Measurement of elastic proton-proton scattering at $\sqrt{s} = 13\,\mathrm{TeV}$ with the ALFA sub-detector of ATLAS at the LHC

Christian Heinz

Dissertation

2. Physikalisches Institut

Fachbereich 07 Mathematik und Informatik, Physik,

Geographie

Justus-Liebig-Universität Gießen

Contents

Abstract

The ALFA (Absolute Luminosity for ATLAS) Roman Pot detector system is part of the forward instrumentation of ATLAS located about 240 m away from the interaction point in the LHC tunnel in both directions. ALFA consists of a scintillating fiber tracker housed in vertical Roman Pots which enables the measurement of elastic proton-proton scattering at small scattering angles. In 2016 seven data-sets were recorded at a center-of-mass energy of $\sqrt{s} = 13$ TeV during a fill with special beam optics of the LHC with $\beta^* = 2.5$ km and parallel-to-point focusing in the vertical plane.

The four-momentum transfer t is measured for elastically scattered protons and used to extract the differential elastic cross section. In this work, the reconstruction efficiency for each of these seven data-sets is determined, which is needed for the correct normalization of the differential elastic cross section, in order to derive the the total cross section and the slope of the elastic cross section at small $|t|$, using the optical theorem. The ρ-parameter, which is the ratio of the real to imaginary part of the forward scattering amplitude, is also measured at this given center of mass energy. The systematic uncertainties for the determination of these quantities as a result of the uncertainties from the determination of the reconstruction efficiency is investigated.

Deutschsprachige Zusammenfassung

Am Large Hadron Collider (LHC) am CERN bei Genf werden Protonen mit bisher unerreichter Schwerpunktsenergie kollidiert. Sowohl die Suche nach bisher unentdeckten Teilchen, als auch die Präzisionsmessungen an den Zerfallskanälen bereits bekannter Teilchen hat das Potential, neue physikalische Erkenntnisse zu erbringen, welche sich jenseits unseres bekannten physikalischen Weltbildes befinden, das durch das Standardmodell beschrieben wird. Eine solche Untersuchung ist die Analyse der Winkelverteilung von elastisch gestreuten Protonen, welche gegenwärtig nicht quantitativ aus bekannten Theorien berechnet werden kann.

In dieser Arbeit wurden Daten des ALFA-Detektors analysiert, welcher für die Untersuchung ebendieser Streuprozesse konstruiert wurde. ALFA ist Teil des ATLAS-Detektors am LHC. ALFA besteht aus acht einzelnen Detektoren, die sich rund 240 Meter vom Kollisionspunkt von ATLAS entfernt in beiden Richtungen direkt an der LHC Strahlröhre befinden. Durch mechanische Vorrichtungen ("Roman Pots") ist es möglich, alle ALFA Detektoren vertikal sehr nah an den LHC-Strahl heranzuführen, um gestreute Protonen unter sehr kleinen Streuwinkeln zu detektieren.

In dieser Arbeit wurde für die sieben separaten Datensätze von 2016 bei spezieller $\beta^* = 2.5\,\text{km}$-Strahloptik und Kollisionsenergie von $\sqrt{s} = 13\,\text{TeV}$ jeweils die Rekonstruktionseffizienz der Protonendetektion bestimmt. Davon ausgehend wird eine Abschätzung der Werte einer Reihe von interessanten Standardmodellparametern bei dieser Kollisionsenergie, sowie ein Vergleich mit vorherigen Messungen bei niedrigeren Energien gegeben. Der erste Parameter ist der totale Wirkungsquerschnittes σ_{tot} der Proton-Proton Streuung, der sich aus der Messung mittels Optischem Theorem herleiten lässt. Des Weiteren wird der nukleare Steigungs-Parameter B bestimmt, ein Maß für den exponentiellen Abfall der Streurate mit steigendem Winkel. Zuletzt wird der ρ-Parameter bestimmt, das Verhältnis zwischen Real- und Imaginärteil der elastischen Vorwärtsstreuamplitude. Die systematische Unsicherheit in der Bestimmung dieser Parameter durch die Unsicherheit in der Bestimmung der Rekonstruktionseffizienz is ebenfalls zentraler Bestandteil dieser Arbeit.

Chapter 1

Introduction

At the Large Hadron Collider at CERN near Geneva, protons are brought to collision at the highest man-made collision energies ever achieved. The search for yet undiscovered particles and precision measurements that deviate from predictions has the potential to reveal new physics which goes beyond out current understanding of the world given by the Standard Model. Further studies include the measurements of Standard Model processes, which can not be quantitatively calculated with current mathematical techniques, so as the elastic scattering between two protons at small momentum transfer, which will be subject of this thesis.

For this analysis, data from the ALFA detector assembly was analyzed. ALFA is part of the ATLAS detector at the LHC, one of the four largest experiments and two of the so called "multi purpose" detectors at the LHC. With the ALFA detectors of ATLAS, the position displacement of elastically scattered protons relative to the LHC beam at a distance of about 240 meters is measured. From the position measurements, one can calculate the momentum transfer that the proton pair underwent. From the measurement, how many protons were scattered at which momentum transfer (angle), several interesting Standard Model quantities can be calculated. The main one is the derivation of the total pp-cross-section by means of the "optical theorem", which will be used as an input parameter in simulation of other processes. The second quantity is the "nuclear slope" parameter B and lastly the ρ-parameter, which is the ratio between the real

and imaginary part of the elastic scattering amplitude at vanishing momentum transfer. That one is particularly interesting, because it provides the basis for the prediction of the energy evolution of the total cross-section at larger energies. This will be an important quantity for the simulation of atmospheric cosmic ray showers and will aid in design of potential future collider experiments at larger collision energies, since it will give basis for an estimate of the expected collision rates that need to be handled.

In this thesis the ATLAS study of elastic scattering in the Coulomb-Nuclear-Interference region at $\sqrt{s} = 13\,\text{TeV}$ is presented. It will be the second study of ATLAS at this region which provides sensitivity to the ρ-parameter.

After this introduction, the first part of the thesis in chapter 2 will give the basics of the theoretical framework of proton scattering kinematics and the derivation of the mentioned physical quantities from those.

In chapter 3 an overview of the experimental facility of CERN, LHC, ATLAS and ALFA is given, followed by details of the data taking which is used in this thesis. At last the reconstruction of the position of proton tracks from detector fiber activity is discussed.

In chapter 4 the beam optics is discussed, in general for a particle collider and then followed by a section on the special properties of the beam optics used. At last, the calculation of the momentum transfer from measured proton positions is explained. Chapter 5 as the main part of this thesis is devoted to the analysis of the recorded data which entails the selection for elastic events in the data set. This is followed by a section dedicated on how to estimate the residual amount of background contamination. After this, the determination of the event reconstruction efficiency together with their statistical and systematic uncertainties is shown. This will be complemented by the determination of the acceptance and unfolding correction for the obtained momentum transfer spectrum (t- spectrum).

In chapter 6, results from the data analysis are applied and physical quantities are derived together with their expected uncertainties due to reconstruction efficiency uncertanties. This is supplemented by a comparison with precious measurements at other energies. Chapter 7 gives a short summary.

Chapter 2

Theory

2.1 Kinematics and conventions

The measurements of the total cross-section, the nuclear B-slope and ρ-parameter described in this thesis rely on the description of elastic proton-proton scattering [1], which is illustrated in figure 2.1.

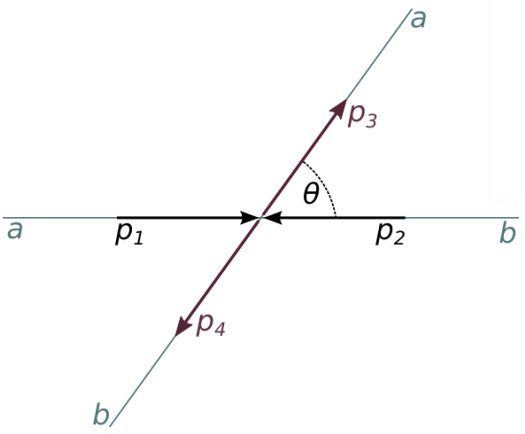

FIGURE 2.1: Schematic drawing of an elastic scattering event in the center-of-mass frame. a and b represent the two protons involved in the scattering, where p_1 and p_2 are the four-momenta of the protons in the initial state and p_3 and p_4 are the four-momenta of those in the final state.

The figure shows two protons, a and b, which remain intact after collision, only being deflected by an angle θ. The general form of the collision is given by $p+p \rightarrow p+p$.

The invariant Mandelstam variable s for this type of collision is given by:

$$s = (p_1 + p_2)^2 = m_1^2 + m_2^2 + 2\left(\sqrt{p^2 + m_1^2}\sqrt{p^2 + m_2^2} + p^2\right) \tag{2.1}$$

where p_i are the magnitudes of the center-of-mass three-momenta of the protons. For two protons this equation simplifies to:

$$s = 4(p^2 + m^2) \tag{2.2}$$

The invariant Mandelstam variable t, which describes the four-momentum transfer in the collision is given by:

$$t = (p_1 - p_3)^2 = -4p^2\sin^2\left(\frac{\theta}{2}\right) \approx -(p\theta)^2 \tag{2.3}$$

where the approximation in equation 2.3 is valid under the small angle conditions studied in this thesis.

The third Mandelstam variable u is given by:

$$u = (p_1 - p_4)^2 \tag{2.4}$$

The sum of the three Mandelstam variables is given by:

$$s + t + u = 4m^2 \tag{2.5}$$

The optical theorem relates the elastic scattering amplitude f in forward direction with the total proton-proton cross-section:

$$\sigma_{\text{tot}} = \frac{4\pi}{p}\Im f(t \to 0) \tag{2.6}$$

2.2 Elastic hadronic scattering in the presence of the Coulomb field

In this chapter the effects of the hadronic and coulombic field in elastic scattering of protons are discussed. These two scattering contributions are then combined.

Elastic proton-proton scattering in the Nuclear field

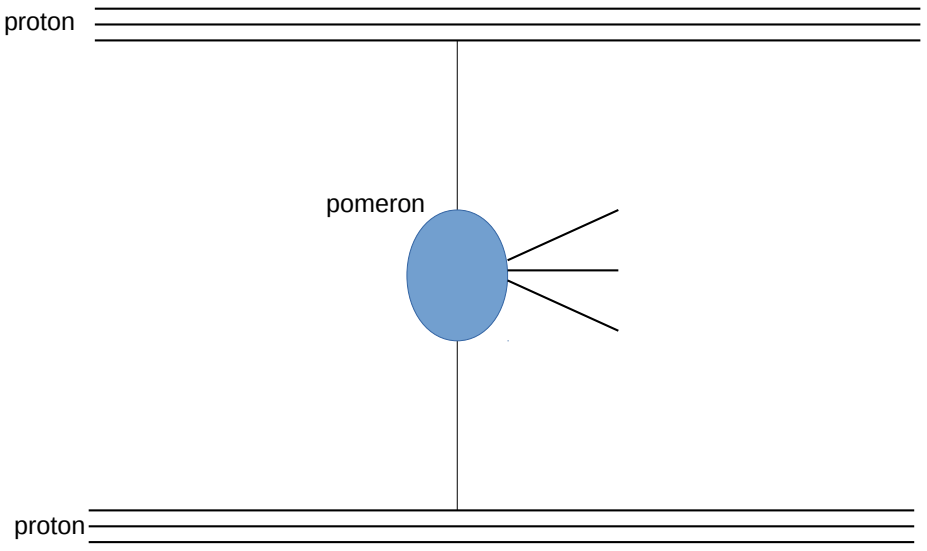

FIGURE 2.2: Schematic drawing of a pomeron exchange between two protons. This type of inelastic scattering contributes to a significant proportion to the irreducible background in this run. The nature of the pomeron is yet to be discovered.

In this analysis the hadronic elastic scattering cross-section is described by a simple exponential form, which was shown to be adequate in the small $|t|$ region:

$$\left[\frac{d\sigma_{\mathrm{N}}}{dt}\right] = \left[\frac{d\sigma_{\mathrm{N}}}{dt}\right]_{t\to 0} e^{-B|t|} \tag{2.7}$$

Using the optical theorem 2.6 and the relation $|f|^2 = \frac{d\sigma_{\mathrm{N}}}{d\Omega_{\mathrm{c.m.}}}$ one gets:

$$\begin{aligned}\left[\frac{d\sigma_{\mathrm{N}}}{dt}\right]_{t\to 0} &= \frac{\pi}{p^2}\left[\frac{d\sigma_{\mathrm{N}}}{d\Omega_{\mathrm{c.m.}}}\right]_{\theta\to 0} = \frac{\pi}{p^2}\left|\Re f(0) + i\Im f(0)\right|^2 \\ &= \pi\left|\frac{(\rho+i)\Im f(0)}{p}\right|^2 = \pi\left|\frac{(\rho+i)\sigma_{\mathrm{tot}}}{2\pi}\right|^2\end{aligned} \tag{2.8}$$

In equation 2.8 the parameter $\rho = \frac{\Re f(0)}{\Im f(0)}$ is introduced.
The nuclear scattering amplitude is then given by:

$$F_N(t) = (\rho+i)\frac{\sigma_{\mathrm{tot}}}{4\sqrt{\pi}} e^{-B|t|/2} \tag{2.9}$$

Elastic proton-proton scattering in the Coulomb field

The appropriate Feynman diagram for elastic proton-proton scattering in the Coulomb field is given in figure 2.3.

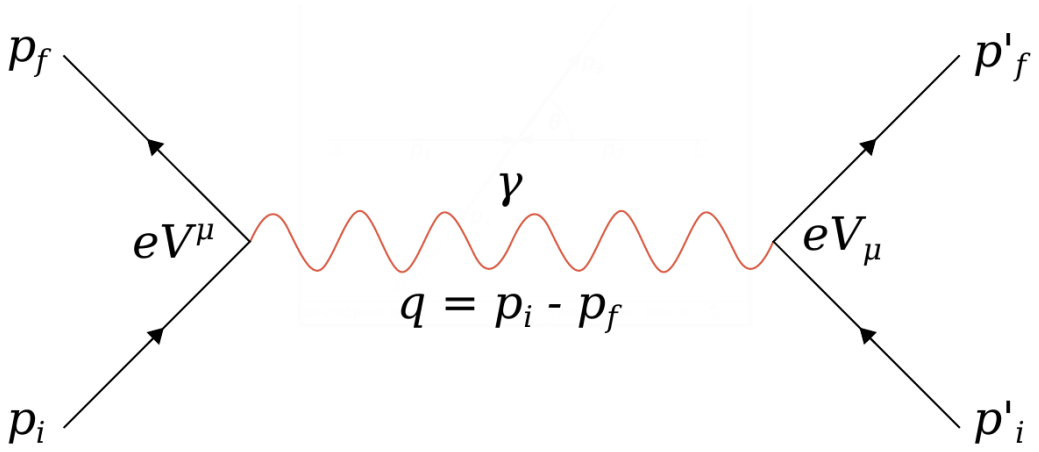

FIGURE 2.3: One-photon exchange for elastic proton-proton scattering in the Coulomb field.

Here, the protons are scattered according to the reaction $p_i + p_i' \rightarrow p_f + p_f'$. The coupling constants are given by eV^μ and eV_μ, where $V^\mu = G(p_i + p_f)^\mu$. $G(t)$ is the electric form factor of the proton.

The electromagnetic differential cross-section is then evaluated to:

$$\frac{d\sigma_C}{dt} = \pi \left| \frac{-2\alpha G^2(t)}{\beta_{\text{lab}}|t|} \left(1 - \frac{|t|}{4mE_{\text{lab}}}\right) \right|^2 \tag{2.10}$$

with the electromagnetic coupling constant $\alpha \approx 1/137$ and the relativistic β and Energy E_{lab} of the incoming proton in the laboratory frame.

Since $|t|$ is negligible, equation 2.10 simplifies to:

$$\frac{d\sigma_C}{dt} = \pi \left| \frac{-2\alpha G^2(t)}{\beta_{\text{lab}}|t|} \right|^2 \tag{2.11}$$

The electromagnetic form factor $G(t)$ is parametrized by a dipole form [2]:

$$G(t) = \left(\frac{\Delta^2}{\Delta^2 + |t|} \right)^2 \tag{2.12}$$

with $\Delta = 0.71\,\text{GeV}^2$

The Coulomb amplitude used in this analysis is given by:

$$F_C(t) = -\frac{2\sqrt{\pi}\alpha G^2(t)}{|t|} \tag{2.13}$$

where $|F_C(t)|^2 = \frac{d\sigma}{dt}$

Combination of the two scattering contributions

To superimpose the Coulomb and the nuclear amplitude to get the combined differential cross-section, one has to introduce a phase factor $e^{i\alpha\Phi(t)}$:

$$\frac{d\sigma}{dt} = |F_C(t)e^{i\alpha\Phi(t)} + F_N(t)|^2 = \pi \left| -\frac{2\pi\alpha G^2(t)}{|t|} e^{i\alpha\Phi(t)} + (\rho + i)\frac{\sigma_{\text{tot}}}{4\pi} e^{-B|t|/2} \right|^2 \tag{2.14}$$

In equation 2.14 it is assumed that the ρ-parameter is constant over the small $|t|$-range probed in this analysis. The phase factor $\Phi(t)$ is given by:

$$\Phi(t) = -\left(\gamma_E + \ln\left(\frac{B|t|}{2}\right)\right) \tag{2.15}$$

where γ_E is Euler's constant. With the use of these parametrization, the form of the differential elastic cross section is given by:

$$\frac{d\sigma}{dt} = \frac{d\sigma_{\text{C}}}{dt} + \frac{d\sigma_{\text{CNI}}}{dt} + \frac{d\sigma_{\text{N}}}{dt} \tag{2.16}$$

which evaluates to

$$\frac{d\sigma}{dt} = \frac{4\pi\alpha^2}{t^2} G^4(t) - \sigma_{\text{tot}} \frac{\alpha G^2(t)}{|t|} [\rho + \alpha\Phi(t)] e^{-B|t|/2} + \sigma_{\text{tot}} \frac{1+\rho^2}{16\pi} e^{-B|t|} \tag{2.17}$$

Equation 2.17 contains three contributions to the differential elastic cross section. The coulomb term, the CNI-term and the nuclear therm. The region where the interference term becomes important is given by $|F_C(t)| = |F_N(t)|$. This evaluates approximately to:

$$|t_{\mathrm{CNI}}| \approx \frac{8\pi\alpha}{\sigma_{\mathrm{tot}}} \tag{2.18}$$

where σ_{tot} is given in mb and t_{CNI} is given in GeV^2

The expression in 2.17 is used to extract the parameters of interest, σ_{tot}, B and ρ from the measured differential elastic cross-section.

The plotted form of equation 2.17 is shown in figure 2.4. A measurement of this elastic cross-section down to the Coulomb-nuclear-interference region ($|t_{\mathrm{CNI}}| \approx 0.0018\,\mathrm{GeV}^2$) is necessary to extract the parameters ρ and the total applied Luminosity $\mathscr{L}$ alongside σ_{tot} and B, since at this region these two parameters become uncorrelated from the latter ones in the measured differential cross-section. At smaller values of $|t|$, the coulomb interaction becomes dominant, whereas for larger values of $|t|$ the exponential nuclear interaction dominates.

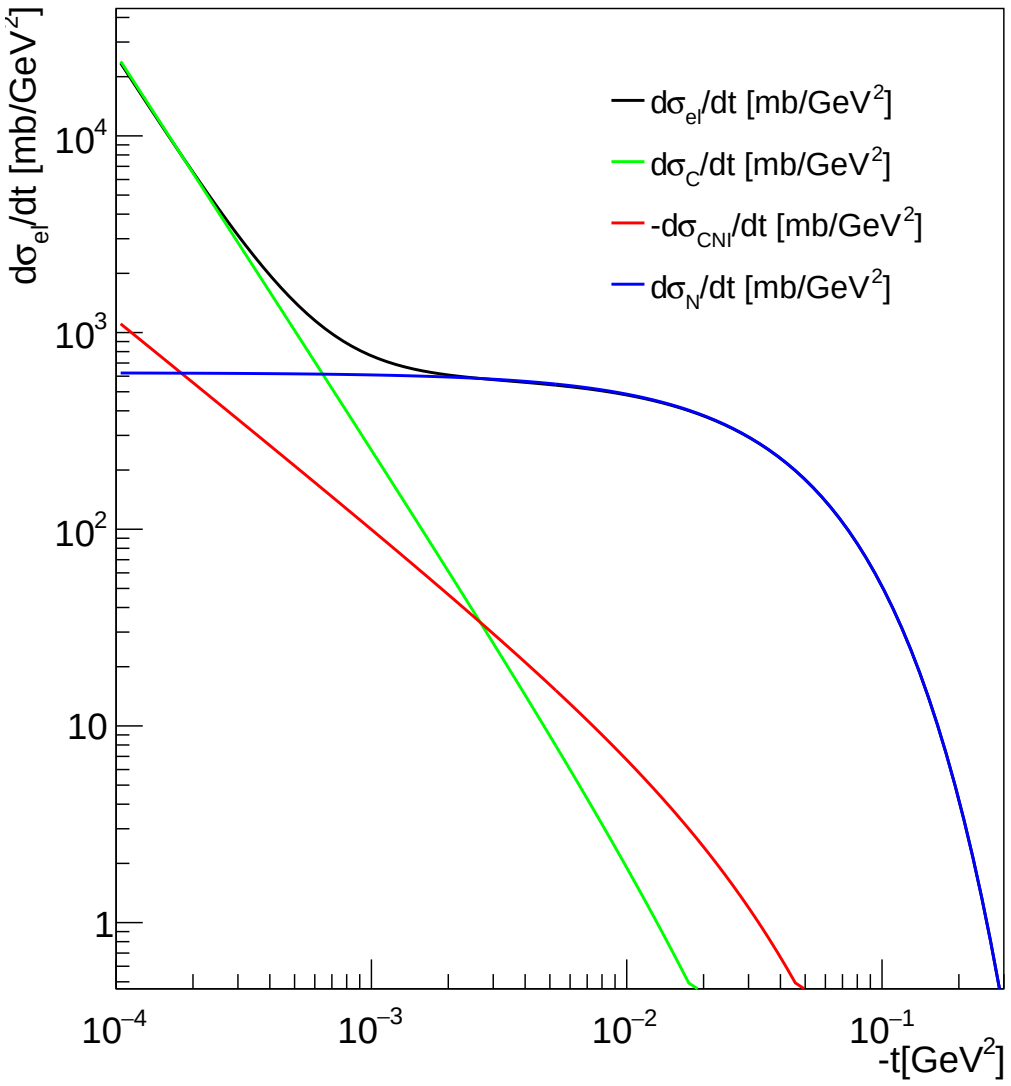

FIGURE 2.4: Simulation of the differential elastic cross-section according to equation 2.17 near the Coulomb-Nuclear-Interference (CNI) region at $\sqrt{s} = 13\,\text{TeV}$ given by the black curve. At the high $|t|$-end, the nuclear scattering contributions dominate (blue). At smaller $|t|$ the CNI-region significantly contributes (green) and towards lowest $|t|$ the Coulomb-term gives a sharp exponential rise (linear in this logarithmic scale). The CNI-term (red) is negative and plotted with inverse sign for plotting convenience.

The ρ-paramter

From previous ATLAS/ALFA data takings at $\beta^* = 90\,\text{m}$-beam-optics, the ρ-parameter was input in equation 2.17 as an external parameter due to the lack of accessibility of the CNI-region in those measurements. The data analyzed in this

work at $\beta^* = 2500\,\text{m}$-beam-optics provides a measurement of the differential elastic cross-section in this region and hence the feasibility of the direct determination of the ρ-parameter is explored.

The electromagnetic form factor

As stated before, the electric form factor $G(t)$ of the proton is parametrized by a dipole function as in equation 2.12. Measurements of low energy elastic *ep*-scattering show a deviation in the order of a few percent from the simple dipole form. High precision data was taken by the A1 experiment [3]. Based on that, the electric and magnetic form factors $G_E(t)$ and $G_M(t)$ were reevaluated. The resulting parameterizations in the $|t|$-range of interest are shown in figure 2.5. The deviations grow with increasing $|t|$ to the order of 4%.

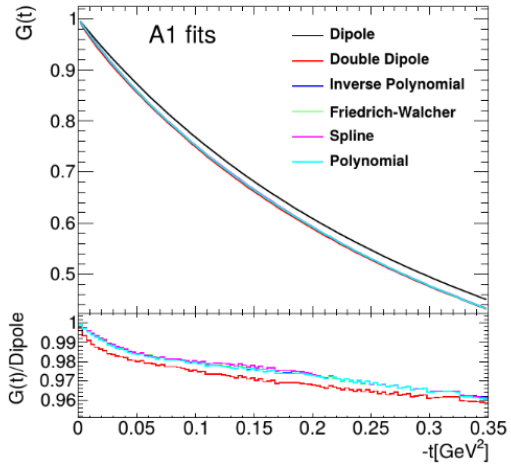

FIGURE 2.5: Parameterizations of the electromagnetic form factor $G(t)$ of the proton obtained by the A1 collaboration [3]. The bottom inlay shows the deviation of those models from the nominal dipole form.

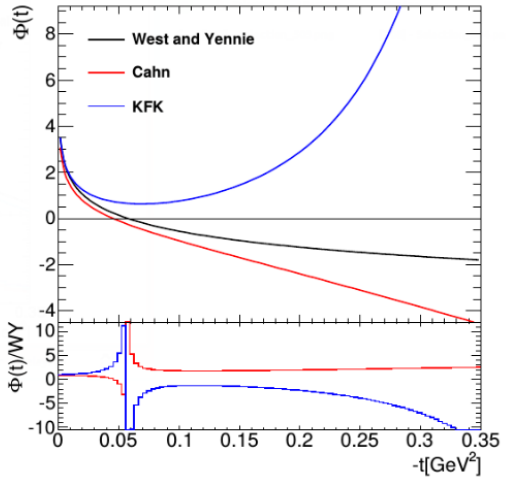

FIGURE 2.6: Parameterizations of the Coulomb phase $\Phi(t)$ by [4], [2] and [5]. The bottom inlay shows the deviation from West and Yennie

The Coulomb phase

For the Coulomb phase, also several parameterizations are available. The nominal one used in equation 2.17 is the parameterization from West and Yennie [4], shown in equation 2.15.

To assess the systematic uncertainty of the Coulomb phase, different models are discussed, like for the electromagnetic form factor.
An approach of Cahn [2] extends the calculation by West and Yennie to higher orders:

$$\Phi(t) = -\left(\gamma_E + \ln\left(\frac{B|t|}{2}\right) + \ln\left(1 + \frac{8}{B\Lambda^2}\right) + \frac{4|t|}{\Lambda^2} + \ln\left(\frac{4|t|}{\Lambda^2}\right) + \frac{2|t|}{\Lambda^2}\right) \quad (2.19)$$

Another model was considered by Kohara, Ferreira and Kodama [5], which assumes different nuclear slopes for the real and imaginary scattering amplitudes respectively. Fits on measurements from TOTEM yield an approximate expression of the real part of the coulomb phase:

$$\Phi_R(s,t) \approx -\left(\ln\left(\frac{-t}{s}\right) + \frac{1}{c^2+1}\left[c^2 I(B_R) + I(B_I)\right]\right) \quad (2.20)$$

with

$$\begin{aligned} I(B) &= \int_{-4p^2}^{0} \frac{\mathrm{d}t'}{|t'-t|}\left[1 - e^{B(t'-t)/2}\right] \quad (2.21)\\ &= E_1\left[\frac{B}{2}\left(4p^2+t\right)\right] - E_i\left[-\frac{Bt}{2}\right] + \ln\left[\frac{B}{2}\left(4p^2+t\right)\right] + \ln\left[-\frac{Bt}{2}\right] + 2\gamma_E \end{aligned}$$

and

$$c = \rho e^{(B_R - B_I)t/2} \quad (2.22)$$

with the nuclear slope of the imaginary part B_I, slope of the real part B_R and exponential integral functions $E_{1,i}$.

Figure 2.6 shows different coulomb phase calculations as a function of t. All models agree well in the lower end of the t-range, but they deviate at larger t-values.

The Nuclear amplitude

The nuclear scattering amplitude is parametrized by equation 2.9. It contains a simple exponential form with a constant nuclear slope parameter B. This approximation is valid in the small $|t|$ range between the CNI-region and before the position of the diffractive dip, shown in figure 2.7 which shows a measurement of TOTEM on a larger $|t|$-range.

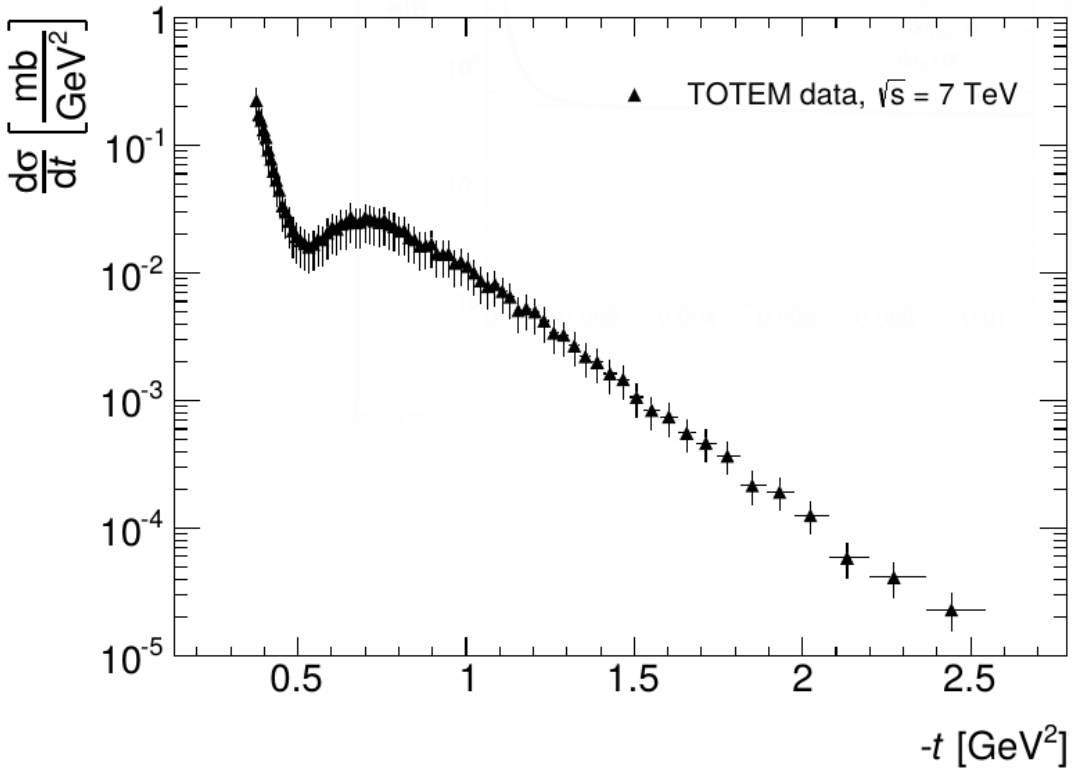

FIGURE 2.7: Differential elastic cross-section $d\sigma/dt$ in a wider t-range by the TOTEM Collaboration at $\sqrt{s} = 7\,\text{TeV}$ [6]. At this energy the diffractive dip is visible around $|t| \approx 0.5\,\text{GeV}^2$. The nuclear amplitude is dominant everywhere in the measured range.

A more recent measurement by TOTEM shown in figure 2.8 shows the behavior of the differential cross section at very small $|t|$-values, where the rise of the differential cross section due to the presence of the CNI-term becomes apparent.

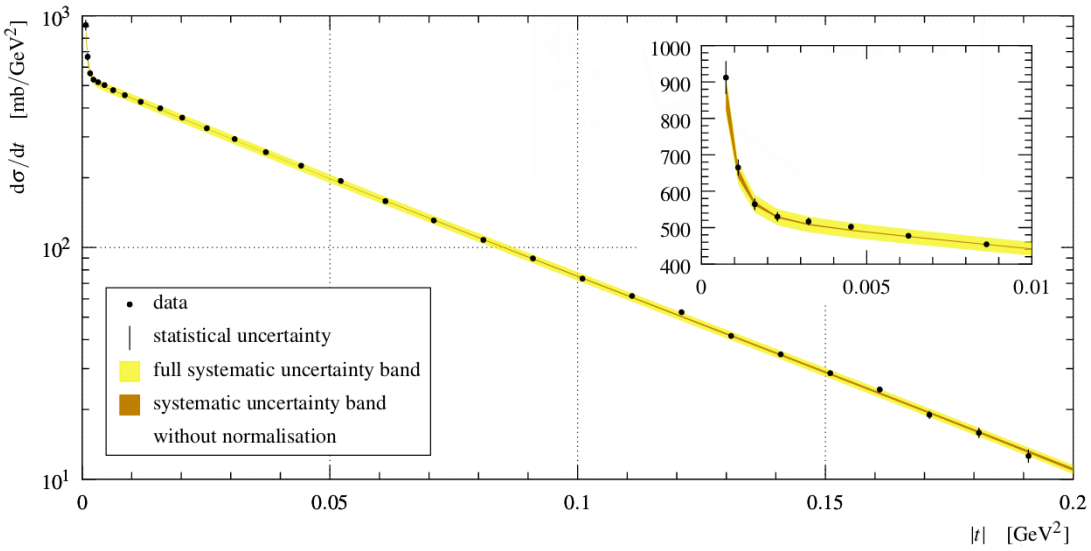

FIGURE 2.8: Differential elastic cross-section $d\sigma/dt$ in the lower t-range by the TOTEM Collaboration at $\sqrt{s} = 8\,\text{TeV}$ [7]. The inlay is a zoom-in on the very low end of the t-range, which shows the rise in differential elastic cross section due to the coulomb nuclear interference term.

Deviations from the simple exponential form within the $|t|$-region of interest have to be considered. One possible modification is the addition of a $|t|$-dependent slope by introducing an additional parameter C:

$$f_{\text{N}}(t) = (\rho + i)\,\frac{\sigma_{\text{tot}}}{\hbar c} e^{-Bt/2 - Ct^2/2} \tag{2.23}$$

This model was previously used in experiments and discussed in theory by West and Yennie and Block and Cahn.

Another extension was proposed by Selyugin [8], which adds a hadron-no-spin-flip amplitude with pion mass μ and an additional fit parameter c:

$$f_{\text{N}}(t) = (\rho + i)\,\frac{\sigma_{\text{tot}}}{\hbar c} e^{-Bt/2 - c/2(\sqrt{4\mu^2 - t} - 2\mu)} \tag{2.24}$$

Another extension was proposed by KFK [9], which assumes different nuclear slopes B_R and B_I for the real and imaginary part of the amplitude:

$$f_{\mathrm{N}}(t) = \rho \frac{\sigma_{\mathrm{tot}}}{\hbar c} e^{-B_R t/2} + i \frac{\sigma_{\mathrm{tot}}}{\hbar c} e^{-B_I t/2} \tag{2.25}$$

Also there are model independent parameterizations available, absorbing physical effects in a variety of free fit parameters. One considered is a from proposed by Phillips and Barger [10]:

$$f_{\mathrm{el}}(t) = i \left[G^2(t) \sqrt{A} e^{-Bt/2} + e^{i\phi} \sqrt{C} e^{-Dt/2} \right] \tag{2.26}$$

At last there is a parametrization by Bourrely, Soffer and Wu [11], consisting of symmetric expressions for the real and imaginary part of the amplitude:

$$\Re f_{\mathrm{el}}(t) = c_1 (t_1 + t) e^{-b_1 t/2} \ , \ \Im f_{\mathrm{el}}(t) = c_2 (t_2 + t) e^{-b_1 t/2} \tag{2.27}$$

2.3 Measurement of $\sigma_{\mathbf{tot}}$ and B from elastic scattering

The differential elastic cross section is inferred from a counting rate measurement. For this, the t-range of interest is binned and the number of elastic collisions in a given t-bin is determined. The counting rate for each t-bin has to be corrected for the predicted background content and the geometrical acceptance available for this bin. Finally the entire spectrum has to be scaled for data acquisition dead times and trigger- and reconstruction inefficiencies. The counting rate $\Delta N(t)$ can then easily be related to the differential elastic cross-section by the integrated luminosity $\mathscr{L}$:

$$\Delta N(t) = \mathscr{L} \left(\frac{d\sigma_{\mathrm{el}}}{dt} \right) \tag{2.28}$$

In case the experiment is able to reach the Coulomb region $|t| \ll |t_{\mathrm{CNI}}|$, one can exploit the fact, that the couloumb part of the differential cross section is

$\frac{d\sigma_C}{dt} \approx 4\pi(\alpha/t)^2$ and hence the luminosity $\mathscr{L}$ could be extracted directly from the measurement without the need for a dedicated analysis based on other detectors of ATLAS and a calibration from a van-der-Meer scan, which provides an absolute luminosity measurement by performing a measurement of particle production rates as a function of a stepwise collision displacement of the two beams. The data sets available for this thesis probes into the CNI-region.

In previous ATLAS-ALFA experiments the luminosity was input from a dedicated measurement. Obtaining the total cross-section in this way is called the "luminosity dependent method". Equations 2.7, 2.8 and 2.28 yield:

$$\sigma_{\text{tot}}^2 = \frac{16\pi}{1+\rho^2}\left(\frac{\sigma_{\text{el}}}{dt}\right)_{t\to 0} = \frac{16\pi}{1+\rho^2}\frac{\Delta N(0)}{\mathscr{L}} \tag{2.29}$$

where $\Delta N(0)$ is the counting rate extrapolated to $|t| = 0$, the so called "Optical Point".

A second important method is the so called "luminosity independent method" which relies on a simultaneous measurement of the inelastic counting rate to obtain the full counting rate $N_{\text{tot}} = N_{\text{elastic}} + N_{\text{inelastic}}$ and cancel out the Luminosity requirement in equation 2.29:

$$\sigma_{\text{tot}}^2 = \frac{16\pi}{1+\rho^2}\frac{\Delta N(0)}{N_{\text{tot}}} \tag{2.30}$$

In earlier ALFA measurements, the ρ-parameter was input using model predictions, since the CNI-region was not accessible. Since the ρ-parameter is small, it only contributed weakly to the systematic uncertainty of σ_{tot} in these two methods.

The total cross section is composed of the sum of elastic and inelastic cross section:

$$\sigma_{\text{tot}} = \sigma_{\text{elastic}} + \sigma_{\text{inelastic}} \tag{2.31}$$

These two additional quantities can be derived from the measurement. The elastic cross section σ_{elastic} can simply be obtained through integration of the differential elastic cross section:

$$\sigma_{\text{elastic}} = \int_{-\infty}^{0} \frac{\sigma_{\text{elastic}}}{dt}\,\mathrm{d}t = \sigma_{\text{tot}}^2 \frac{1+\rho^2}{16\pi B} \tag{2.32}$$

Equation 2.32 can be written as

$$\frac{\sigma_{\text{elastic}}}{\sigma_{\text{tot}}} = \sigma_{\text{tot}} \frac{1+\rho^2}{16\pi B} \tag{2.33}$$

At small ρ in high proton energies, equation 2.33 implies that the ratio $\frac{\sigma_{\text{elastic}}}{\sigma_{\text{tot}}}$ varies the same as the ratio $\frac{\sigma_{\text{tot}}}{B}$. For infinite collision energies, in many scattering models this ratio approaches to the "Black Disk Limit" $\frac{\sigma_{\text{elastic}}}{\sigma_{\text{tot}}} = 1/2$

Finally the nuclear slope parameter B can be obtained independent of luminosity normalization from the exponential slope in the hadronic region of the differential cross-section.

Chapter 3

Experimental setup

3.1 CERN and the Large Hadron Collider

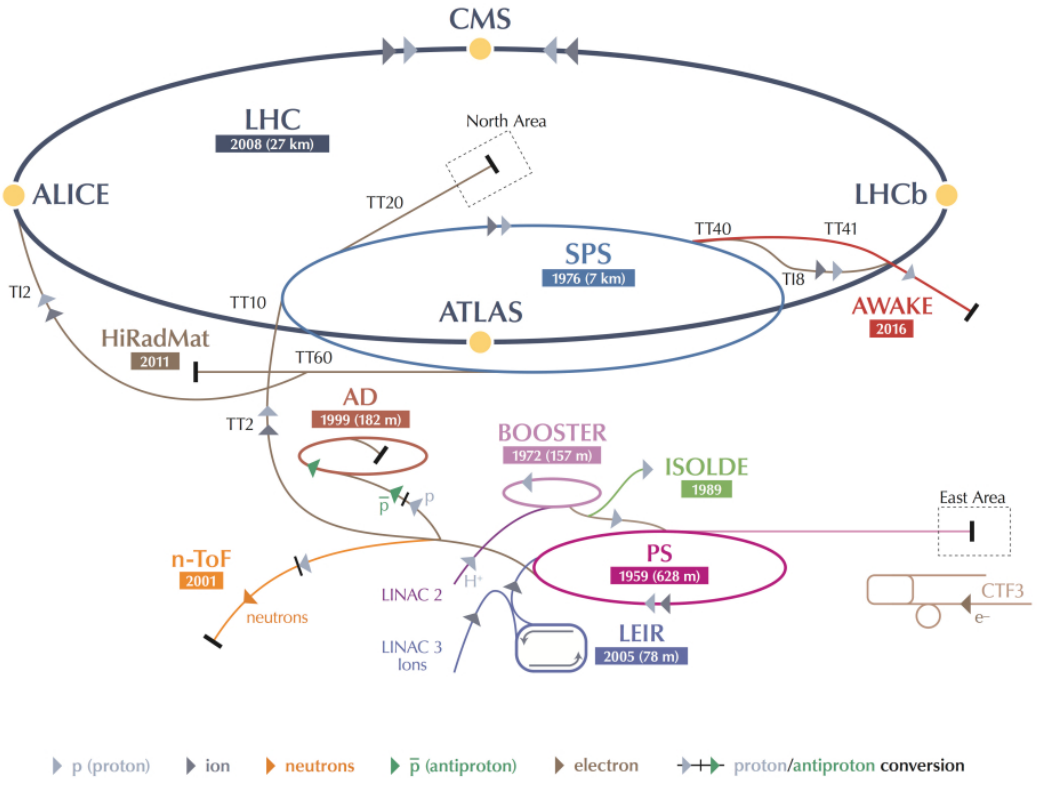

FIGURE 3.1: The LHC is the main ring (dark gray line) in a complex chain of particle accelerators. The smaller machines are used in a chain to help boosting the particles to their final energies and provide beams to a whole set of smaller experiments. [12]

The European Organization for Nuclear Research, or short CERN (French: Organisation européenne pour la recherche nucléaire) is the worlds largest particle accelerator complex. Founded in 1954, it currently encompasses 22 member states. The organization has official United Nations observer status. CERN is located on the border between Switzerland and France near Geneva. Today CERN focuses on particle physics, the study of the fundamental constituents of matter and the interactions between them.

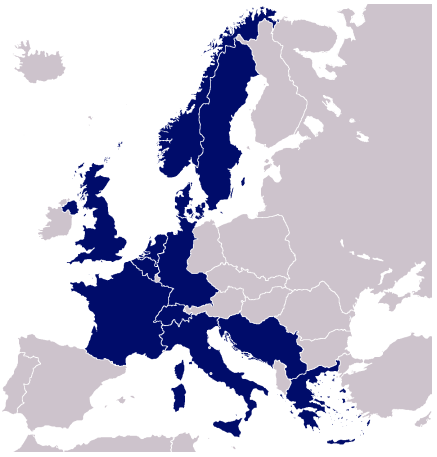

FIGURE 3.2: The twelve founding member states of CERN in 1954 with the nation boarders at this time [13]

Several ground breaking discoveries and achievements were accomplished at CERN, e.g.

- 1973: Discovery of neutral currents in the Gargamelle bubble chamber
- 1983: Discovery of the W and Z bosons, the force carriers of the weak interaction, in the UA1 and UA2 experiments
- 1989: Invention of the World Wide Web by Tim Berners-Lee and Robert Cailliau
- 1995: First creation of neutral anti-hydrogen atoms in the PS210 experiment
- 1999 Direct Observation of CP (Charge/Parity) violation in the NA48 experiment.
- 2012 Discovery of a boson with mass of around $m = 125\,\frac{\mathrm{GeV}}{c^2}$, consistent with the theorized Higgs Boson

Figure 3.1 shows the LHC ring on top of the chain of the current accelerator complex. Several older storage rings (PS,SPS) serve as injectors for protons (or

lead ions for the heavy ion program) for the LHC. The LHC was built between 1998 and 2008 in the already preexisting tunnel, which housed the Large Electron Position Collider before. The tunnel is located about 100 meters under ground and is about 27 kilometers in circumference. It is divided into eight linear sections and eight arcs. Figure 3.3 shows a sketch of the underground LHC complex together with the main four experiments and their access shafts. The ATLAS experiment, introduced in detail in section 3.2 is located at "Point 1" (bottom of the image), inside the underground cavern labeled "UX15". Together with the "Point 5" CMS detector both are general purpose experiments, designed to be operated in high luminosity conditions.

The ALICE (A Large Ion Collider Experiment) located at "Point 2" is designed to study heavy ion collisions.

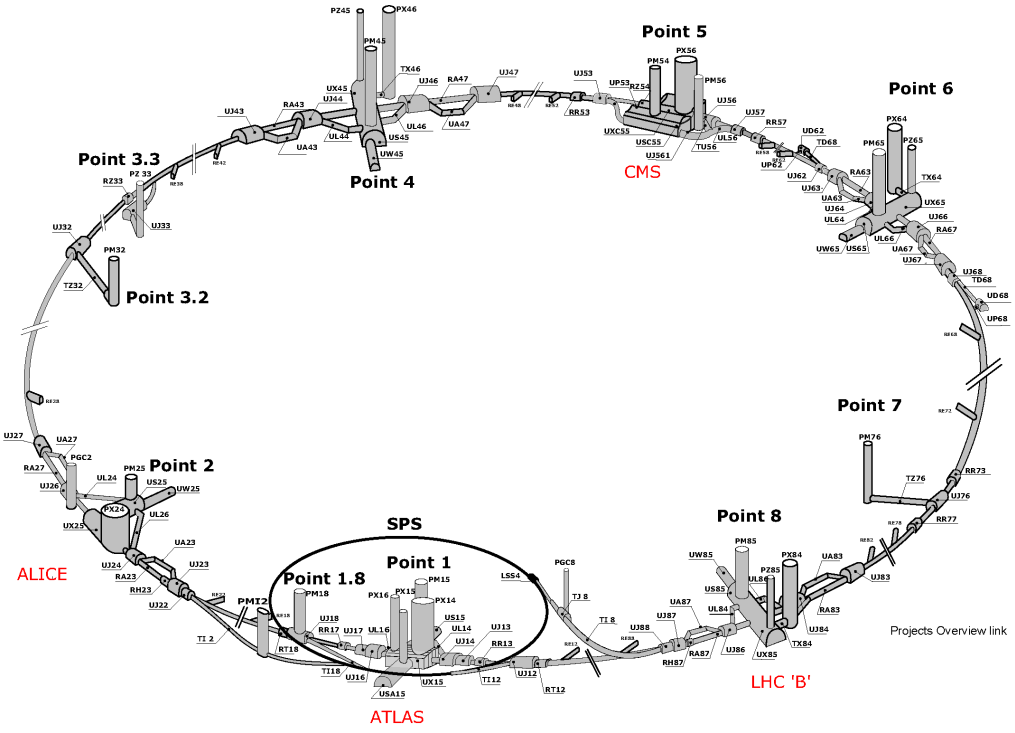

FIGURE 3.3: Sketch of the segments of the LHC ring, including experiment caverns and access ports [14]

The LHCb experiment ("Point 8") is used to study B meson decays and explore the CP violation. This one is a single side forward spectrometer and contrary to

the other main experiments doesn't cover a large solid angle around the respective interaction point. A further experiment, LHCf, is located in the forward region from the interaction point of ATLAS with the goal to measure the rate and energy of produced neutral pions in the LHC for the purpose of study of ultra-high-energy cosmic rays.

In the very forward region of CMS, the "TOTEM" experiment (Total Elastic and diffractive cross-section) is located. Compared to the four main experiments, it is a smaller experiment, consisting of silicon based Roman Pot detectors, which are designed to be inserted into the LHC beam pipe very close to the beam to measure proton scatterings under very small angle. The goal is to measure elastic and diffractive scattering processes. A silicon based forward telescope is used to determine inelastic scattering rates. From this rate, "TOTEM" is able to measure the total proton-proton cross section without having to include external luminosity information from the CMS interaction point, resulting in their "Luminosity independent method" [15].

Elastic and diffractive measurements are also the goal of the ALFA detector, located at each far side from the ATLAS interaction point, however fully integrated into the ATLAS data acquisition system. ALFA relies on the luminosity measurement from ATLAS.

The LHC was built for a design center of mass collision energy of $\sqrt{s} = 14\,\text{TeV}$. However up until now (2018) "only" an energy of $\sqrt{s} = 13\,\text{TeV}$ has been archived, since the necessary magnet training has not been fully performed yet. The two high luminosity experiments ATLAS and CMS were designed for a peak luminosity of $\mathscr{L} = 1 \cdot 10^{34} cm^{-2} s^{-1}$ for proton collisions. LHCb is designed for lower peak luminosity of $\mathscr{L} = 1 \cdot 10^{32} cm^{-2} s^{-1}$ and ALICE is designed for $\mathscr{L} = 1 \cdot 10^{27} cm^{-2} s^{-1}$ in heavy ion mode. In 2017 ATLAS archived a peak Luminosity of $\mathscr{L} = 2.09 \cdot 10^{34} cm^{-2} s^{-1}$ [16].

The proton beam in the LHC is bunched into 2808 slots, separated by 25 ns in time. Each proton bunch is designed to be made up of $1.1 \cdot 10^{11}$ protons.

The LHC uses superconducting niobium-titanium magnets that are cooled down to a temperature of 2 K and operate at magnetic field strength above 8 T. Due

to limited space in the tunnel, each magnet element (the mechanical housing and cryostat framework) has to serve both counter circulating beams, hence twin bore magnets are used with separate coil sets for each beam channel. Out of 9593 magnets in total, 1232 are dipole magnets for bending the beam along the LHC ring segments. The rest are higher order correction magnets. Eight radio frequency cavities per beam are used to accelerate the injected beam in the LHC.

3.2 The ATLAS experiment

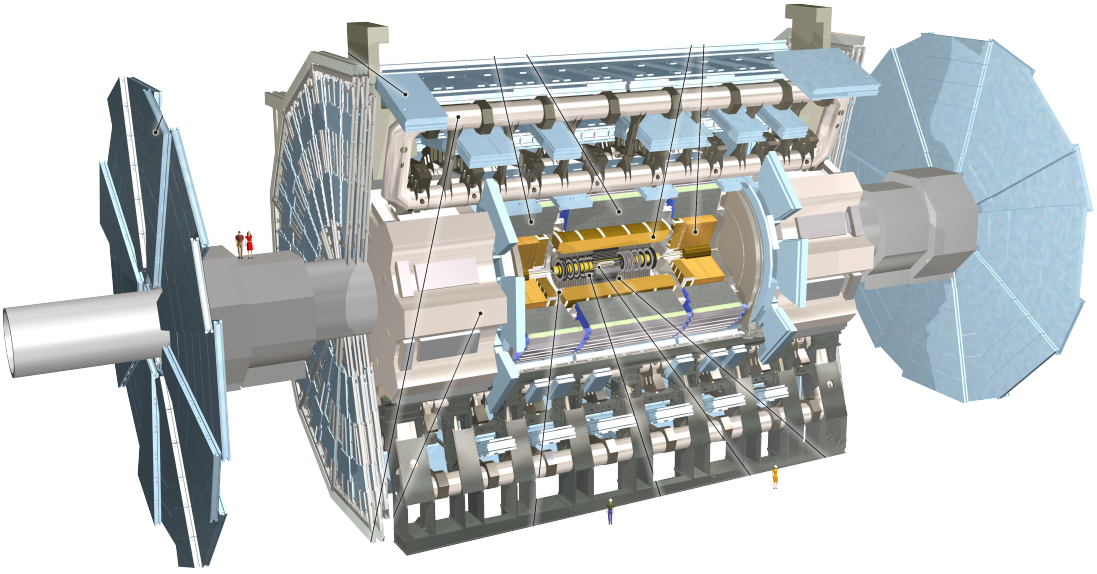

FIGURE 3.4: Schematic overview of the ATLAS experiment with individual detectors, excluding the detectors in the forward region (e.g. ALFA) [17]

In this section, a closer description of the ATLAS detector (A Toroidal LHC ApparatuS) is given. As one of the two general purpose detectors, design considerations for ATLAS had to take into account e.g. high particle interaction rates, harsh radiation environment, many simultaneous tracks (high particle multiplicities).

Figure 3.4 shows schematically the layout of the ATLAS detector around the

interaction point. With dimensions of 46 meters long and 25 meters in diameter, ATLAS is as of this date the largest volume detector ever constructed. With a total weight of around 7000 metric tonnes, it is similar in mass as the Eiffel Tower. The detector consists of many sub-detectors, arranged in an onion shaped layering symmetrically around the interaction point. A torroidal and solenoidal magnet system induce track bending, to infer the momenta of charged particles created. The quantities from this short summary are taken from [18].

Figure 3.5 shows the basic principle of particle tracking and identification. The role of each subsystem shall be explained in the next paragraphs.

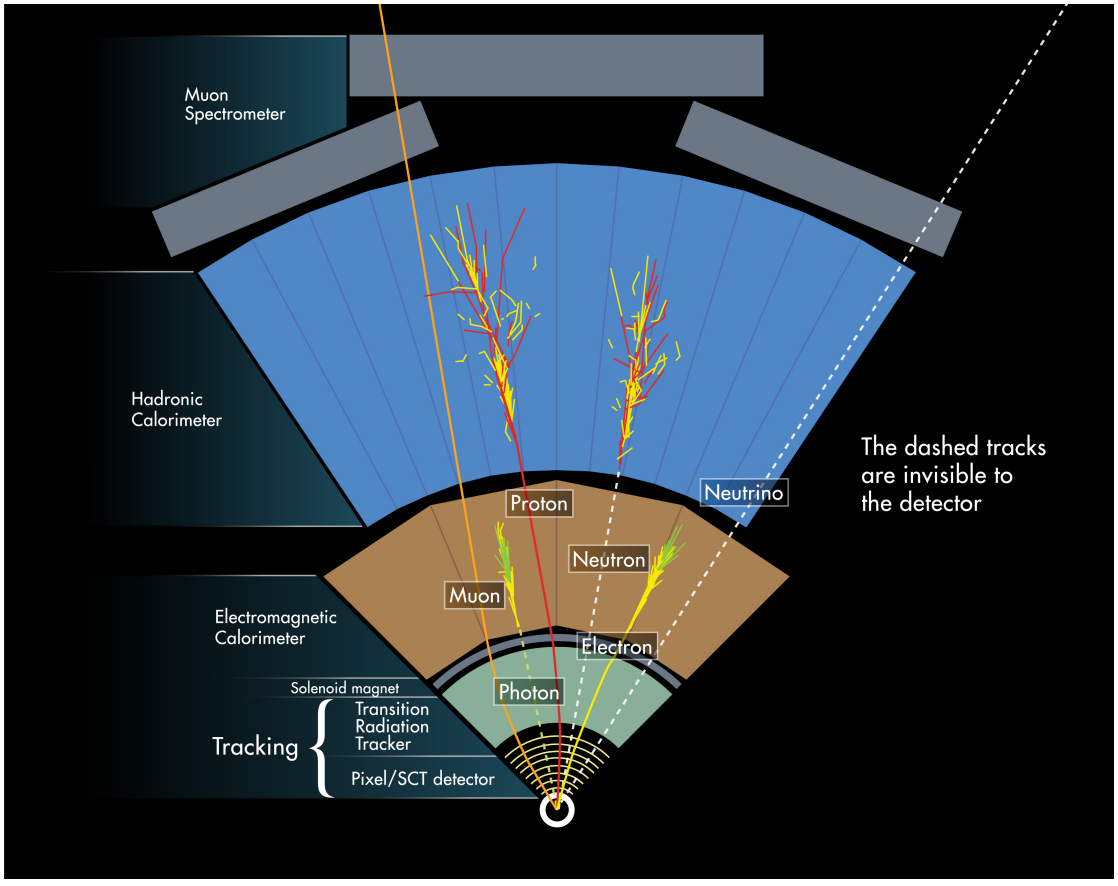

FIGURE 3.5: Schematic radial overview of particle tracking and absorption in the ATLAS detector. [19]

The Inner Detector

The ATLAS inner detector, as sketched in figure 3.6 provides detection and tracking of charged particles created at the interaction point. It has a high efficiency over the pseudorapidity range $|\eta| \leq 2.5$.

The innermost element of the Inner Detector is the "pixel detector". The pixel detector system contains about 80 million detection channels. It is the most important detector for identification and reconstruction of the vertices from the decay of other created particles, e.g. from particles that contained b-quarks, b-tagging of jets (those decay at a measurable distance from the LHC beam, at a location which is called "secondary vertex". The term "primary vertex" indicates the place, where reaction between protons happen from the LHC beam.). It provides a high spacial resolution for the reconstruction of primary vertices in the multiple interaction environment [20].

Further out we have the Semiconductor Tracker (SCT), consisting of eight layers of silicon strip detectors, with 4088 detector modules in total and 768 read out strips per module, providing tracking resolution of around 30 μm
The outer part of the Inner Detector is the Transition Radiation Tracker (TRT). Tracking is achieved in straw-like drift tubes, where electrons produce detectable X-rays when traversing [22].

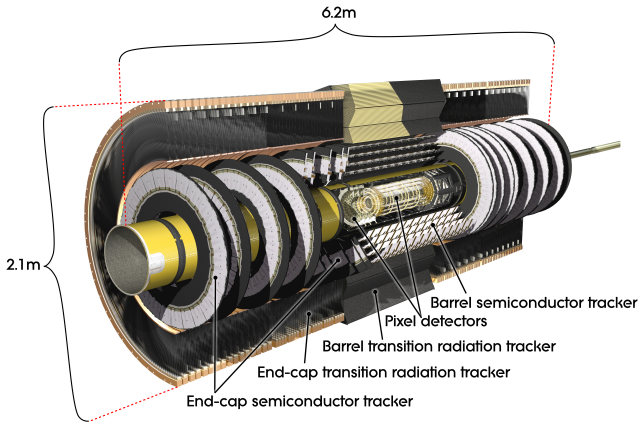

FIGURE 3.6: Schematic sketch of the ATLAS inner detector components [21]

The Magnet System The ATLAS magnet system is composed of four superconducting magnets. One of those is a solenoid magnet, located between the inner detector and the electromagnetic calorimeter. The field strength of the solenoid magnet reaches 2 T and stores 38 mega-joules of energy.
Further we have barrel toroid and two end-cap toroids for the muon chambers, producing 4 T of magnetic field strength.

The Calorimeter System

ATLAS is designed with an electromagnetic and hadronic calorimeter system to absorb particles and photons which interact with the material those respective colorimeters are made of. The particles deposited energy and location is measured. ATLAS' calorimeter system covers the rapidity range of up to $|\eta| \leq 4.9$. The electromagnetic calorimeter is based exclusively on liquid argon. This subsystem is therefore referred to as the "LAr Calorimeter". The hadronic calorimeter system uses in addition scintillating tiles technology. This one is referred to as "Tile Calorimeter".

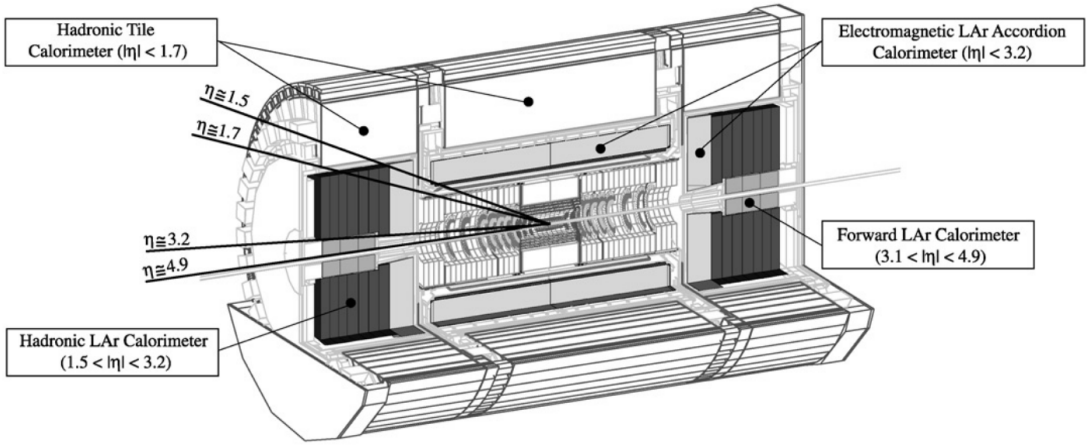

FIGURE 3.7: Schematic view of the ATLAS calorimeter systems [23]

The main component of the electromagnetic calorimeter is a lead/liquid argon sampling detector with accordion shaped electrodes. The absorber plates are lead based. The calorimeter is split into a "Barrel part" and two "End-Caps", where each end-cap is divided into an inner and outer coaxial wheel. The outer wheel covers a rapidity range of $1.375 \leq |\eta| \leq 2.5$, while the inner one covers a range of $2.5 \leq |\eta| \leq 3.1$. In the forward region $3.1 \leq |\eta| \leq 4.9$ a further LAr subsystem (The Forward Calorimeter (FCAL)) is placed. It consists of copper rods, parallel to the beam axis. A further LAr system is the "Hadronic End-Cap calorimeter (HEC)". It provides hadronic coverage between $1.5 \leq |\eta| \leq 3.2$, consisting of copper plate absorbers orthogonal to the beam axis.

All other hadronic calorimetry is done by the Tile system. This consists of everything below the rapidity range of $|\eta| \leq 1.6$, where the intrinsic radiation hardness of the LAr technology is not needed. The Tile calorimeter sits behind the solenoid coil and the electromagnetic calorimeter. The absorber material of this sampling calorimeter consists of iron, while scintillating tiles act as the active material. The hadronic forward calorimeter for the range $3.1 \leq |\eta| \leq 4.9$ sits just behind the corresponding electromagnetic FCAL.

The Muon System

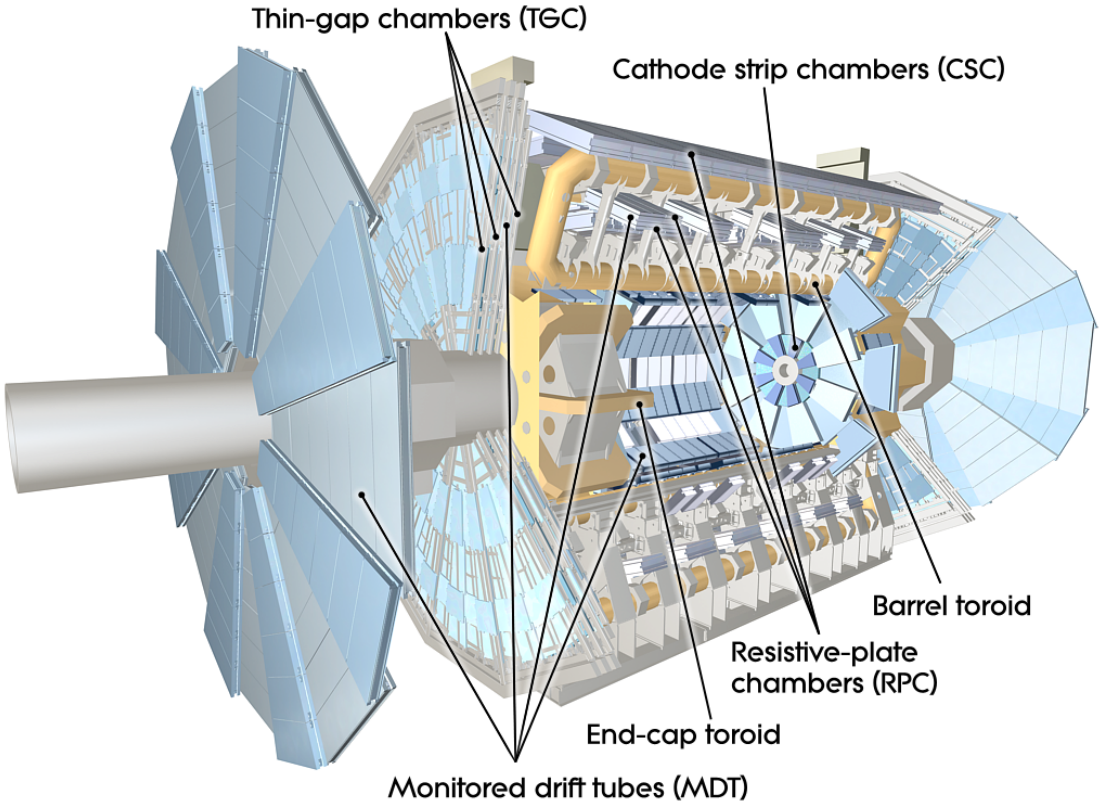

FIGURE 3.8: Schematic view of the ATLAS muon systems [24]

A muon spectrometer system is part of ATLAS' assembly, in order to measure high-momentum final state muons [25]. The momentum measurement is based on muon deflection by the three air-coil toroid magnets. For the rapidity range below $|\eta| \leq 1.0$, a large barrel magnet made up of eight coils, surrounding the hadronic calorimeter provides the magnet bending. For the rapidity range between $1.4 \leq |\eta| \leq 2.7$ this is achieved by two smaller end-cap magnets inserted in both

ends of the barrel toroid. In the transition range inbetween these two rapidity ranges, a combination of both fields is used for deflection.

Figure 3.8 shows a schematic layout of ATLAS with focus on the muon sub-systems. Three cylindrical layers are located around the beam axis, which provides track measurement capability in the barrel region. Three further stations are installed in the transition and endcap region vertically. The "Monitored Drift Tubes" (MDTs) provides a precise measurement of the muon tracks in the bending direction of the magnetic field over most of the total covered rapidity range. At large rapidities and close to the ATLAS interaction point, "Cathode Strip Chambers" (CSCs) are used which are able to cope with higher rates and under harsher background conditions.

The muon subsystems independent trigger system covers the rapidity range $|\eta| \leq 2.4$. "Resistive Plate Chambers" (RPCs) and "Thin Gap Chambers" (TGCs) are used in the barrel and end-cap region respectively.

3.2.1 Luminosity and Forward detectors

ATLAS consists of several sub-detector systems dedicated to luminosity determination and forward physics.

In the forward region we have LUCID (LUminosity measurement using Cherenkov Integrating Detector), used for determination of the luminosity. Another one is the ZDC (Zero-Degree Calorimeter), designed to detect forward neutrons and photons in heavy-ion collisions. Further out there are Roman Pot based detector systems AFP and ALFA for measurement of scattered protons under very small angles. All forward detector systems have symmetric setup on both sides from the interaction point.

The Beam Condition Monitor (BCM) is capable of providing luminosity information, however its main design purpose is to trigger on high rates, caused by instabilities in the beam. This detector is part of the LHC interlock system and can, when triggered and not masked, initiate the beam disposal procedure ("beam dump") in order to avoid damage to the inner ATLAS detectors.

The Minimum Bias Trigger Scintillators (MBTS) is a detector, located about 3.5 meter on both sides from the interaction point perpendicular to the beam direction, consisting each of an outer and inner ring with scintillator paddles. The purpose is to provide trigger on inelastic scattering processes during low luminosity pp-running. The MBTS has been upgraded since run I period and currently covers a rapidity range of $2.08 \leq |\eta| \leq 3.86$ [26].

3.2.2 The ALFA detector

ALFA stands for "Absolute Luminosity for ATLAS". ALFA is one out of two ATLAS Roman Pot detector systems, which was designed to measure elastic proton scattering under very small angles and infer from that the total *pp*-cross section as well as the applied luminosity directly from characteristics of the measured elastic differential cross-section.

The system is composed of four "Roman pot stations", which are installed in the LHC tunnel, about 240 meters around both sides from the ATLAS interaction point at the end of the straight LHC section. On either side from the interaction point, there are two ALFA stations, roughly eight meters apart. The in- and outgoing beams are separated into individual beam pipes on both sides before the ALFA stations as seen from ATLAS. The large distance to the ATLAS interaction point gives a good lever arm for the scattered protons to become separated from the beam itself. Each one of the four stations is equipped with a pair of tracking detectors, which can be mechanically inserted into the LHC beam pipe from both sides vertically. Mechanically, the upper and lower detectors of each station can approach each other up to one millimeter of distance (this will activate an anti-collision switch), however in practice the distance to the beam will be constrained by the extend of the beam itself and its surrounding halo. There are no LHC magnet systems between the station pairs in either side, hence a direct measurement of the local angle of the protons trajectory is measurable by comparing the measured positions for both adjacent detector stations.

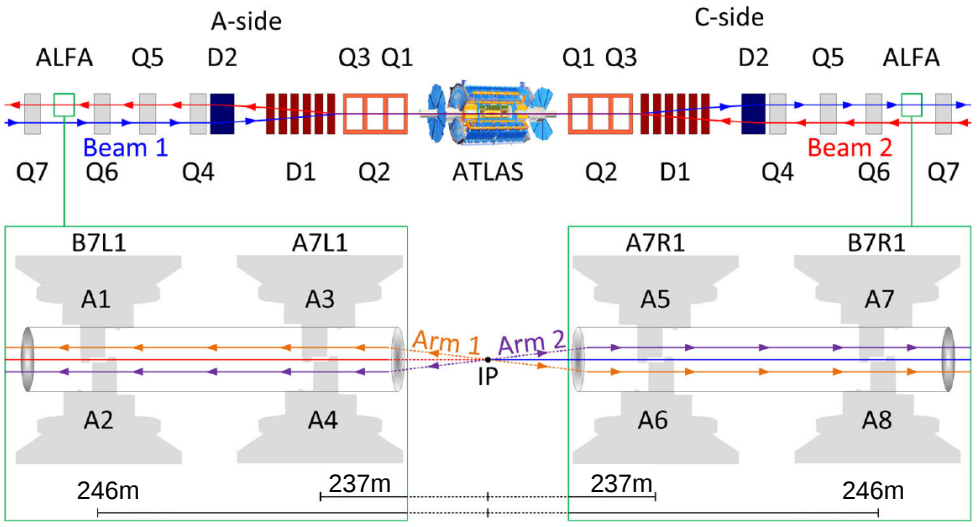

FIGURE 3.9: Overview of the eight ALFA detectors in the LHC tunnel relative to the ATLAS interaction point. Given are positions, orientations and naming scheme. [27]

Figure 3.10 shows a sketch of the individual detector components which are included in each of the ALFA stations. The beam passes inbetween the upper and lower detector. We have two types of detectors, one is called the "Main detector" (MD) used for the physics measurements, while associated with each MD is an "Overlap Detector" (OD), which, as the name implies, overlaps with the corresponding counterpart of the opposite detector, providing means of precise determination of the distance between both detectors as part of the alignment.

The MD uses scintillating fibers in order to determine the proton positions in the transverse (orthogonal) plane of the LHC beam. The fibers are glued on ten titanium plates. Figure 3.11 shows the arrangement of the fibers on one of those titanium plates. The remaining nine are identical for each detector, except that they are staggered slightly shifted against one another. On the front side of each of the plates we see 64 fibers which are tilted 45 degrees clockwise. When

assembled, the LHC beam will be passing just below the lower edge of the fibers in the picture. The fibers in the foreground of the picture are orthogonal to the fibers glued on this plate in the back behind the titanium plate which are glued 45 *anti*clockwise. The orthogonality provides a two-dimensional position resolution. The geometrical planes of this arrangement are called V-plane (for the clockwise arranged fibers) and U-Plane (for the anticlockwise arranged fibers).

The fiber layers are stacked without titanium inbetween the layers to reduce the occurrence of multiple-scattering processes in the detector which would reduce reconstruction efficiency. Each fiber has a square base area of $0.5 * 0.5\,\mathrm{mm}^2$. Upon proton traversing, they produce scintillation light with a peak intensity at 450 nm [29]. The fibers are cladded, so that most of the light produced in the fiber is trapped in there due to internal reflections. The fibers are further coated with aluminum in order to reduce cross-talk caused by escaping light propagating to a neighboring fiber. Both cladding and coating make up about 2.2% of the total layer width. The layer efficiency, meaning the probability that a passing proton will introduce measurable light in this layer, was determined to be around 90% in a test beam.

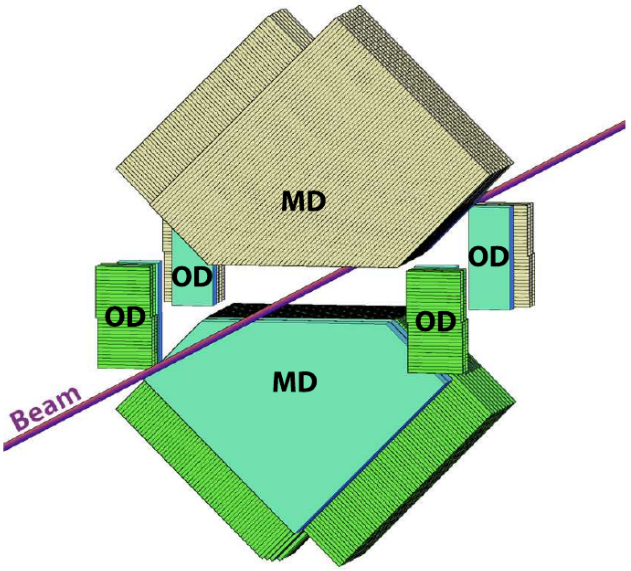

FIGURE 3.10: Schematic scetch of one ALFA station, comprised of a pair of main detectors and overlap detectors [28]

Each fiber layer is shifted by a tenth of the fiber width, which greatly enhances the resolution of the reconstructed tracks (see section 3.4).

The light induced in the fibers of each layer is measured by a 64-channel Multi-Anode Photo-Multiplier-Tube (MAPMT). Due to a persistent risk of cross-talk between neighboring channels in the MAPMT, a special mapping is used so that adjacent fibers are not read out by adjacent channels.

The "Overlap Detector" (OD) is shown in right hand side of figure 3.11. The

OD of each ALFA detector is split into a left and right hand part. They are constructed using the same type of scintillating fibers as the MD. For the ODs, only three fiber layers are staggered to give only a vertical position resolution of tracks. The fibers are cut on one end and terminated with a reflecting aluminum coating. On the other end, the fibers are connected to MAPMTs, just like the MD ones. Compared to the MD, there is an increased material budged from titanium between the fiber layers, enhancing the probabilities of multiple scattering and shower developments. The ODs purpose is to measured the distance between the two detectors per station and thus contribute to the "Alignment procedure", which will be outlined in section 3.4.3.

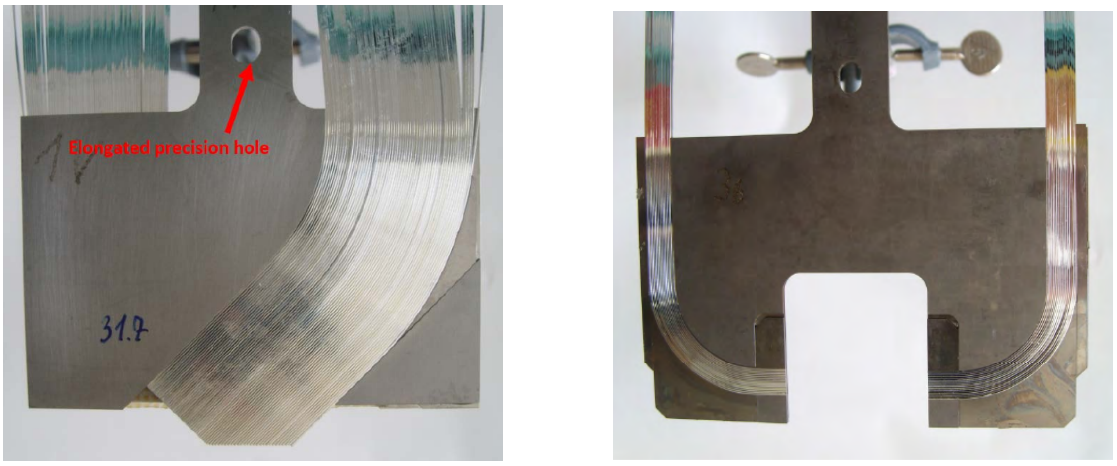

FIGURE 3.11: Picture of a titanium plate together with (left:) one layer of fibers in the V-Plane glued on the front of such and one layer of fibers in the U plane in the back and (right:) one layer of fibers for each side of the OD detector.

Roman Pot

In this section, the concept of a "Roman Pot" shall be explained as well as the procedure of placing the detectors into data taking position.

In order for the ALFA detectors to measure small angle scattering, they have to be placed as close to the LHC beam as possible. Figure 3.12 shows a mechanical support structure, called "Roman Pot" which will allow to do just that. The ALFA MD and OD detector-components are placed inside, which allows to separate the detector assembly from the ultra high vacuum of the LHC beam pipe. For data taking, the movable upper part of the structure of picture 3.12 is inserted into the beam pipe by a step motor with 5 μm step size. In order to place the upper

and lower detector of each station as close to the beam as possible, a "Beam Based Alignment" procedure (BBA) is used. In the first step, the coarse beam position and extend is estimated by readings of beam position monitor, beam emittance and the β-function. Using this information, an estimate of the final detector positions is calculated and the detectors are placed at that distance with some safety margin in order not to touch the beam itself. In a second step the detectors are, one by one, further inserted closer to the beam in very small steps. After some time, the thin Roman Pot window (shown at the top in the picture) starts touching the outer edges of the LHC beam and induces showers which are detected by the LHC beam loss monitoring system. The detector is then placed a bit away from the beam to ensure stable beam conditions and a good physics data taking position. The Roman Pot window thickness is only 200 μm small and the entire distance between the outer window edge (which faces the beam) and the edge of the MD detector is only about 450 μm in length. The Roman Pot interior has secondary vacuum conditions to reduce proton-air scattering and to reduce mechanical stress to the window, which would otherwise bend outwards and degrade achievable beam-distance. Due to the amount of solid matter the elastic protons have to pass through on their way through the inner ALFA station ("material budget"), position tracking resolution is naturally degraded at the outer stations by an order of 10%.

The entire beam based alignment procedure takes in the order of two to three hours to complete for all detectors.

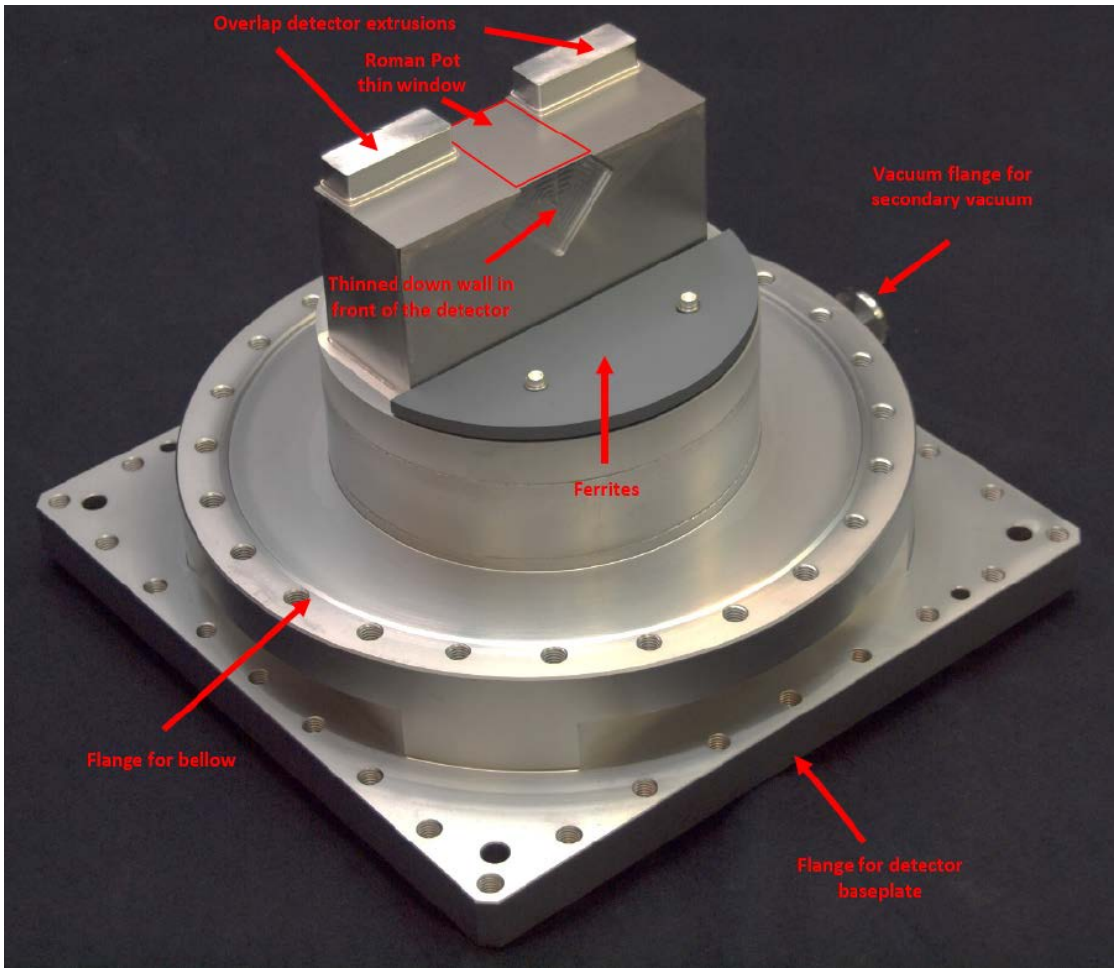

FIGURE 3.12: Picture of an ALFA Roman Pot. The MD sits inside the diamond shaped structure, while the ODs sit inside the extrusions on top to either side.

3.2.3 Coordinate systems and naming conventions

Figure 3.9 shows the overview of the ALFA detectors relative to the rest of ATLAS. Throughout the rest of this thesis, we will use the official LHC naming scheme to identify the individual ALFA detectors. These are the designations written in bold in the overview, so B7L1U, B7L1L, A7L1U, A7L1L, A7R1U, A7R1L, B7R1U, B7R1L. The designations are composed of B/A for outer/inner, L/R for left/right (as seen from someone looking from the center of LHC towards ATLAS) and U/L for upper/lower detector all respectively. The designation left/right from ATLAS is also known as A-side/C-side respectively. The 7 and 1 have no meaning for ALFA. They stem from the fact that ALFA is the 7th element in the LHC ring as

seen from interaction point 1, where ATLAS is located.

For reference of detectors and event constellations (coinciding track reconstruction in multiple detectors), we will from now on be using simplified drawings like the one in figure 5.5. This drawing shows schematically an elastic event. Due to momentum conservation, if a proton is elastically scattered upwards in direction of A-side (left side), then the counterpart has be have been scattered downwards on C-side (right side) and vice versa. We will refer to those constellations as "elastic (spectrometer) arm 1" and "elastic arm 2" respectively.

Proton track positions are reconstructed and safed in the "Detector Coordinate System" (DetCS) (see figure 3.13). The origin of this coordinate system corresponds to the "Precision hole" seen in previous figure 3.11 (left side). For the analysis, proton positions relative to the LHC beam center have to be calculated, so a translation and further a small rotation (exaggerated in figure) have to be performed. The procedure of determining those parameters is explained in section 3.4.3. This coordinate system will be referred to as "Beam Coordinate System" (BeamCS).

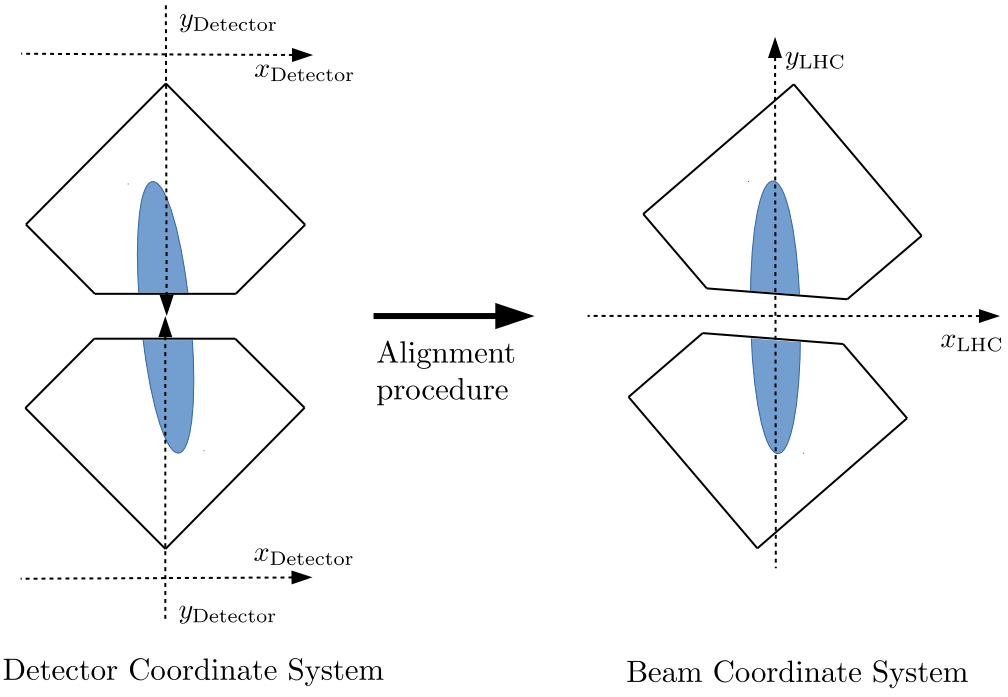

FIGURE 3.13: Schematic drawing of the "Detector coordinate system" (DetCS) and the "beam coordinate system"(BeamCS). Tracks are measured in the DetCS. The determination of the translation and rotation values to get from DetCS to BeamCS is called "Alignment procedure".

3.3 Data taking

3.3.1 Beam configuration and detector setup

The data used in this analysis were recorded in September 2016, divided into several LHC fills and several ATLAS runs. The overview of these runs is given in table 3.1.

TABLE 3.1: Overview of the datasets from the $\beta^* = 2.5\,\text{km}$ campaign

ATLAS run number	LHC Fill	Start Date	End Date
308979	5313	Mon Sep 19 2016 17:16:39	Tue Sep 20, 06:32:34
308982	5313	Tue Sep 20 2016 06:47:35	09:11:40
309010	5314	Tue Sep 20 2016 10:25:51	22:57:10
309039	5317	Wed Sep 21 2016 00:50:06	Thu Sep 22, 01:06:30
309074	5317	Thu Sep 22 2016 01:09:15	09:56:11,15,380,752
309165	5321	Thu Sep 22 2016 22:44:26	Fri Sep 23, 07:53:01
309166	5321	Fri Sep 23 2016 08:02:59	14:22:50

The dedicated low-luminosity LHC fills used a special beam optics setup with an unprecedented high $\beta^* = 2.5\,\text{km}$. This is a parameter of the betatron function $\beta(s)$ which gives the variation of the beam envelope as a function of the position s along the LHC ring. The beam had a center-of-mass energy of $\sqrt{s} = 13\,\text{TeV}$.
As in previous runs, after LHC filling and de-squeezing the beam to now $\beta^* = 2.5\,\text{km}$, the collision rates were optimized using the online-luminosity infrastructure of ATLAS. After that, the ALFA Roman Pots were aligned, using the beam based alignment procedure as described earlier. Before data recording, the LHC beams were "scraped", meaning that collimators in the beam pipe moved towards the beam in order to absorb the outer layers of the beam halo envelope.
After this procedure, elastic data were recorded. The collimators have been retracted to a position of 2.5σ for TCLA.Vs and 5.5σ for the TCP.H. The scraping procedure however had to be repeated continuously, due to the re-population of the beam halo envelope. In the order of every 35 to 90 minutes, the beam was scraped again. This required a lot of coordination with the experts from ATLAS inner detector, since for each scraping procedure, the pixel and SCT detectors had to be put on standby in order not to damage those because of the shower development from the beam scraping.

3.3.2 Trigger conditions and data streams

Each ALFA detector is equipped with a set of trigger tiles. Upon traversal of a proton, they create a signal which is sent to the Central Trigger Processor (CTP) of ATLAS. The individual trigger signals are combined to represent higher-level "structures". For the selection of elastic events, it is naturally convenient to have a trigger signal for the topology where detector activity is expected for both the elastic spectrometer arms. Hence two elastic triggers are defined:

$$\text{L1\_ALFA\_ELAST15} = (\text{B7L1U} \vee \text{A7L1U}) \wedge (\text{B7R1L} \vee \text{A7R1L}) \tag{3.1}$$

$$\text{L1\_ALFA\_ELAST18} = (\text{B7L1L} \vee \text{A7L1L}) \wedge (\text{B7R1U} \vee \text{A7R1U}) \tag{3.2}$$

also for background analysis, it is necessary to also record events, which do not have an elastic signature:

$$\text{L1\_ALFA\_ANY} = \text{B7L1U} \vee \text{B7L1L} \vee \text{A7L1U} \vee \text{A7L1L} \vee \text{A7R1U} \vee \text{A7R1L} \vee \text{B7R1U} \vee \text{B7R1L} \tag{3.3}$$

The recorded events were processed on Tier0, which for ALFA is basically the conversion of raw fiber hits into reconstructed track positions. Contrary to earlier data takings, these tracking information is not provided in the form of convenient ROOT-NTuple type files, but in a more general ATLAS xAOD format. The author has designed a conversion method and the classic-style NTuples are processed on private computing grid time in order to provide compatibility with established analysis code.

3.4 Track reconstruction

The spacial coordinate of the proton tracks passing through each detector are inferred from the activity pattern from the fiber structure. Due to the fiber arrangement in the u and v-plane, tracks are reconstructed in this coordinate system and have to be transformed into the detector coordinate system by a simple rotation:

$$\begin{pmatrix} x_{\mathrm{DetCS}} \\ y_{\mathrm{DetCS}} \end{pmatrix} = \begin{pmatrix} cos(45°) & -sin(45°) \\ sin(45°) & cos(45°) \end{pmatrix} \begin{pmatrix} v \\ w \end{pmatrix} \tag{3.4}$$

3.4.1 Tracking algorithm

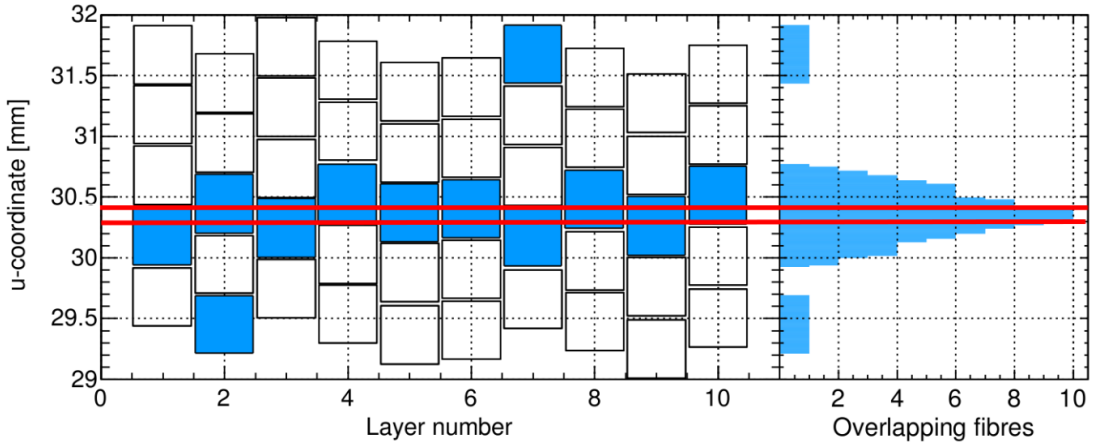

FIGURE 3.14: Schematic illustration of the track reconstruction exemplary in the U-plane. Lit up fibers are drawn in blue, fiber layers are shifted against each other hence the resulting overlap region (red lines) is used as reconstructed track position. Picture taken from [30]

The basic principle of track reconstruction is described in detail in [28] with some modification in [30]. For the track reconstruction it is assumed that protons pass through the detector perpendicular to the detector plane. This is true for protons originating from the LHC beam, but not for cosmic particles or decay products from radioactive activation of any material in the vicinity of the detector or the detector itself.

The track reconstruction principle is shown in figure 3.14 exemplary for the U-plane. Fibers from each layer in this picture are lit up by the passage of a

proton, drawn in blue. Due to the staggering of the layers, the proton must have passed in a region, where all layers show activation simultaneously. This region is shown as red borders, which give the position range, in which the proton will have equal probability to have passed the detector. Under ideal theoretical conditions, the position resolution would be $\frac{50}{\sqrt{12}}\,\mu$m which is however diminished by:

- Imperfect staggering of the layers
- Layer efficiency of only around 90 % meaning that there is about a 10 % probability that any layer will not give a signal even though the proton passed through it
- Diminishing position resolution on the outer stations due to interactions with detector material on the inner ones (multiple-scattering and showers)

As seen in figure 3.14 there are also two excluded fibers lit up. This shall symbolize the occurrence of cross-talk effects between MAPMTs. Also cross-talk between neighboring fibers is possible, which might also diminish the tracking resolution, if this increases the overlap region.

Figure 3.15 shows the fiber hit pattern of an elastic event in spectrometer arm 1 for run 309039. For each of the eight detectors, the fiber hit pattern is shown for both u and v-plane for each the individual layers. Lit fibers are symbolized with colored squares, where green squares means a fiber hit and black squares means fiber hit, which is used for the reconstruction of a given track, which is then symbolized with an arrow. The numbers above and below a given layer give the "layer multiplicity", meaning the number of lit up fibers in this layer. Overall we see a relatively clean elastic event in arm 1. There is no activity whatsoever in the opposite spectrometer arm 2, indicating the absence of any upstream showers. On A-side (B7L1U and A7L1U, to the upper left), we see a close to ideal fiber hit pattern. Most fiber hits are constraint to a single horizontal line, indicating the traversal of a proton perpendicular to the detector surface. Some negligible cross-talk (as indicated by isolated green colored fibers) is present which does

not influence track reconstruction in this case. Noticeable are also a few layers with no activity whatsoever indicating the non-perfect layer efficiency. On the C-side (A7R1U, to the lower right, inner) we see a fiber hit pattern a bit more interesting. Beside from again a very distinctive clear proton track, we have a non-perpendicular and thus non-reconstructed "side-track" apparently originating near the beginning of the detector. This is a candidate for a shower event, or some radioactive decay inside the detector. The hit pattern of the shower is completely discarded for the track reconstruction and it does not pose any problem in this case.

Independently of what the tracking algorithm provides, further requirements will be enforced for a given track to be considered as reconstructed ("Data quality cuts"): A track has to be reconstructed from three "good layers", whereas a layer is considered "good" if it has at most three lit up fiber in total. Further a track has to be reconstructed using at least three overlapping layer pairs in u and v-plane. This does not cure the intrinsic problem of showers, however it is very efficient in removing accidentally reconstructed background tracks. Shower occurrences will be the cause of many events which can not be fully reconstructed (by all four out of four detectors) and thus reduce the event reconstruction efficiency which determination will be the main focus of this work.

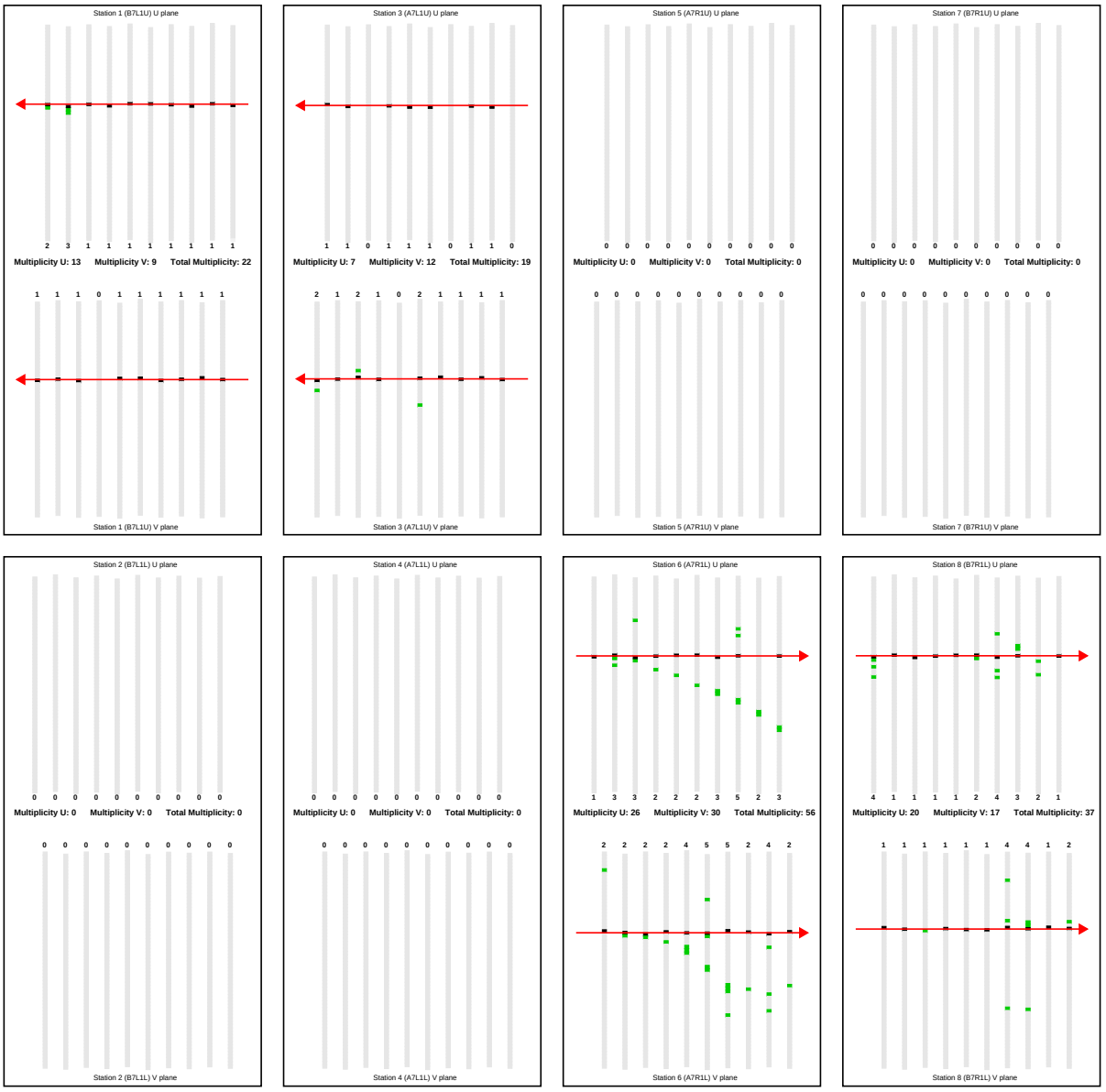

FIGURE 3.15: Example of track reconstruction from fiber hits. Shown are for all eight detectors (black borders) the u and v-plane with lit up fibers in either green (not used for track reconstruction) or in black (used to reconstruct a track). A7R1U shows in addition to the track a non-perpendicular path of a charged background particle.

3.4.2 Track matching

Sometimes, more than one track is reconstructed for a given detector. These can be pseudo-tracks as artifacts from shower events, or they may be genuine pile-up e.g. overlap of elastic events, beam halo and other diffractive processes. Figure 3.16 shows the fiber hit distribution of such an multi-track event from run 309039. Here, a genuine pile-up of two particles is observed. The tracks are cleanly separated with minor cross-talk and no showers. The presence of more than one reconstructed track in both u- and v-plane leads to a peculiar artifact in track reconstruction. Contrary to pixel-detectors, where the 2D-position of activity is measured directly, in the fiber based detector structure, the track position is inferred from the intersection of the u- and v-planes, where the track is located. Figure 3.17 demonstrates this process and the mentioned peculiarities.

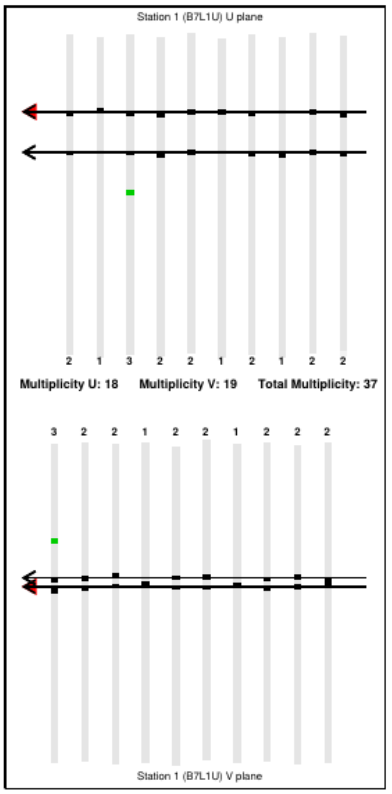

FIGURE 3.16: Example of a fiber hit structure for a clean multi-track event

Assuming two protons traverse the detector at places which are indicated by blue circles near the edge. This gives measurement of two v-coordinates as well as two measurements of u-coordinates, as indicated by red line. This gives however a total of four possible proton positions in the 2D-region, as indicated by the line

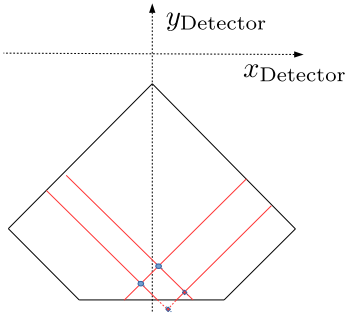

FIGURE 3.17: Schematic example on the "fake-track" construction in a multi-track event

intersections. We can see that for our example, in addition to the two real proton positions, two further "fake-tracks" are reconstructed. One of these is located even outside the fiducial volume of the detector below the edge.

For multi-track events, a procedure was invented in [28] in order to determine for a given set of coinciding tracks, that combination of tracks, which has the highest probability of being of elastic origin. This "best-track matching" exploits the fact, that elastic events have a back-to-back topology. The procedure was slightly simplified for this analysis. For each event it calculates for any possible track combination a χ^2:

$$\begin{aligned}\chi^2_u = &\left(\frac{1}{\sigma_{u,i}} \cdot (u_{A,i} + u_{C,i})\right)^2 + \\ &\left(\frac{1}{\sigma_{u,o}} \cdot (u_{A,o} + u_{C,o})\right)^2 + \\ &\left(\frac{1}{\sigma_{u,io,A}} \cdot (u_{A,o} - L_{io,A} \cdot u_{A,i})\right)^2 + \\ &\left(\frac{1}{\sigma_{u,io,C}} \cdot (u_{C,o} - L_{io,C} \cdot u_{C,i})\right)^2\end{aligned} \tag{3.5}$$

where L are the geometric lever arms between an inner station i and outer station o. The χ^2 given in equation 3.5 is calculated for both horizontal and vertical plane and summed up. The equation consists of four penalty terms. In the first term, the track positions of the inner detectors of A- and C-side are summed up. Due to back-to-back topology, those ideally should sum up to 0. It is divided by a σ which includes the position resolution of this extrapolation. The second term does the same, but for the outer detector pair. The third and forth term are extrapolations on respectively the same side from the inner to the outer detector. The track combination that minimize this χ^2 is taken as the elastic track combination candidate. When dealing with reconstruction efficiency analysis, where we do not have tracking information on all four detectors available, only those terms of equation 3.5 are summed up, for which tracks are available.

Contrary to the analysis in [28], where the Best-track candidates were determined

once in a dedicated analysis, the procedure was modified by the author to calculate the best-track candidate at runtime, which provides easier analysis workflow and can now handle best-track matching under for arbitrary data set skims and most importantly for different data quality cut settings.

3.4.3 Alignment

In order to transform the track position given in the DetCS into the physics relevant BeamCS, the exact detector positions relative to the beam have to be determined. This is done in a separate analysis in a data-driven procedure which determines the following values for each of the four ALFA stations:

- The distance between the upper and the lower detector
- The horizontal offset of both detectors center relative to the LHC beam center
- The vertical offset of the detector pair center relative to the LHC beam center
- The rotation of the detectors relative to the LHC beam planes.

At first, we show the basic principle on how the distance measurement is conducted in figure 3.18.

The distance measurement makes use of the overlap detectors. These are shown in orange in the sketch, which shows the detectors of one ALFA station from side view point. The Overlap detectors of both the upper and lower individual detector will overlap in the vertical plane when in data taking position, however have in the horizontal plane (not seen in projection) a far enough distance such that the beam itself does not endanger the detectors. Any particle in the outer beam halo or shower particle that traverses one OD perpendicular will also traverse the other one. From coinciding track positions of both ODs, a distance

value of the detector pair can be inferred.

The determination of the other alignment parameters relies on tracks measured in the MDs. For the horizontal offset alignment, a simple selection for elastic event is applied. The elastic event distribution in the horizontal plane is fairly Gaussian shaped, so a simple Gaussian fit can be applied and the offset of this distribution is the horizontal detector offset.

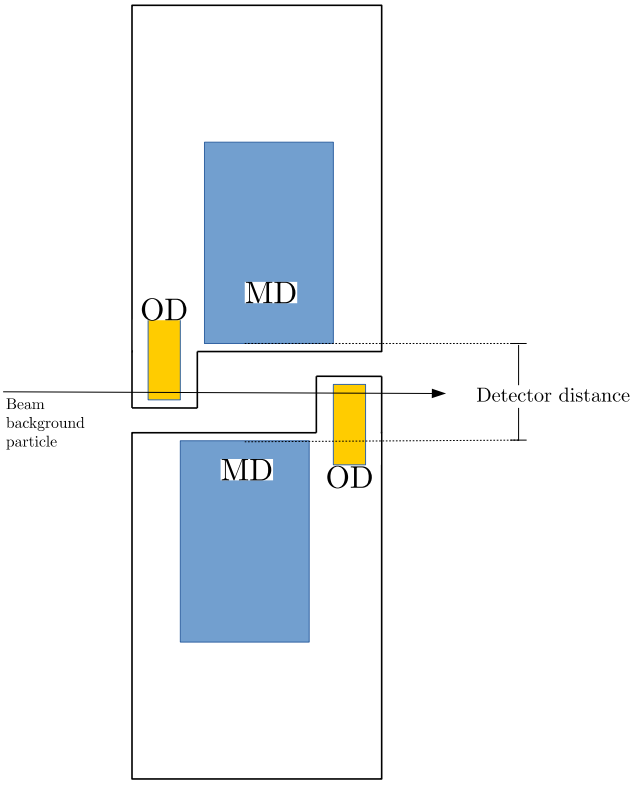

FIGURE 3.18: Principle of the detector distance measurement using the Overlap-detectors.

The vertical offset determination is not trivial. There are, contrary to the horizontal plane, obviously no tracking information available over the entire vertical range, since a gap has to be there, where the LHC beam is located. Instead, a "sliding windows"-technique is used. Again, elastic events are collected. Then a reference window (small range in y) is created on one of the detectors and its integral event count compared with the integral event count of the same window width in floating y-position in the opposite detector of the same station. For a vertical offset of zero, one would expect that for a given y-range, the same number of elastic events is observed in both the upper and lower detector. The difference of the position of that window gives the vertical offset. What makes this part of the analysis prone to uncertainty, is the fact that the upper and lower detectors are located in different elastic spectrometer arms, which we will later see have different efficiencies for elastic reconstruction. This fact has to be included as a scaling factor in this procedure.

At last, for each detector a relative rotation is determined relative to the LHC beam planes. This is done by dividing the elastic selection into windows in the vertical plane and for each window determining the center of the corresponding horizontal distribution. The shift of the horizontal distributions center along the vertical windows gives the rotation of the detector.

The alignment procedure is a separate analysis and was in an early stage at the time of this writing, hence only the basic ideas are displayed.

Chapter 4

Beam optics and t-reconstruction

The derivations from this chapter are taken from [31]. The drawings and illustrations are self made. The "beam optics" can be used to describe the trajectory of the protons in a particle accelerator. Dipole magnets along the LHC ring are used to deflect the protons in order to follow the shape of the LHC ring, where quadrapole magnets are used to keep the beam focused. A single quadrapole magnet can only focus the beam envelope in one plane, while defocussing it in the other. Hence a combination of these magnets is used to obtain a net focusing in both planes. A position along the ring is given by the coordinate s. Figure 4.1 visualizes an arbitrary value of s as a distance along the LHC ring between the interaction point of ATLAS towards an ALFA detector, where a local xy-coordinate system, orthogonal to the beam path is constructed.

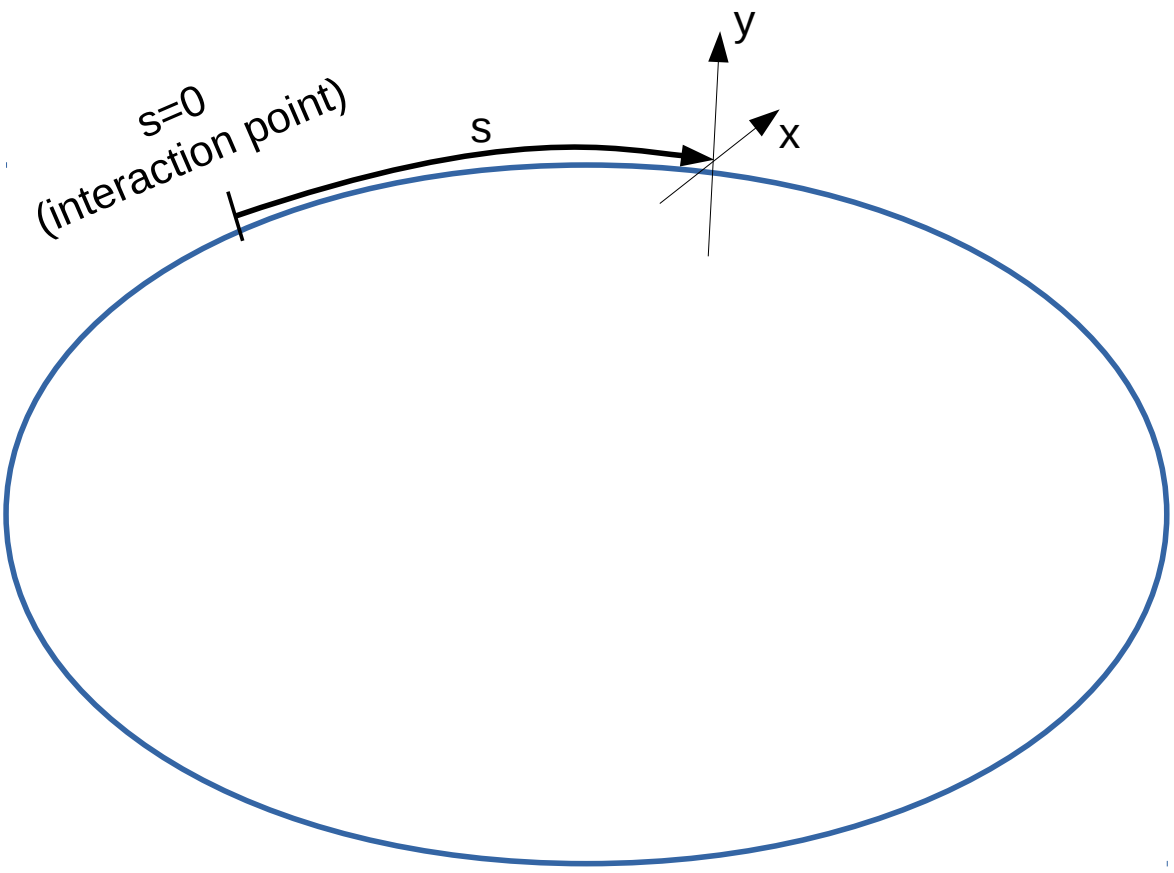

FIGURE 4.1: Illustration of the relations between accelerator ring, and the beam coordinate system. The value of s is the distance along the ring from the interaction point to the point of interest (in this case the ALFA detector).

Due to the alternating focusing and defocussing manipulations of the beam, its envelope oscillates, which is described by the betatron function $\beta(s)$. The form of this betatron function is determined by the magnet strengths. This determines, how a proton at the interaction point with a given position (the so called vertex-position) and a given angle (the scattering angle) is translated into a local position and local angle at the ALFA stations, which are about 240 meters away from the ATLAS interaction point with several sets of dipole and quadruple magnets in between.

4.1 Transverse beam dynamics

The Lorentz force governs the change in motion of a charged particle in an electromagnetic field, given in equation 4.1:

$$\vec{F_L} = q(\vec{E} + \vec{v} \times \vec{B}) \tag{4.1}$$

$\vec{F_L}$ is the force a proton with charge q and velocity $\vec{v}$ experiences under present of an electric field $\vec{E}$ and magnet field $\vec{B}$. In the LHC, electric fields are used by super conducting radio frequency cavities for proton acceleration, while magnetic fields are used for the bending and focusing. Transverse beam oscillations are given by the offset of the protons from a perfect reference orbit and are described by Hills' equation 4.2

$$\frac{d^2}{ds^2}u(s) + K(s)u(s) = 0 \tag{4.2}$$

with $u = x, y$ This is a set of second order linear differential equations in the horizontal and vertical planes x and y. They are similar to the equation of an harmonic oscillator, with the exception that $K(s)$ is not a constant. $u(s)$ describes the transverse offset from the reference orbit at beam position s, while $K(s)$ are focusing functions, which depend on the magnet system. At first order, the movements in x and y are independent, and u can be replaced with x and y. The first derivative $u'(s)$ gives the angle of the proton with respect to the reference orbit, which can be written as $\theta_u(s)$. The focusing functions are periodic $K(s) = K(s + \kappa)$, where κ is given by the distance between sets of focusing/defocussing magnet systems ("FODO"-cells). The value of $K(s)$ is positive in those parts of the accelerator ring, where focusing magnet systems are present, while it is negative for defocussing magnets. The solution of this differential equation results in sinusoidal oscillations with a variable amplitude and a varying wave number along s, constraint by an envelope as illustrated in figure 4.2.

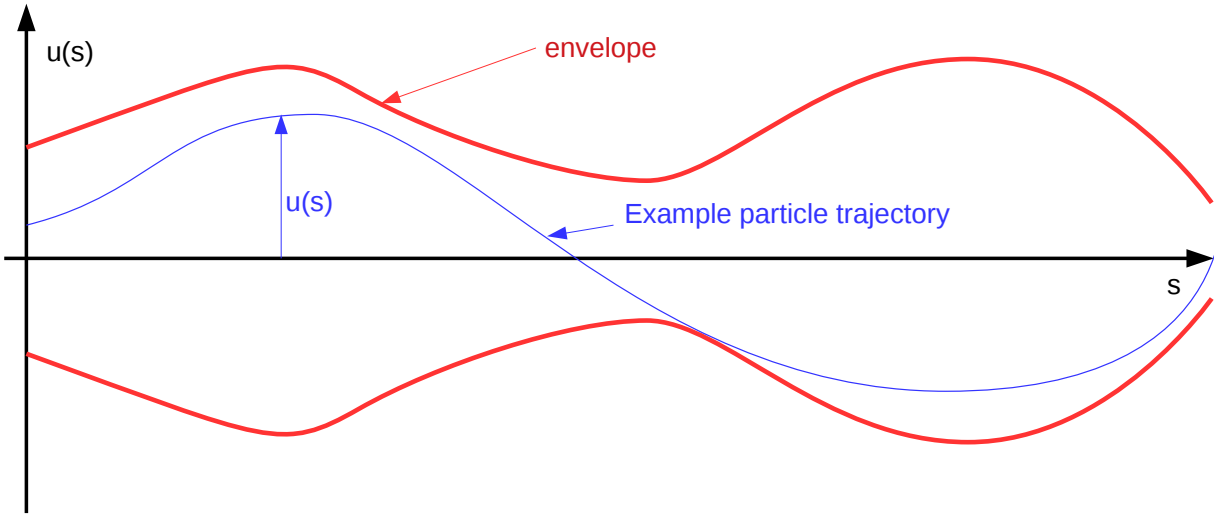

FIGURE 4.2: Illustration of a possible particle trajectory along the ring. All particles that are part of the stable beam traverse within an enveloping function.

The evolution of the offset from the reference orbit can be uniquely desribed by a matrix equation:

$$\begin{bmatrix} u(s) \\ u'(s) \end{bmatrix} = \begin{bmatrix} M_{u,11}(s) & M_{u,12}(s) \\ M_{u,21}(s) & M_{u,22}(s) \end{bmatrix} \cdot \begin{bmatrix} u* \\ u'* \end{bmatrix} \tag{4.3}$$

In equation 4.3, $u(s)$ is the position offset from the reference orbit at a given position s along the ring. $u'(s)$ is the local angle with respect to the reference direction at position s. The values can be calculated from initial conditions, which are given by the position and angle at the interaction point u^* and u'^* by multiplication with a so called "transport matrix". The transport matrix elements at a given position s can be calculated by multiplication of the individual transport matrices for each optically active element from the interaction point to position s.

For a solution to Hill's equation, we consider the following ansatz:

$$u(s) = a \cdot \omega(s) \cdot \cos\left(\psi(s) + \psi_0\right) \tag{4.4}$$

The ansatz resembles an harmonic oscillator with a s-dependent amplitude $\omega(s)$. Plugging 4.4 into 4.2 results to:

$$\left(\omega^{''} - \omega \cdot \psi'^2 + \omega \cdot K\right) \cdot \cos\left(\psi + \psi_0\right) - \left(2\omega^{'} \cdot \psi^{'} + \omega \cdot \psi^{''}\right) \cdot \sin\left(\psi + \psi_0\right) = 0 \quad (4.5)$$

in order for equation 4.5 to be true, the terms at sin and cos have to be zero simultaneously:

$$\begin{aligned} \left(\omega^{''} - \omega \cdot \psi'^2 + \omega \cdot K\right) &= 0 \\ \left(2\omega^{'} \cdot \psi^{'} + \omega \cdot \psi^{''}\right) &= 0 \end{aligned} \quad (4.6)$$

Integrating the second equation of 4.6 results in $\psi^{'} = 1/\omega^2$, where a further integration results in:

$$\psi(s) = \int_0^s \frac{d\bar{s}}{\omega^2(\bar{s})} \quad (4.7)$$

The differential equation in $\omega(s)$ is then given by:

$$\omega^{''} + K(s) \cdot \omega = \frac{1}{\omega^3} \quad (4.8)$$

which has a unique solution for $\omega(s)$. Defining the betatron function as $\beta(s) = \omega^2(s)$ gives the solution to Hill's equation in the form

$$u(s) = a \cdot \sqrt{\beta(s)} \cdot \cos\left(\psi(s) + \psi_0\right) \quad (4.9)$$

The locale angle (derivative in s) is given by:

$$u'(s) = \frac{a}{\sqrt{\beta(s)}} \cdot (-\alpha(s) \cdot \cos(\psi(s) + \psi_0) - \sin(\psi(s) + \psi_0)) \tag{4.10}$$

with

$$\alpha(s) = -\frac{1}{2} \cdot \beta'(s) \tag{4.11}$$

Equation 4.10 represents the parametrization of an ellipse with a constant area of

$$E = \pi a^2 = \pi\epsilon = \text{const.} \tag{4.12}$$

The form of the ellipse is a function of the coordinate s, which is determined by the optical function $\alpha(s)$, $\beta(s)$ and $\gamma(s)$, with $\gamma(s) = \frac{1+\alpha(s)^2}{\beta(s)}$. These are called the "Twiss-functions". Eliminating $\psi(s) + \psi_0$ in equation 4.9 gives:

$$\frac{u^2}{\beta} + \frac{(\alpha u + \beta u')}{\beta} = a^2 = \epsilon \tag{4.13}$$

Equations 4.12 and hence 4.13 are invariants of the motion and are called "Courant-Snyder-Invariant". The introduces quantities are visualized in figure 4.3 for an arbitrary phase space ellipse.

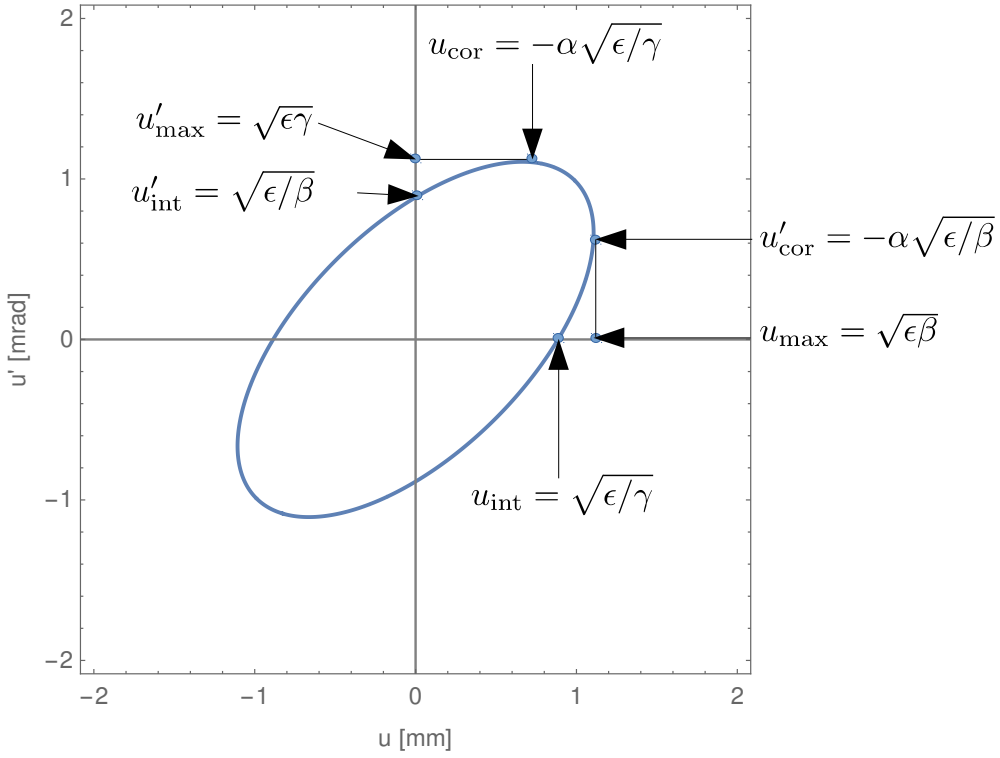

FIGURE 4.3: Example of a phase space ellipse in u (x,y) and u' (θ_x,θ_y) with critical quantities

We will now consider the functional dependency of the transport matrix given in equation 4.3 in terms of our introduced functions $\alpha(s)$,$\beta(s)$,$\gamma(s)$ and $\psi(s)$. The Twiss-Parameters at the interaction point $s = s_0 = 0$ shall be α^*,β^* and γ^*. At our location of interest at s, the Twiss-Parameters shall be α,β and γ. The phase advance of the betatron function between s_0 and s shall be ψ. In order to substitute the dummy parameters M_u from equation 4.3, we consider the general solution of Hill's equation in the form

$$u(s) = \sqrt{\epsilon}\sqrt{\beta(s)}\cos(\psi(s) + \psi) \tag{4.14}$$

$$u'(s) = \frac{-\sqrt{\epsilon}}{\sqrt{\beta(s)}}\left(\alpha(s)\cos(\psi(s) + \psi) + \sin(\psi(s) + \psi)\right) \tag{4.15}$$

using the trigonometric substitution $\sin(a+b) = \sin(a)\cos(b) + \cos(a)\sin(b)$ and $\cos(a+b) = \cos(a)\cos(b) + \sin(a)\sin(b)$ we expand:

$$u(s) = \sqrt{\epsilon}\sqrt{\beta(s)}(\cos(\psi(s))\cos(\psi) - \sin(\psi(s))\sin(\psi)) \tag{4.16}$$

and for the derivative:

$$\begin{aligned} u'(s) = \frac{-\sqrt{\epsilon}}{\sqrt{\beta(s)}} (\alpha(s)\cos(\psi(s))\cos(\psi) - \\ \alpha(s)\sin(\psi(s)+\psi)\sin(\psi(s)+\psi) + \\ \sin(\psi(s))\cos(\psi(s)) + \\ \cos(\psi(s))\sin(\psi)) \end{aligned} \tag{4.17}$$

At the interaction point, we set $s(0) = 0$, $\psi(0) = 0$ and $\beta(0) = \beta^*$ and obtain:

$$\cos(\psi) = \frac{u_0}{\sqrt{\epsilon\beta^*}} \tag{4.18}$$

and

$$\sin(\psi) = -\frac{1}{\sqrt{\epsilon}} \left(u_0' \sqrt{\beta^*} + \frac{a_0 u_0}{\sqrt{\beta^*}} \right) \tag{4.19}$$

inserting in 4.16 and 4.17 gives:

$$\mathbf{u}(\mathbf{s}) = \sqrt{\frac{\beta(s)}{\beta^*}}(\cos(\psi(s)) + \alpha_0 \sin(\psi(s))) \cdot \mathbf{u_0} + \sqrt{\beta(s)\beta^*}\sin(\psi(s)) \cdot \mathbf{u_0'} \tag{4.20}$$

and

$$\mathbf{u}'(\mathbf{s}) = \left(\frac{\alpha_0 - \alpha(s)}{\sqrt{\beta(s)\beta^*}} \cos(\psi(s)) - \frac{1 + \alpha(s)\alpha_0}{\sqrt{\beta(s)\beta^*}} \sin(\psi(s)) \right) \mathbf{u}(\mathbf{0}) + \sqrt{\frac{\beta^*}{\beta(s)}} (\cos(\psi(s)) - \alpha(s)\sin(\psi(s))) \cdot \mathbf{u}'(\mathbf{0}) \tag{4.21}$$

Equations 4.20 and 4.21 can be combinedly written in matrix form:

$$\begin{bmatrix} u(s) \\ u'(s) \end{bmatrix} = \begin{bmatrix} \sqrt{\frac{\beta(s)}{\beta^*}} (\cos(\psi(s)) + \alpha_0 \sin(\psi(s))) & \sqrt{\beta(s)\beta^*} (\sin(\psi(s)) \\ \left(\frac{\alpha_0 - \alpha(s)}{\sqrt{\beta(s)\beta^*}} \cos(\psi(s)) - \frac{1+\alpha(s)\alpha_0}{\sqrt{\beta(s)\beta^*}} \sin(\psi(s)) \right) & \sqrt{\frac{\beta^*}{\beta(s)}} (\cos(\psi(s)) - \alpha(s)\sin(\psi(s))) \end{bmatrix} \cdot \begin{bmatrix} u* \\ u'^* \end{bmatrix}$$

This relates the position and angle of the proton at the detector stations u, u' to the vertex position u^* and scattering angle u'^* at the interaction point using knowledge of the values of the beam evolution functions at the detector stations.

4.2 $\beta^* = 2.5\,\mathrm{km}$ design beam optics

Nominal LHC beam optics settings are not suitable for measuring elastically scattered protons. For nominal, "collision optics" settings ($\epsilon = 3.75\,\mu\mathrm{m}$ and $\beta^* = 0.55\,\mathrm{m}$) the resulting beam divergence is with around $30\,\mu\mathrm{rad}$ about twice as high as the smallest vertical scattering of the elastic protons that has to be covered ($\theta_y < 15\,\mu\mathrm{rad}$) for measurement of the total cross section and the nuclear slope parameter and even bigger, compared to the scattering angles needed to be accessible for ρ-measurement ($\theta_y \approx 5\,\mu\mathrm{rad}$). To make the angular domain required for these three measurements accessible for the Roman Pot Systems, a special beam optics setting is used with a β^*-value of $\beta^* = 2.5\,\mathrm{km}$.

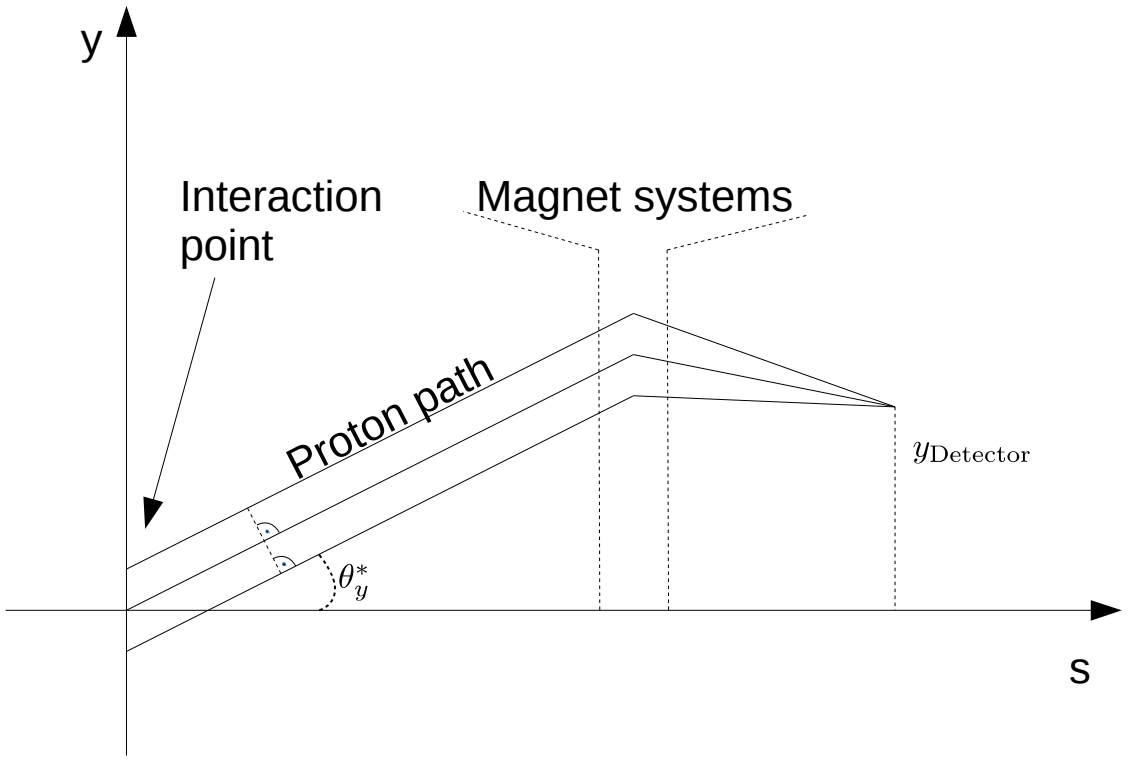

FIGURE 4.4: Illustration of the principle of "parallel to point" focusing, used in the special high β^*-optics in the vertical beam plane. All protons with any specific scattering angle at the interaction point are transported to the same position at the ALFA detector stations, regardless of the exact vertical position of the interaction in ATLAS.

4.3 t-reconstruction

As derived in the preceding section, we now have a way to infer from the measured proton positions u and local angles u' at the detector the vertex positions u^* and scattering angles u'^* at the interaction point. In order to obtain the differential elastic cross section, which is basically a measure of how many protons scatter at a certain momentum transfer t, we need to calculate from determined scattering angles this momentum transfer. Those quantities are related by:

$$t = -(p\theta^*)^2 = -\left(p\sqrt{(\theta_x^*)^2 + (\theta_y^*)^2}\right)^2 = -p^2\left((\theta_x^*)^2 + (\theta_y^*)^2\right) \tag{4.22}$$

where p is the beam energy. The formula 4.22 is valid for small angles. Now, we will take a look at the four methods of t-value reconstruction that are available and have been used in the past and emphasis minor modifications due to limitations of the $\beta^* = 2.5\,\mathrm{km}$ beam optics.

Subtraction Method The Subtraction Method is the nominal method used for t-value reconstruction. It exploits the knowledge, that any two elastically scattered protons originated from the same vertex position:

$$u_A^* = u_C^* \tag{4.23}$$

Further, the scattering angle of each proton is assumed to be the same, even though this is only approximately true, due to non-zero beam divergence:

$$\theta_A^* \approx \theta_C^* \tag{4.24}$$

The approximate nature of 4.24 results in slightly reduced resolution of the reconstructed scattering angle later on. The high-β^* beam optics results in a beam divergence that is significantly smaller than the smallest elastic scattering angle that can be measured. In turn it means, that the beam size at the ATLAS interaction point is larger than for nominal collision optics. With the special optics, the beams collide at the interaction point basically without crossing angle (quasi-parallel beams, described by $\alpha^* \approx 0$. Critical for this optics are the values for the phase advance at the detector stations, which is $\psi_y = 90°$ in the vertical plane, resulting in parallel-to point focusing. It is near $\psi_x = 180°$ in the horizontal plane. The high-β^* optic is designed to maximize the effective lever arm in the vertical plane. Due to this parallel-to-point focusing, as illustrated in figure 4.4 the vertical position of the proton at the detector stations only depend on the scattering angle at the interaction point:

$$y(s) = \sqrt{\beta_y(s)\beta_y^*}\sin(\psi_y(s)) \cdot y'^* = \sqrt{\beta_y(s)\beta_y^*} \cdot y'^* = \sqrt{\beta_y(s)\beta_y^*} \cdot \theta_y^* \tag{4.25}$$

from this, the scattering angle can be expressed as a function of the measured position and an "effective lever arm for a given detector station":

$$\theta_y^* = \frac{y_{\text{det}}}{L_{\text{eff,y,det}}} \tag{4.26}$$

The effective lever arm is basically the virtual distance between the interaction point and the detector station, imagining that no magnet systems were present.

The subtraction method uses the relationship given in equation 4.20. Using a pair of proton position measurement on each side (A,C) from the interaction point and taking the difference, one gets the following expression:

$$u_A - u_C = M_{11,\text{A}} u^* + M_{12,\text{A}} \theta_u^* - M_{11,\text{C}} u^* + + M_{12,\text{C}} \theta_u^* \tag{4.27}$$

due to the fact, that M_{11} is small and almost equal for both beams, eliminating the vertex position, equation 4.27 simplifies to:

$$u_A - u_C = (M_{12,\text{A}} + M_{12,\text{C}}) \cdot \theta_u^* \tag{4.28}$$

The to be calculated scattering angle is then finally given by:

$$\theta_u^* = \frac{u_A - u_C}{(M_{12,\text{A}} + M_{12,\text{C}})} \tag{4.29}$$

This value is used both for the horizontal and vertical plane, as well as for both the inner and outer detector station pair. To utilize the information we have from both inner and outer detector station pair, we modify equation 4.22 and substitute the scattering angles with the average values, we obtain from the inner and outer detector station pair:

$$t = -p^2 \left(\frac{(\theta_{x,i}^*)^2 + (\theta_{x,o}^*)^2}{2} + \frac{(\theta_{y,i}^*)^2 + (\theta_{y,o}^*)^2}{2} \right) \tag{4.30}$$

For the $\beta^* = 2.5\,\text{km}$ optics however, we have the peculiarity that the effective horizontal lever arms for the inner detector station pair is too small, to give a reliable contribution to the scattering angle reconstruction. Therefore, the "Subtraction Light" method is used, utilizing only the horizontal information of the outer station pair:

$$t = -p^2 \left((\theta^*_{x,o})^2 + \frac{(\theta^*_{y,i})^2 + (\theta^*_{y,o})^2}{2} \right) \tag{4.31}$$

Local angle method

The local angle method utilizes the second row of the transport matrix, written out in equation 4.21. Exploiting the back-to-back topology, we again take a look at the difference in the measurements from A- and C-side, this time however for the local angle of the proton:

$$\theta_{\text{u,A}} - \theta_{\text{u,C}} = M_{21,\text{A}} u^* + M_{22,\text{A}} \theta^*_u - M_{21,\text{C}} u^* - M_{22,\text{C}} \theta^*_u \tag{4.32}$$

Again, the vertex position term proportional to M_{21} is neglected, resulting in:

$$\theta^*_u = \frac{\theta_{\text{u,A}} - \theta_{\text{u,C}}}{M_{22,\text{A}} + M_{22,\text{C}}} \tag{4.33}$$

The local angles in equation 4.33 is measured simply by taking the difference in the position measurement from outer to inner station pair, divided by the geometric distance ($d \approx 8.26\,\text{m}$, no optically active LHC systems are inbetween the station pair on either side):

$$\theta_u = \frac{u_o - u_i}{d} \tag{4.34}$$

The t-value is calculated basically as in equation 4.30, however this time without averaging, since only one t-value can be reconstructed per event with this method, since only one local angle can be measured per side.

This method has an advantage in the horizontal plane, since the value of the matrix element M_{22} is proportional to the sine of the phase advance, giving less sensitivity to uncertanties on the exact phase advance ψ.

Local Subtraction Method The "Local Subtraction Method" starts from the relationships given by these two equations:

$$u_{\mathrm{S,i}} = M_{11,\mathrm{S,i}} u^* + M_{12,\mathrm{S,i}} \theta_u^* \tag{4.35}$$

for the inner station on side $S = (A, C)$ and:

$$u_{\mathrm{S,o}} = M_{11,\mathrm{S,o}} u^* + M_{12,\mathrm{S,o}} \theta_u^* \tag{4.36}$$

for the outer stations accordingly. Equations 4.35 and 4.35 share two unknown quantities, namely the vertex position u^* and scattering angle θ_u^*. Solving for the scattering angle by eliminating the vertex position gives:

$$\theta_S^* = \frac{M_{11,\mathrm{S,o}} u_{\mathrm{S,i}} - M_{11,\mathrm{S,i}} u_{\mathrm{S,o}}}{M_{11,\mathrm{S,o}} M_{12,\mathrm{S,i}} - M_{11,\mathrm{S,i}} M_{12,\mathrm{S,o}}} \tag{4.37}$$

This method however utilizes the matrix element M_{11}, it is more sensitive to uncertainties in the exact optics. As indicated by the index S, two t-values can be calculated per event, which are averaged again as in equation 4.30.

Lattice method This method uses in the inversion of equation 4.3 to calculate the scattering angle from a position and local angle measurement directly:

$$\begin{bmatrix} u^* \\ \theta^* \end{bmatrix} = M_u^{-1} \cdot \begin{bmatrix} u \\ \theta_u \end{bmatrix}$$

where M_u^{-1} is the inversion of the transport matrix, which can be easily calculated using Cramer's rule

$$M_u^{-1} = \frac{1}{M_{11}M_{22} - M_{12}M_{21}} \begin{bmatrix} M_{22} & -M_{12} \\ -M_{21} & M_{11} \end{bmatrix} \tag{4.38}$$

With this method, four t-values can be calculated for each event. Again, the average is taken as the final value.

Chapter 5

Data analysis

5.1 Event selection

The elastic scattering data used in this analysis were recorded in several LHC fills. ATLAS recorded the data in several datasets as shown in table 3.1.

The first level of event selection is performed on a Luminosity Block (LB) basis. Any time period where an LHC beam scraping was in progress was excluded from the data analysis. From the remaining LBs, those where discarded which have a duration of less than 60 seconds, have a dead-time fraction above five percent or for any other reason have too small amount of data.

5.1.1 Elastic trigger conditions

Elastic events are selected by scanning for recorded events where the "Level 1 ALFA Elastic trigger 15" or "Level 1 ALFA Elastic trigger 18" trigger item bit is set. Respectively, for elastic spectrometer arm 1 and 2 those bits are set, if any one of the two main detector trigger tiles have fired on each side from the ATLAS interaction point. The background templates later in the analysis are selected by vetoing on those trigger items and select for events with single side trigger activity.

5.1.2 Fiducial cuts

Fiducial cuts are applied separately for all detectors. First, the vertical position of tracks are required to be at least 60 μm from the detector edge, which faces the LHC beam. These edge cuts ensure uniform track reconstruction efficiency and suppress some of the background which is located near the beam.

Second, a cut is applied on the upper vertical range. This so called beam screen cut is put 1 mm away (towards the beam) on a position, where LHC beam screens cast a "shadow" on the ALFA detectors. The purpose of the beam screen cut is to avoid contamination of shower events originating at the beam screens. The elastic yield on those high vertical positions is in any case marginal.

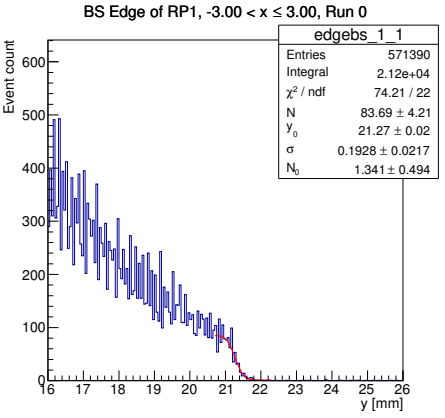

FIGURE 5.1: Example of beam screen fit on detector B7L1U for run 309166. The blue line indicates the elastic data, while the red curve is the fitted beam screen position.

To determine the beam screen positions, a fit has been performed to the vertical track position data. As in previous analysis, the convolution of a Gaussian with a Heaviside step function was used with floating parameters for the transition position (which resembles the beam screen position), the normalization and the degree of smoothness of transition (corresponds to the width of the Gaussian):

$$f(y, N, y_0, \sigma) = N * \int_{-\infty}^{\infty} H(a')g(a' - a)\,\mathrm{d}a'. \tag{5.1}$$

$$= \frac{N}{2}\left[1 + \mathrm{erf}\left(\frac{a}{\sigma\sqrt{2}}\right)\right] \tag{5.2}$$

Here, N is the normalization, erf() is the error function, $a = y - y_0$ where y_0 is the to be determined beam screen position and σ is the smoothness of the transition.

The functions

$$f^{+}_{\text{beam-screen}} = N_0 + \frac{N}{2}\left[1 + \text{erf}\left(\frac{a}{\sigma\sqrt{2}}\right)\right] \tag{5.3}$$

$$f^{-}_{\text{beam-screen}} = N_0 + N - \frac{N}{2}\left[1 + \text{erf}\left(\frac{a}{\sigma\sqrt{2}}\right)\right] \tag{5.4}$$

are fitted to the y-track-distributions in upper and lower detectors respectively. An example is shown in figure 5.1. A small track-count offset N_0 is allowed in the fitting procedure for the range beyond the relevant y-range. For the 2016 data, the obtained beam screen positions are provided in Table 5.1. For the data analysis, a safety margin of one millimeter was subtracted from the absolute numbers obtained in the fit. The variation of this safety margin was conducted as part of the systematic analysis, which however has negligible impact on the results as we will see later on, since there are not many elastic events with tracks near the beam screen position.

Run	B7L1U	B7L1L	A7L1U	A7L1L	A7R1U	A7R1L	B7R1U	B7R1L
308979	21.2	-20.9	22.4	-22.0	21.9	-22.3	20.9	-21.2
308982	21.3	-20.9	22.3	-21.9	22.0	-22.5	21.0	-21.2
309010	21.3	-21.0	22.5	-22.0	22.1	-22.4	21.1	-21.3
309039	21.1	-20.9	22.3	-22.0	22.0	-22.3	21.0	-21.2
309074	21.1	-21.0	22.3	-22.0	22.2	-22.3	21.0	-21.2
309165	21.3	-21.0	22.2	-22.0	22.1	-22.3	21.0	-21.2
309166	21.3	-21.0	22.4	-22.0	22.1	-22.3	21.0	-21.2

TABLE 5.1: Determined beam screen positions in millimeters per detector per run.

Correlation	$\sigma_1[mm]$	$\sigma_2[mm]$	$\theta[rad]$
xLxRi	0.91	1.015	0.761
xLxRo	0.84	3.92	0.783

TABLE 5.2: Elliptic event selection cuts for the horizontal track correlations x_A vs. x_C for each the two inner (i) and outer (o) detector pairs opposite from the interaction point

5.1.3 A-side C-side coplanarity cuts

Elastic scattering happens in back-to-back configuration, meaning that the spacial positions of the proton tracks on one side from the interaction point have opposite sign compared to the tracks on the other side. Background on the other hand has no causal back-to-back configuration, hence several cuts that exploit the back-to-back configuration can be applied to the event selection to help suppress background. Figure 5.2 shows exemplary for arm 1 in run 309039 the left right correlations of track positions in the horizontal plane. The elastic events are concentrated in the central region near small x-values. Due to the nature of the back-to-back scattering, the track positions are anti-correlated and a suitable elliptic selection cut was chosen to separate elastic events from the uncorrelated background. The cut shape and size are obtained from Monte Carlo simulation and set to $3.5\,\sigma$, in order to include more than 99 % of the elastic events. The semi axes and rotations of the ellipses are given in table 5.2. Due to a small lever arm in the inner stations in the horizontal plane, the elastic events in these stations are less correlated and hence the selection ellipse looks more circular.

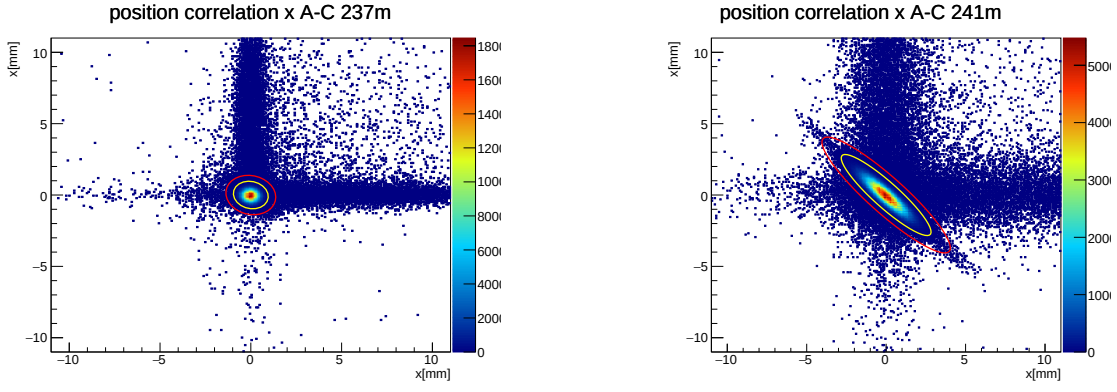

FIGURE 5.2: Horizontal left right track correlations and the applied event selection cut as a rotated central ellipse (yellow).

The same kind of cuts are applied to the vertical track positions. Here the elastic back-to-back scattering shows as narrow bands of anti-correlated vertical track positions. A cut of $\pm$ 1 mm is applied on either side of the central band. The events outside these constraints are treated as background and are cut away. Figure 5.3 shows the correlations in the vertical plane.

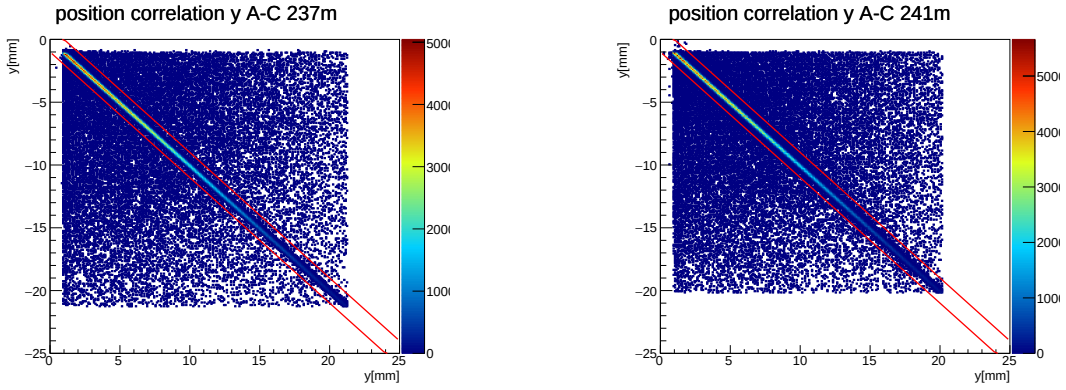

FIGURE 5.3: Vertical left right track correlations and the applied event selection cut as displaced linear cuts (red).

5.1.4 Local position angle correlation cuts

The main correlation which is used to filter background events is the local horizontal position vs. local horizontal angle correlation as shown on the left hand plot of figure 5.4. The local angle is calculated by taking the position differences between the track(s) in the outer and inner detectors and taking the spacial detector station distances into account. Similar to the previously discussed left-right-correlation, again here the elastic tracks concentrate on a positively correlated ellipse at the central region. There are several background contributions visible which we divide into "off-orbit" and "off-momentum" background-regions, which are highlighted in figure 5.4 with blue and red borders respectively. The "off-orbit" background is composed mainly of beam-halo-protons, which are protons that escape the central beam region and continue on a few unstable revolutions around the LHC ring before they are absorbed by the collimation system. Also reaction products from interactions of beam with collimators appear here. We see those contributions as horizontal and vertical bands which are

Correlation	$\sigma_1[mm]$	$\sigma_2[\mu rad]$	$\theta[rad]$
x vs. θ_x	0.686	248.85	-2.79E-3

TABLE 5.3: Elliptic event selection cuts for the horizontal position (x) vs. local angle (tx) correlation

completely uncorrelated in either position or in local angle.

The second background class in this correlation, the "off-momentum"-background, is composed of any protons which loose energy due to interactions, which shift them to narrower orbit radii around the LHC ring and hence those protons are located at positive x values in the correlation plot as a "tail" in the upper right hand quadrant. The semi axis and rotation of the central elastic contribution on which is cut is given in table 5.3.

The cut on the position angle correlation in the vertical plane is now used in this analysis for elastic event selection contrary to earlier $\beta^* = 90\,\text{m}$-analysis, since we see an otherwise irreducible background contribution near the detector edge, which will not contaminate the golden elastic sample significantly, however would become problematic later on in the reconstruction efficiency determination.

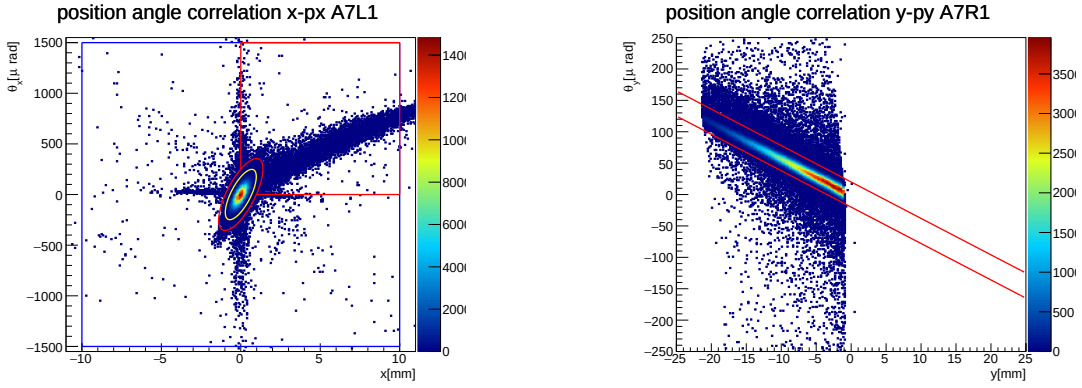

FIGURE 5.4: Position vs. local angle correlations for A-side. The left hand plot shows the correlation in the horizontal plane. Most of the elastic events are present within the central yellow 3.5σ ellipse. Everything outside the red 5.0σ ellipse is considered background. The cut for the elastic selection is chosen to be within the yellow 3.5σ ellipse. The upper right quadrant (red bordered) is defined as the "off-momentum" background region, while the remaining three quadrants (blue borders) are defined to be the "off-momentum" regions. The right hand plot shows the same correlation in the vertical plane. Here the elastic selection region is inbetween the red lines.

5.1.5 Summary after all selection cuts

Table 5.4 shows a run-by-run summary of the event cut flow for the selected "golden" elastic events. The term "golden" in this context is used to denote elastic events, where tracks in all four detectors of an elastic spectrometer arm were reconstructed. The successive decrease in remaining elastic events is shown, leading to a pre-final number of elastic event candidates. This number still contains a small fraction of background. This background is comprised of such background events which intersect the elastic event selection core in all correlation cuts previously introduced simultaneously.

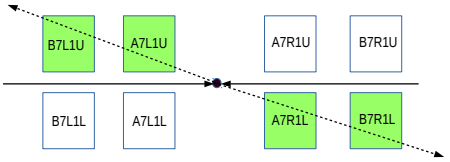

FIGURE 5.5: Schematic illustration of elastic scattering in spectrometer arm 1. Detectors from which track reconstruction was possible are drawn in green

At this point it shall be pointed out that for spectrometer arm 1 we end up with more elastic events than with arm 2. This is due to an interplay of causes. Aside from small contributions from acceptance differences between the arms due to asymmetric detector positioning around the beam, the main cause is from different reconstruction efficiency between the arms, which shall be examined in detail later in the section about the reconstruction efficiency.

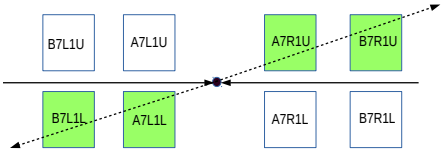

FIGURE 5.6: Schematic illustration of elastic scattering in spectrometer arm 2. Detectors from which track reconstruction was possible are drawn in green

For a very small fraction of the events, elastic pile-up was observed. This means that we have a coincidence of two independent elastic scattering events into the two spectrometer arms each. The per-run counts of those occurrences are listed in table 5.5. Those events are very rare due to the low mean number of interactions per LHC bunch crossing (μ-parameter). Same-arm-pileup clearly happens also, which however will not be directly measured in this analysis. This is a result by the way

multi-track events are handled, where only that track combination will be further analyzed which resembles most closely a back-to-back scattering constellation. For concurrent elastic events in one arm, one constellation will pass the track matching over the other one(s) due to e.g. finite detector resolution effects. For differential cross section normalization the measured amount of inter-arm-pileup will be used as zero-order estimate of the intra-arm-pileup by adding the observed inter-arm pileup to the number of number of elastic events per arm. In the case of intra-arm pile-up, only one elastic event constellation is observed, namely the one which passes the best-track matching. Higher orders (e.g. pile-up of three elastic scatterings) are neglected due to the very low probability. Further, pileup of elastic scattering with inelastic reactions occur which gives no bias, since no veto on inelastic events (e.g. by vetoing on activity on the inner ATLAS-Detectors) is placed. Any inelastic reaction fragments which reach ALFA-Detectors are filtered out as background.

To illustrate the spacial distribution of reconstructed tracks where an elastic trigger signal is present, figure 5.7 shows this distribution exemplary for detector A7L1U in run 309039. The elastic events are concentrated in the central narrow vertical band. Parallel-to-point focusing spans this band in the vertical plane. The geometric diamond like shape is visible as the envelope around all reconstructed events. Noticeable is that there is a clear wide side-band visible, extending to positive horizontal values. Tracks in this region stem mainly from any type of event, where protons loose energy either from collisions or by interaction with residual beam gas, causing them to travel at narrower orbits around the LHC center (located on the positive horizontal side). The shadow of the beam-screen is also clearly visible around 20mm away from the beam center in vertical direction as a sharp drop in the density of reconstructed tracks. At very small y-values below the detector edge some few fake tracks were reconstructed.
Figure 5.8 shows the remaining elastic candidates after all selection cuts.

	run 308979	run 308982	run 309010	run 309039	run 309074	run 309165	run 309166
L1 Trigger Signal	494076 590377	159618 115603	731465 828363	1996561 1884135	680474 653332	856591 840149	709109 727543
Events with reconstructed tracks in all 4 detectors	230406 227552	75180 74003	452157 451224	1290913 1270948	477096 470027	616524 607263	558822 551456
Remaining after fiducial cut	228034 224249	74410 73227	448330 445961	1279103 1258248	472989 465601	611195 601302	554167 546105
Remaining after horizontal left-right cut	221148 216801	72196 71181	436532 433428	1244402 1224526	459715 452272	595431 585597	539725 531507
Remaining after vertical left-right cut	220389 215997	71928 70918	434972 431772	1240084 1220481	458164 450783	593272 583532	537851 529713
Remaining after horizontal position angle cut	220149 215713	71850 70828	434643 431402	1238907 1219376	457537 450149	592814 583082	537368 529170
Remaining after vertical position angle cut	217048 212827	70848 69934	428657 425798	1221794 1204038	451237 444516	584698 575475	529963 522463

TABLE 5.4: Run-by-run summary of the cutflow of elastic event candidates in the golden topologies after successive cut application. The first number in each cell gives the number of remaining elastic event candidates in spectrometer arm 1 (see 5.5), where the second number gives the according number of elastic candidates for elastic arm 2 (see 5.6).

Run number	Pileup Events	Pileup-fraction
308979	66	0.000153533
308982	23	0.000163373
309010	195	0.000228216
309039	478	0.000197046
309074	145	0.000161875
309165	448	0.000386149
309166	354	0.000336366

TABLE 5.5: Run-by-run summary of the cutflow of the golden event pileup-fraction

Everything outside the central band is indirectly cut away by the correlation cuts, except for the events above the beam-screen and near the detector edge, where the cut is directly applied on the vertical spacial coordinate of the respective tracks.

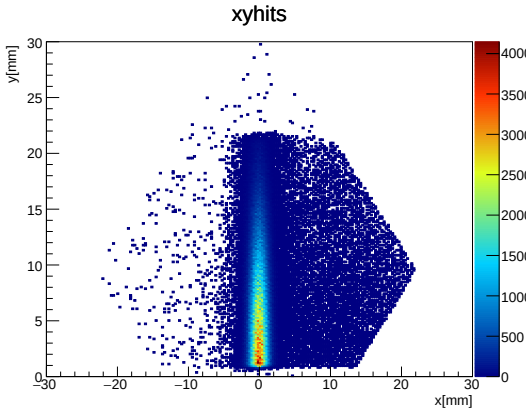

FIGURE 5.7: Spacial distribution (hitmap) of reconstructed tracks from golden events fulfilling the elastic trigger condition but with no additional event selection cuts. This sample is for detector A7L1U in run 309039. Notice the diamond shape envelope around the hits which resembles the physical detector geometry.

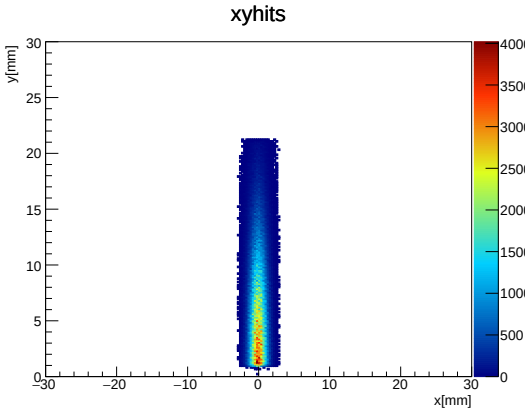

FIGURE 5.8: Spacial distribution (hitmap) of reconstructed tracks from golden events fulfilling the elastic trigger condition after all applied event selection cuts. This sample is for detector A7L1U in run 309039.

Figures 5.9 and 5.10 show the horizontal and vertical projections of the distributions shown in figures 5.7 and 5.8 respectively. The plots are again exemplary for detector A7L1U. The blue lines show the distributions of the raw event selection for the golden topology, so events which just fulfill the elastic trigger conditions and tracks are present in all four spectrometer arm detectors

and no further selection cuts, whereas the red lines show the distributions after elastic selection cuts. The horizontal distribution for the trigger-only selection in 5.7 shows the peak of the elastic candidates in the central region, a tail at positive values for the mainly diffractive protons and some other background to the negative side. Those side bands vanish after selection cuts are applied (red line), leaving only the fairly Gaussian shaped elastic core. Logarithmic scale was chosen in figure 5.9 to make the tail regions more easily visible. No distinctive features can be seen by eye in figure 5.10 by comparing the vertical track positions before and after elastic selection cuts. A small amount of elastic candidates near the detector edge (visible at the first bin) is completely cut away by the edge cut.

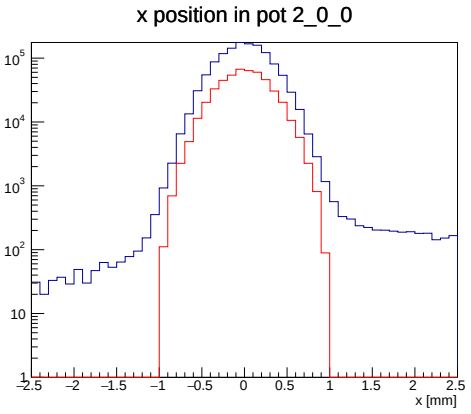

FIGURE 5.9: Horizontal spacial distribution of reconstructed golden events fulfilling the elastic trigger condition. The blue curve shows the reconstructed events without any applied event selection cuts, while the red curve shows the resulting distribution after event selection cuts. This sample is for detector A7L1U in run 309039.

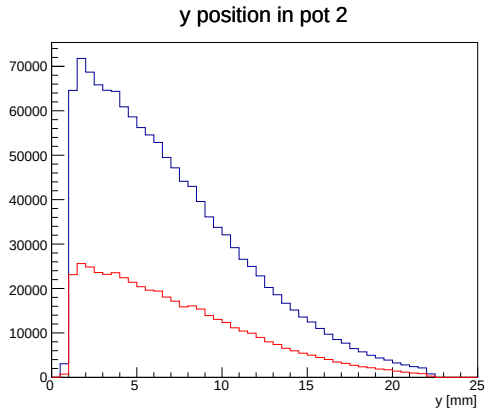

FIGURE 5.10: Vertical spacial distribution of reconstructed golden events fulfilling the elastic trigger condition. The blue curve shows the reconstructed events without any applied event selection cuts, while the red curve shows the resulting distribution after event selection cuts. This sample is for detector A7L1U in run 309039.

A noteworthy characteristic of elastic tracks is shown in figures 5.11 and 5.12. The plots show how many tracks are reconstructed in total given a certain number of lit up fibers in the detector for this event. This observable is not specific to tracks with elastic origin, but characteristic of the detector response to a passing proton (perpendicular to the detector surface) and of the coinciding beam background.

We have in blue the distribution for any tracks given elastic trigger conditions, while in red we have the resulting distribution after all applied elastic correlation cuts. The left hand figure 5.11 shows the total fiber multiplicity distribution of the outer detector B7L1U, while the right hand figure 5.12 shows the distribution for the inner detector A7L1U. We see on all distributions a most probable value of around 22, which means that most single protons cause around 22 fibers to light up in the detector. We have a local maximum around the double value of this, caused by two coinciding protons (not visible in this double logarithmic scale). The most noteworthy feature seen in those distributions is that for the outer detectors (as illustrated by 5.11) the distribution is broader and also after elastic correlation cuts there remains a high multiplicity tail in the sample. Both is explained by the fact that on some cases the protons coming from the interaction point cause a shower on their way trough the inner detector, which spreads together with the incident proton outwards, resulting in a higher total fiber multiplicity. In most cases however when such a shower develops, track reconstruction becomes impossible in the outer detector, resulting in a failure in reconstruction. Those cases will be examined in detail in the reconstruction efficiency section. A proton that passes through the detector perpendicularly to its surface passes through ten fibers in each of the two fiber planes, naively expecting a total fiber multiplicity of 20. However the number of lit up fibers is increased by cross-talk, electronic noise, background coincidences and interactions of the proton with the detector. A single fiber efficiency of about 93 per cent [32], mainly because of insensitive coating material surrounding a fiber, decreases the total number of lit fibers, giving a net effect of slightly more than 20 lit up fibers as the expected total fiber multiplicity.

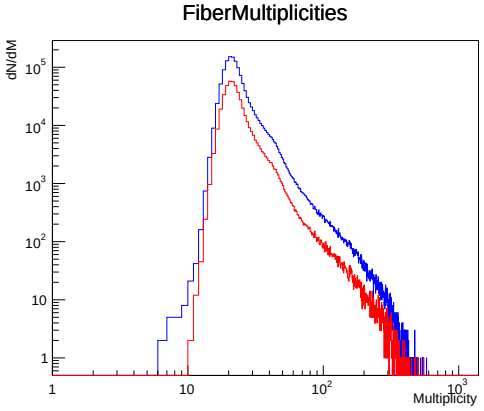

FIGURE 5.11: Total fiber multiplicity distribution for the outer detector B7L1U. The blue curve shows the reconstructed events without any applied event selection cuts, while the red curve shows the resulting distribution after event selection cuts. This sample is for run 309039.

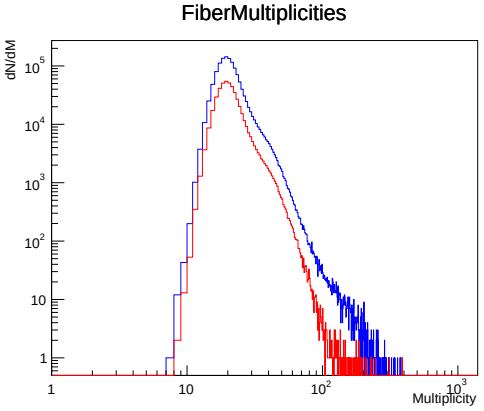

FIGURE 5.12: Total fiber multiplicity distribution for the inner detector A7L1U. The blue curve shows the reconstructed events without any applied event selection cuts, while the red curve shows the resulting distribution after event selection cuts. This sample is for run 309039.

5.2 Background estimation

In this chapter, we shall discuss how to deal with the presence of irreducible background count remaining in the final elastic event count numbers. Basically, we have to apply a suitable method which can give an estimate of how much residual background events we can expect in the final sample, which number can then be subtracted to give the final elastic event count.

Three methods of estimating residual background amount are established in our analysis procedure. The so called "Vertex method" as well as the "Antigolden method" were established and used concurrently for the 7 TeV dataset [28], whereas only the "Antigolden method" was used in the 8 TeV, $\beta^* = 90\,\mathrm{m}$ dataset [33]. In light of significant different background conditions and levels, during the analysis of the 1km and this dataset, a new method of background determination was developed and tested, called the "Event mixing method". These three methods are, on their own, purely data driven. This is due to the fact, that the background from beam halo protons cannot be predicted and simulated reliably.

The "event mixing method" was extended to include background count estimates from "Double Pomeron Exchange" (DPE). The shape of the background contribution is obtained from Monte-Carlo, while the normalization is data driven. The analysis of DPE background was already included in the analysis of the 8 TeV, $\beta^* = 1\,\text{km}$ dataset [34], which is however, at the time this thesis was written, not published yet.

5.2.1 Vertex position method

The vertex position method estimates the number of residual background events by analyzing the horizontal vertex distribution of the sample. The vertex position of any track is the exact position at the interaction point, from which the incident proton originates. This makes the term "interaction point" a bit misleading, since beam collisions do not take place in a single point at this IP, but within a narrow region due to a non-negligible beam width in the horizontal and vertical plane and beam-bunch length in the z-direction. A vertex position of any given event is extrapolated from the track positions in the ALFA detectors using the first row of the inversion of the transport matrix:

$$x^* = M_{11}^{-1} \cdot x + M_{21}^{-1} \cdot \theta_x \tag{5.5}$$

To estimate the residual background fraction in this sample, the observation is exploited that tracks with elastic origin have a fairly Gaussian shaped distribution around the beam center whereas background tracks have a broader non-Gaussian distribution. A template of background events has to be generated from the data. The Gaussian elastic template and the background template are both fitted to the vertex distribution with floating normalization to get an estimate of the residual background fraction in the vertex distribution. Only the vertex distribution in the horizontal plane is examined, since it is not possible to get an adequate vertex distribution in the vertical plane. In the vertical plane, the beam optics is set to parallel-to-point focusing, meaning that the track position in the detectors is

independent of the origin vertex position but largely dependence on the angle under which this given protons leaves the interaction point. Hence it is in reverse not possible to extrapolate from any given vertical track position in the detector backwards to a position in the interaction point.
This method was co-used in the 7TeV analysis but was later dropped due to poor fit stabilities and is not used in this analysis.

5.2.2 Antigolden method

In the antigolden method background templates are constructed directly in the detector coordinate system. It can be used, if most of the background is composed of random coincidences of background tracks on A-side and C-side. In this method, events are selected where all four detectors either on the positive side of the vertical plane have reconstructed tracks (called "arm++", see figure 5.13), or all four detectors on the negative vertical plane have tracks (called "arm−−", see figure 5.15).

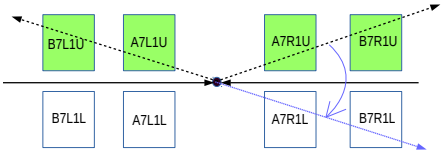

FIGURE 5.13: Schematic illustration of the construction of a pseudo-elastic background template event using a coincidence in arm++, flipping the sign on the coordinate on the vertical plane of the track coordinates on the tracks on C-side. The resulting event mimics a coincidence in spectrometer arm 1

From each of those samples ("arm++" and "arm−−") events from either one side from the interaction point ("A-Side", "C-Side") can be projected on the opposite detectors in the vertical plane simply by flipping the sign on the reconstructed track coordinates giving background templates in both elastic spectrometer arms 1 and 2. The weakness of this method is that we need

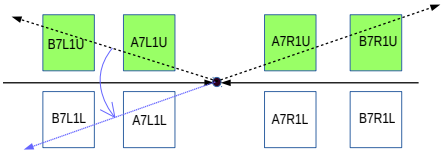

FIGURE 5.14: Schematic illustration of the construction of a pseudo-elastic background template event using a coincidence in arm++, flipping the sign on the coordinate on the vertical plane of the track coordinates on the tracks on A-side. The resulting event mimics a coincidence in spectrometer arm 2

to assume symmetric background conditions in the vertical plane and also we require the detectors to have equal distance to the beam, otherwise the critical background conditions near the detector edge cannot be modeled. The event selection requires trigger activity on the two armlets that are selected for. In nominal analysis mode, "soft trigger conditions" are required, meaning that the trigger tile of either one of the involved triggers in an armlet has to have fired. A trigger veto is set on the vertically opposite detectors, to prevent the selection for real elastic events, coinciding with background on one vertical plane.

5.2.3 Event mixing method

The Event mixing method was invented in light of the 1 km data analysis to address shortcomings from the conventional antigolden and vertex method. The estimation of the irreducible background content in the elastic sample is based upon building background templates and scaling them appropriately so that the event count in the background templates inside the elastic event selection criteria gives an estimate of the background count in the elastic sample. The procedure relies on background that is caused by random coincidences of background happening on the A-side and on the C-side simultaneously. This background can contain mixed contributions between single diffractive events and beam halo particles or between two of the same kind. For single diffractive processes there exist simulations which could be used for background estimation, however no procedure exists which simulates the beam halo background. In the LHC there are circulating non-colliding bunches which can in principle be used to study halo effects, however they are unsuitable to construct halo templates due to their different beam bunch shapes. The background

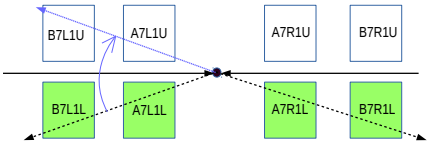

FIGURE 5.15: Schematic illustration of the construction of a pseudo-elastic background template event using a coincidence in arm−−, flipping the sign on the coordinate on the vertical plane of the track coordinates on the tracks on A-side. The resulting event mimics a coincidence in spectrometer arm 1

template construction in the event mixing method is performed in the following consecutive steps:

1. A sample of tracks is collected for all four armlets independently. For any given armlet, there is a veto on activity on the opposite armlet on the other side from the interaction point, to ensure that pure background is selected and no elastic tracks.

2. Tracks are randomly combined from each of the two elastic spectrometer arms to form random A-side/C-side background combinations.

3. After combination, there exists an background event sample (template) for which correlation plots as for the elastic event selection are constructed.

4. The background templates need to be scaled in order to quantitatively represent the background in the elastic sample.

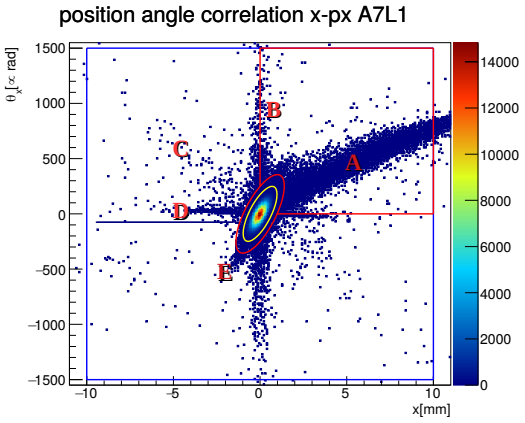

FIGURE 5.16: Local angle correlation for events in elastic spectrometer arm 1. This sample is for run 309039.

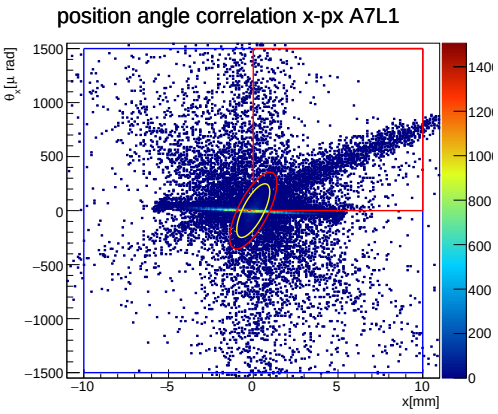

FIGURE 5.17: Local angle correlation for the background template in elastic spectrometer arm 1. This sample is for run 309039.

The scaling shall be explained by figures 5.16 and 5.17. Figure 5.16 shows again the position vs. local angle correlation in the horizontal plane of the elastic selection in spectrometer arm 1 whereas figure 5.17 shows the corresponding background template. In both figures, the central narrow yellow ellipse shows the elastic

selection criteria for this correlation as introduced before. For the background scaling procedure we introduce additional regions in this correlation plot. First, we assume that anything beyond a 5-sigma ellipse (red ellipse) can be safely considered to be background. Second we introduce outside the 5-sigma region two separate regions, so that we have two ways of scaling from this correlation. The region in the upper right hand quadrant, bordered inside red lines, we shall call "off-momentum region". The events in this quadrant are mainly comprised of single diffractive events which make up the curved "tail" that extends to large x-values. As we have introduced before, these are any kind of protons which have lost momentum in an interaction. The region also contains a small amount of halo protons from the uncorrelated band near $x = 0$, extending upwards to positive local angles. The second normalization region comprises the remaining three quadrants, bordered in blue. We shall call this region "off-orbit region" since it is mainly composed of beam halo protons which have escaped the nominal LHC beam orbit. In order to estimate the residual background contribution in the elastic sample 5.16 inside the yellow ellipse, which we are ultimately interested in, we scale the background template 5.17 e.g. in the "off-momentum region" by re-normalizing the event count, so that the number of entries inside the red borders matches between both correlations 5.16 and 5.17. From the rescaled version of the background template 5.17 one can now easily count the number of events inside the yellow ellipse of this correlation which is now the number of residual background we estimate for our elastic sample inside the yellow ellipse.

Figures 5.18 and 5.19 show the same for elastic spectrometer arm 2, where the uncorrelated halo bands are a bit more pronounced.

We see in figure 5.16 several distinctive background bands, the nature of which shall be shortly explained. The dense band labeled "A" in the "off-momentum" region consists mostly of events, where protons have lost energy. These are single diffractive processes and DPE. The nature of the band in "B" is not fully determined, however it seems to be a mixture of beam halo background (since it is also visible in the background template 5.17 and some elastic events which get reconstructed with too high angles in the horizontal plane, possibly due to missing

fiber hits lowering the resolution. The latter contribution would be in any case too small to cause significant deviations from the determined elastic event count. Region "C" are clearly halo background. Region "D" are halo or upstream shower background events, which are close to the detector edge in the vertical plane and have a relatively steep local angle in the vertical plane. Most of these are filtered out by the newly introduced cut on the vertical position and local angle. Region "E" seem to be DPE events, since this contribution can not be described by the event mixing template in 5.17 but is however clearly visible in the DPE template in 5.20.

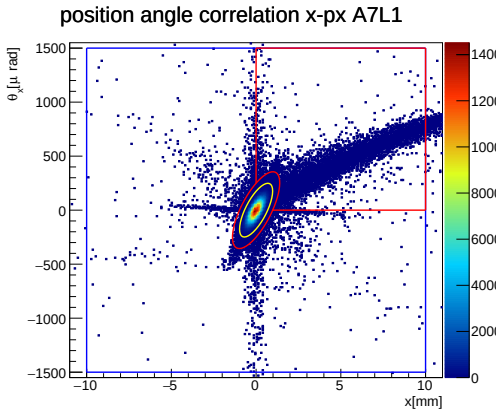

FIGURE 5.18: Local angle correlation for events in elastic spectrometer arm 2. This sample is for run 309039.

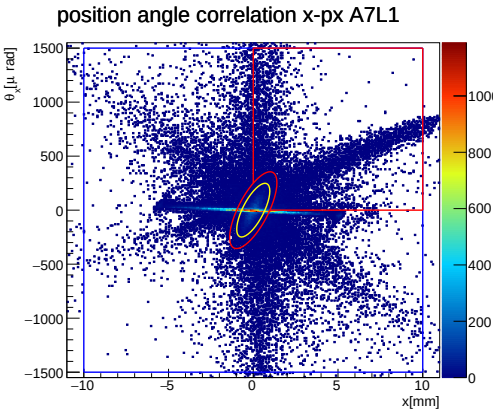

FIGURE 5.19: Local angle correlation for the background template in elastic spectrometer arm 2. This sample is for run 309039.

The event mixing algorithm was designed to handle the background estimation for an arbitrary time slicing setting. It was found, that in this run just as for the previous 1 km data set, background fraction builds up over time until a LHC beam scraping is performed. After the scraping, the rate of background pollution returns to a small initial value and begins to increase again. The halo envelope of the LHC beam quickly repopulates over time, while the background contributions from single diffractive events decreases according to the luminosity curve. The event mixing algorithm was set to do the time slicing and background subtraction in 10-Luminosity-Block intervals. This is a compromise between time resolution and gathering enough statistics within each block. The event mixing algorithm is also

designed to do the background subtraction independent for each colliding bunch, however a global background template was chosen for the nominal background value, since it turned out that the per-bunch approach had no impact on the result.

In the next chapter, the event mixing algorithm will play a crucial role in determining the background contributions in any given "failed topology", that is, where we assume to have an elastic event, where however only a subset out of the four detectors that make up a spectrometer arm have reconstructed tracks. We will see that the irreducible background contribution becomes significantly higher for other elastic topologies in contrast to the very small estimated background as shown in table 5.6.

5.2.4 DPE Contribution

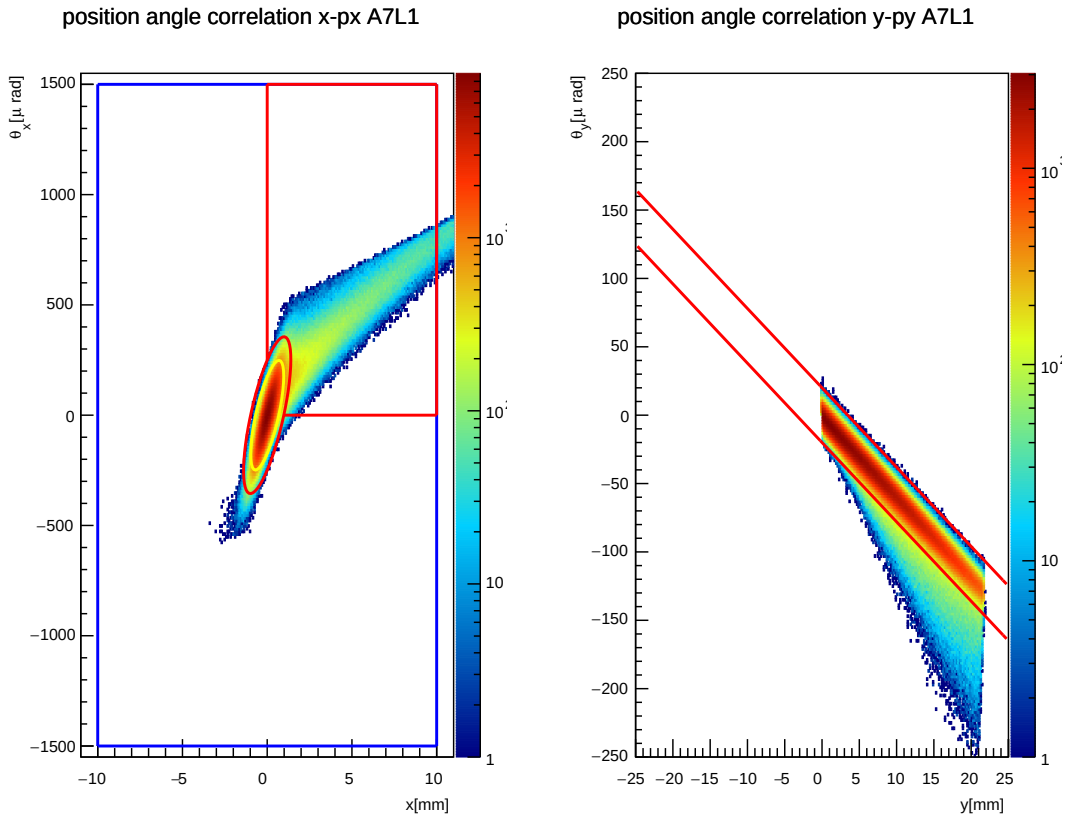

FIGURE 5.20: Position vs local angle correlations in the horizontal plane (left) and the vertical plane (right) of the Monte-Carlo generated DPE sample that was used as input for the background analysis. The yellow (left) and red (right) ellipse/lines indicate the corresponding elastic selection region. [35]

The event mixing method was extended to include DPE background contributions, which are not accessible through combination of uncorrelated tracks. Figure 5.20 shows the position vs. local angle correlations of the DPE sample that was obtained from Monte-Carlo. Most DPE events fall within the elastic event selection cuts and also have the elastic trigger topology. The DPE cross-section suffers from model-dependent uncertainties, hence it is determined data driven. For that, both the DPE sample as well as the event mixing sample are taken, each with a given unknown scaling factor s. The two scaling factors are calculated by finding the combination, such that the sum of both templates accurately reproduces the background count e.g. in figure 5.16 in both normalization regions (off-orbit and off-momentum) simultaneously. This is given by the solution of equations 5.6 and

5.7:

$$s_1 \cdot B_{\text{Eventmixing,Off-Momentum}} + s_2 \cdot B_{\text{DPE,Off-Momentum}} = B_{\text{Data,Off-Momentum}} \tag{5.6}$$

$$s_1 \cdot B_{\text{Eventmixing,Off-Orbit}} + s_2 \cdot B_{\text{DPE,Off-Orbit}} = B_{\text{Data,Off-Orbit}} \tag{5.7}$$

Here s_1 is the scaling factor of the event mixing based background template, s_2 is the scaling factor of the DPE background template. B are the event counts in off-orbit and off-moment regions of the event mixing and DPE template and in the elastic data sample respectively.

This procedure was chosen, because the horizontal position vs. angle correlation is available in all data driven event topologies and because this way, a combined background template is constructed. It can be seen in figure 5.16, that DPE is present in regions "A" and "E", which means that DPE is present in both off-momentum and off-orbit region for the position local angle correlation in the horizontal plane. The method described above takes this nicely into account.
For the background contribution of the "failed topologies" (see next section), the DPE background count is fixed by the amount of DPE in the golden topologies and the ratio of the elastic event numbers golden/failed.

5.3 Reconstruction efficiency

The precise determination of the reconstruction efficiency is important as it defines the normalization to transform the counting spectrum into the differential elastic cross-section. The central part of this work is the determination of the reconstruction efficiency of both elastic spectrometer arms, which is the probability that a given physical elastic scattering process, happening within the acceptance region of ALFA, is fully reconstructed in terms of proton tracks by all four ALFA detectors involved. Failure in track reconstruction in one or more detectors is

caused by any type of event, which overwhelms the track reconstruction algorithm due to given high lit up fibers for a given event. Main reasons for such a situation are

- Hadronic shower development at the ALFA stations caused by a passing proton
- Hadronic shower development upstream (e.g. at a beam collimator or pile-up inelastic process at the interaction point or interactions with beam gas)
- Pile-up with other diffractive processes
- Pile-up with beam halo protons
- Electronic noise
- Fiber cross-talk
- Any combinations of the above

The determination of the reconstruction efficiency for the $\beta^* = 2.5\,\mathrm{km}$ campaign is, just as in previous analysis, a mainly data-driven approach. Monte-Carlo-Simulation plays a role in the relative acceptance correction ("phase space corrections", or "EOFs" (Elastic overestimation factor) that were introduced as part of this work and already implemented in the $\sqrt{s} = 8\,\mathrm{TeV}$, $\beta^* = 90\,\mathrm{m}$ analysis. In the previous analysis these corrections were however determined data driven. Also in this analysis, the DPE part of the background pollution is estimated with the aid of a Monte-Carlo-Simulation.

5.3.1 Definition

The basic definition of the reconstruction efficiency is given by equation 5.8, which is the number of fully reconstructed events (denoted as N_{golden}) over the total

number of elastic events with only tracks reconstructed in a subset of detectors, denoted as N_{fail}.

$$\epsilon_{\text{reco}} = \frac{N_{\text{golden}}}{N_{\text{golden}} + N_{\text{fail}}} \tag{5.8}$$

The numbers N_{golden} for both spectrometer arms were already determined in the previous chapter. In order to determine the numbers N_{fail}, we expand formula 5.8 to obtain:

$$\epsilon_{\text{reco}} = \frac{N_{\text{golden}}}{N_{\text{golden}} + N_{3/4\text{i}} + N_{3/4\text{o}} + N_{2/4} + N_{\text{lower}}} \tag{5.9}$$

For equation 5.9, we introduce "failed topologies", meaning constellations of subsets of detectors which have reconstructed tracks that were of elastic origin. The definition of these topologies and the determination of the according elastic event numbers shall be explained further below in the according subsections.
From each of these event counts, we need to subtract the irreducible background estimation B_i we obtain for those samples, as indicated by equation 5.10. Elastic event- and residual background estimation becomes increasingly difficult, the fewer detectors are available with reconstructed tracks due to decreasing number of correlation cuts that can be applied.
Last, we modify our reconstruction efficiency definition to correct the obtained background corrected elastic event numbers for an acceptance effect. The event acceptance slightly increases, when correlation cuts become unavailable in a given failed topology, hence a topology specific phase space correction was introduced. We shall call this "Elastic Overestimation Factor" or short "EOF". Contrary to previous $\sqrt{s} = 8\,\text{TeV}$ analysis, the EOFs are calculated by MonteCarlo to exclude uncertainties from background pollution. The procedure for determining the EOFs is outlined here:

1. Take a Monte-Carlo sample of golden elastic events with all four detectors of the spectrometer arm with reconstructed tracks

2. Apply all golden correlation cuts as introduced in the previous chapter and save the event count

3. Apply now to the same sample only the correlation cuts available for a given failed topology and again safe the event count. More events will pass the reduced set of selection cuts.

4. The ratio from the above two numbers now gives a correction factor (EOF), which can be interpreted as the acceptance ratio between a golden and a given failed topology

5. Divide the background corrected event numbers for the failed topologies with the according EOF to obtain an event count which is in accordance to the same phase space as the golden sample

We now write our definition for the reconstruction efficiency as follows:

$$\epsilon_{\text{reco}} = \frac{(N_{\text{golden}} - B_{\text{golden}})}{(N_{\text{golden}} - B_{\text{golden}}) + \frac{(N_{3/4\text{i}} - B_{3/4\text{i}})}{\text{EOF}(3/4\text{i})} + \frac{(N_{3/4\text{o}} - B_{3/4\text{o}})}{\text{EOF}(3/4\text{o})} + \frac{(N_{2/4} - B_{2/4})}{\text{EOF}(2/4)} + N_{\text{lower}}} \tag{5.10}$$

The determination of the numbers in equation 5.10 will be explained in the following subsections.

5.3.2 Workflow

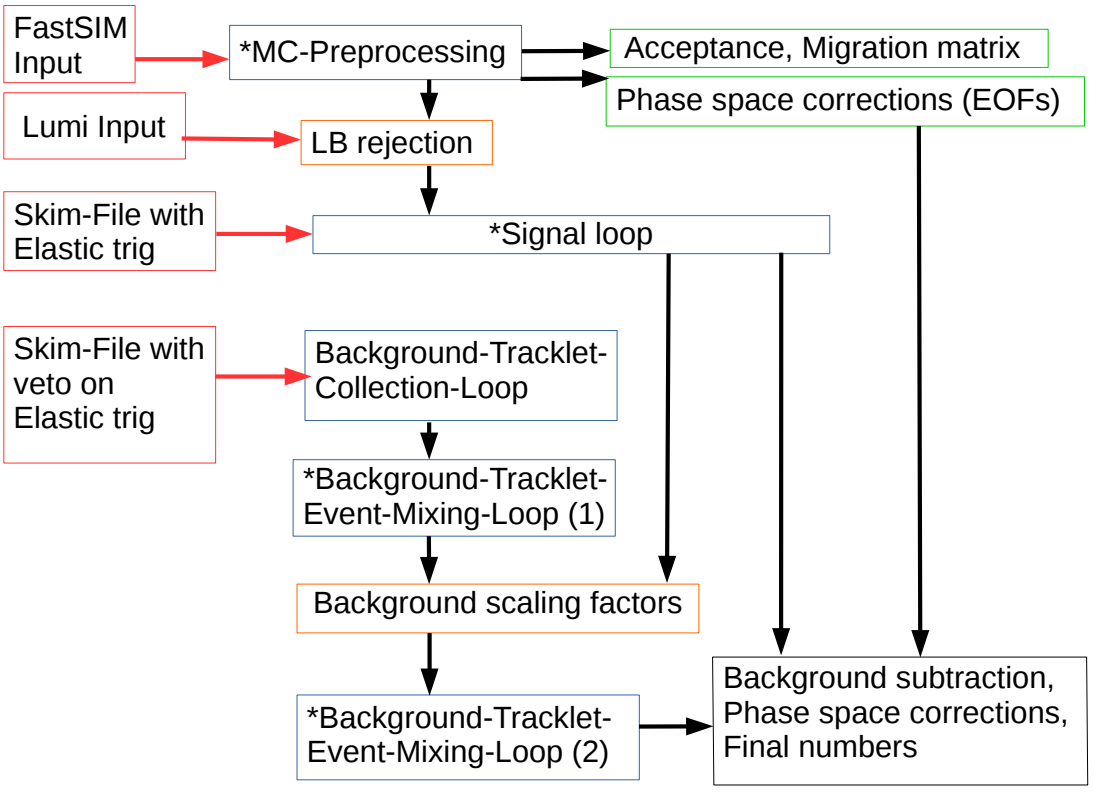

FIGURE 5.21: Logic of the reconstruction efficiency algorithm with included background subtraction by event mixing

Figure 5.21 shows the basic workflow of the reconstruction efficiency algorithm. The algorithm relies on four input files (red boxes):

1. A file containing a Monte-Carlo sample of elastic events with position and momentum distributions at the interaction point.

2. A file containing for each Luminosity Block the duration, the dead time and delivered luminosity

3. A ROOT-NTuple file, containing a pre-selection (skim) of events where an elastic trigger signal is present

4. A ROOT-NTuples file without any elastic trigger signals, however trigger signals from individual detectors

The simulated elastic protons from the first input file are propagated to the detector stations using the beam transport matrix elements obtained from the effective beam optics. The obtained proton positions are Gaussian smeared in order to mimic the finite detector track reconstruction position resolution. Obtained from those are the t-dependence of the acceptance, the migration matrix (comparison of real t-values of the events to reconstructed t-values) and most importantly for this work, the phase space corrections (EOFs).

The luminosity input file provides information about which luminosity blocks shall be rejected for further analysis due to limited duration or high data taking dead time fraction (data quality cuts).

The input file containing events with elastic trigger signals present provide a pool from which elastic event candidates are selected for each given golden and failed topology (denoted as "SignalLoop").

The input file containing events without elastic trigger signal provide a pool, from which background event templates are constructed. In the first stage, "tracklets" are collected and stored at runtime in RAM, which are background tracks at either side from the interaction point, present at either a full armlet (neighboring detectors), or present at any one of the two detectors of an armlet. The latter ones are later used to construct background templates for the "failed topologies". In the next analysis steps ("Background-Tracklet-Event-Mixing-Loop (1)") the previously collected background tracklets are randomly combined with tracklets from the opposite side from the interaction point to form events for the background templates. After this, by comparing the background correlation templates with the according correlations from the elastic samples, the background template scaling factors are derived. Those scaling factors are then used for a second iteration of the tracklet combination stage ("Background-Tracklet-Event-Mixing-Loop (2)"). This loop constructs all background histograms again, however with the correct scaling.

Using the background t-spectra, the t-spectra of the elastic candidates and the EOFs, the value of the reconstruction efficiency per spectrometer arm is then calculated using formula 5.10.

5.3.3 Event selection

Event selection for the failed topologies is similar compared to event selection for the golden topologies. For an elastic spectrometer arm, we require the elastic trigger signal, L1_ALFA_ELAST15 or L1_ALFA_ELAST18 respectively being present for this event. It is then checked, which ones out of the four detectors provide reconstructed tracks. We categorize events into failed topologies depending on which detectors provide no reconstructed tracks. The tracks are then checked for elastic back-to-back characteristics with as many selection cuts as are available in these cases. For instance if an event has one outer detector in C-side with no reconstructed tracks, one set of left-right-coplanarity cuts is unavailable, as well as the position local angle correlation on C-side. The lack of available event selection cuts leads to an increase in acceptance in those failed topologies. To compensate for this effect, phase space corrections were introduced and applied to the background subtracted event number in those failed topologies as described before.
We can attribute the cause of a failed topology by two event classes:

1. The tracking algorithm becomes unable to find individual tracks, due to e.g. shower developments, multiple pile-up events, too high cross-talks/noise, etc.

2. A proton just "grazes" the detector(s), giving elastic trigger signal but not enough fiber hits to reconstruct a track there

The first one causes the reconstruction inefficiency, whereas the second one is caused by an event that happened outside of the detectors geometric acceptance. This type of event is handled by the acceptance correction and must not be counted again in the reconstruction efficiency analysis. In order to ensure, that a reconstruction failure is caused by too many instead of too few fiber hits, a minimum of at least five fiber hits is requested for those detectors, otherwise the event will be considered to be out of the acceptance and hence discarded.

In the following section we will see the results from the event selection in the failed topologies.

5.3.4 Data driven event topologies

We divide the failed topologies into two main categories. The first one are the "data driven event topologies" where event selection is done in data. Those topologies constitute any case of failed detectors, where there is still one position vs. local angle (x vs. θ_x) cut available. The second category are the remaining cases, for which their respective event numbers will be estimated statistically.

5.3.4.1 Event topology 3/4i

We begin with our most common failed topology. The "3/4i" case, given the nomenclature, is composed of any events where three out of four detectors provide reconstructed tracks. "i" means, that all inner detectors have reconstructed tracks. This gives four sub-cases for this topology as illustrated in figure 5.22.

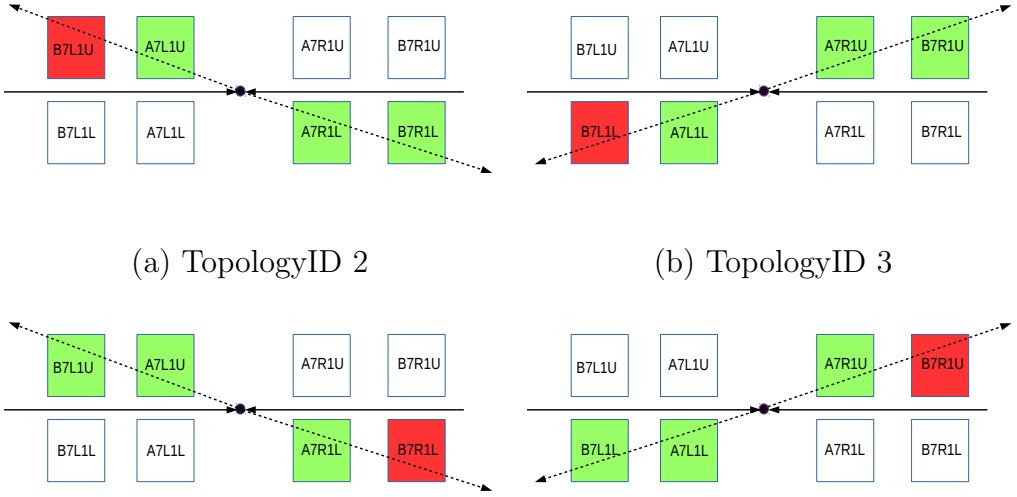

(a) TopologyID 2 (b) TopologyID 3

(c) TopologyID 4 (d) TopologyID 5

FIGURE 5.22: The sub-cases for the event topology class 3/4i. Elastic scattering is indicated by arrows. Detectors drawn in green indicate reconstructed tracks, while detectors drawn red indicate trigger signal in this armlet but no reconstructed tracks. Activity in the opposite spectrometer arm (white detectors) is ignored by default.

Each sub-case is treated individually and was given an ID number for easy array-handling in the program code. We shall use the ID number of the failed topologies for all event tables that follow below.

The cause of "3/4i"-events in most cases is, that on the side with the reconstruction failure, a shower developed at the inner detector. The shower spreads to the outer detector, lighting up too many fibers there for the reconstruction algorithm to handle.

In figure 5.23 we see the resulting t-spectra from the "3/4i"-event category. The blue line shows the according golden "4/4" sample as determined earlier for comparison. The t-spectra do not have at this point any unfolding or acceptance correction - they are just event counting spectra. We can already see, that the "3/4i"-events make up a sizable fraction of the overall elastic events. For all event samples, the irreducible background contribution is being estimated using the event mixing method. This gives us background corrected t-spectra, which are not be plotted here, which allows through integration to obtain the total number of events in this topology after division by the t-dependent EOFs (phase space

correction). We see, that the prevalence of background for the "3/4i" sample becomes larger near the detector edge at small t-values. This trend gets even more pronounced for the "2/4" topologies.

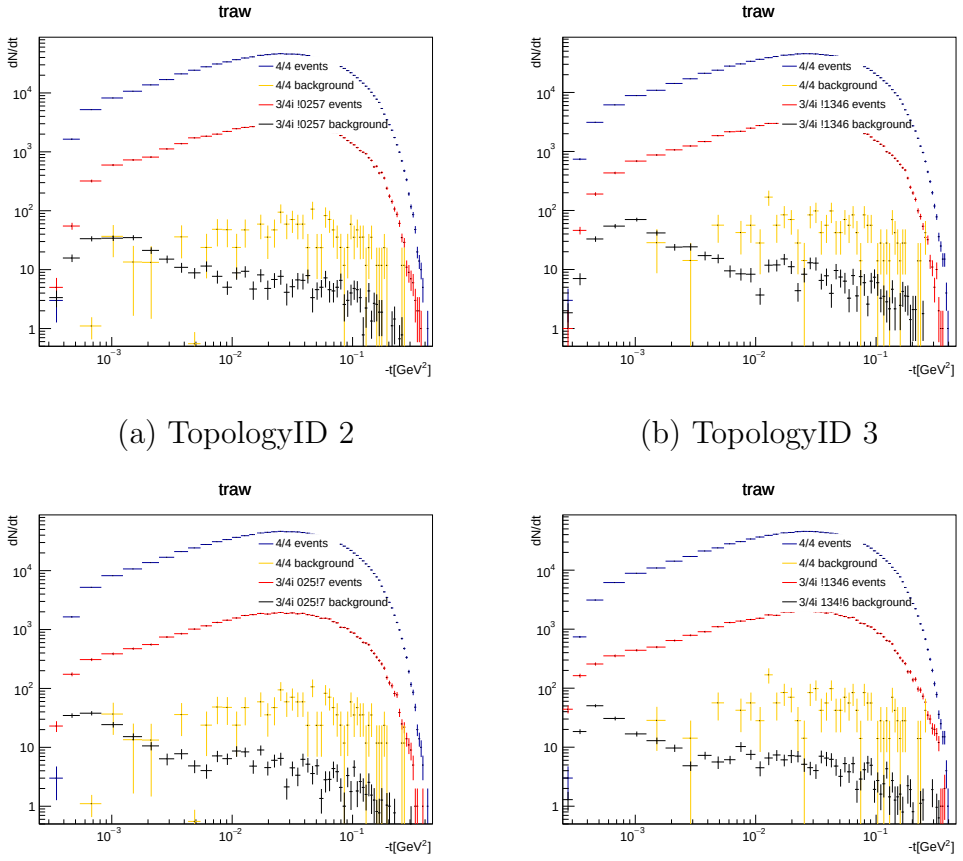

(a) TopologyID 2

(b) TopologyID 3

(c) TopologyID 4

(d) TopologyID 5

FIGURE 5.23: t-spectra reconstructed for the four sub-classes in the event topology class 3/4i in comparison with the according golden t-distribution. The blue line shows the reconstructed golden t-spectrum for comparison, while the red line shows the t-spectrum of the according failed topology. Yellow shows the residual background contribution estimated in the golden event sample, while black shows the residual background in the according failed t-spectrum both using the event mixing method.

Another important aspect for this analysis, as it was in the past, is to determine whether the reconstruction efficiency is independent of t. One might expect, that it is possible that the reconstruction efficiency drops at small t-values possibly due to increased likelihood of coinciding halo protons near the detector edge which faces the beam. To determine the behavior of the reconstruction efficiency is particular crucial for this analysis since it would have impact on the form of the CNI-region

in the final differential elastic cross section.

In order to confirm the t-independence of the reconstruction efficiency, we divide the background corrected and phase space corrected t-distributions of the according golden and failed distribution and see if the ratio between the events bin by bin remains constant.

We check for any t-dependence in the partial "3/4i"-reconstruction efficiency by plotting figure 5.24:

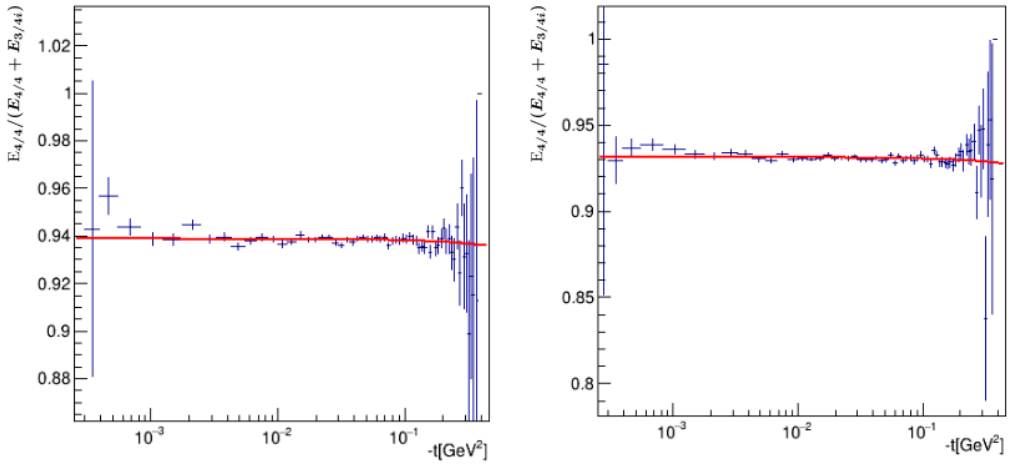

(a) TopologyID 2 (b) TopologyID 3

(c) TopologyID 4 (d) TopologyID 5

FIGURE 5.24: Ratios of the background and phase space corrected partial reconstruction efficiency for the "3/4i"-event class with given event counts E_i, where index i indicates the 4/4 and failed topology respectively.

We see, that for our "3/4i"-class events here, the partial reconstruction efficiency is flat in t within the uncertainties of a linear fit.

5.3.4.2 Event topology 3/4o

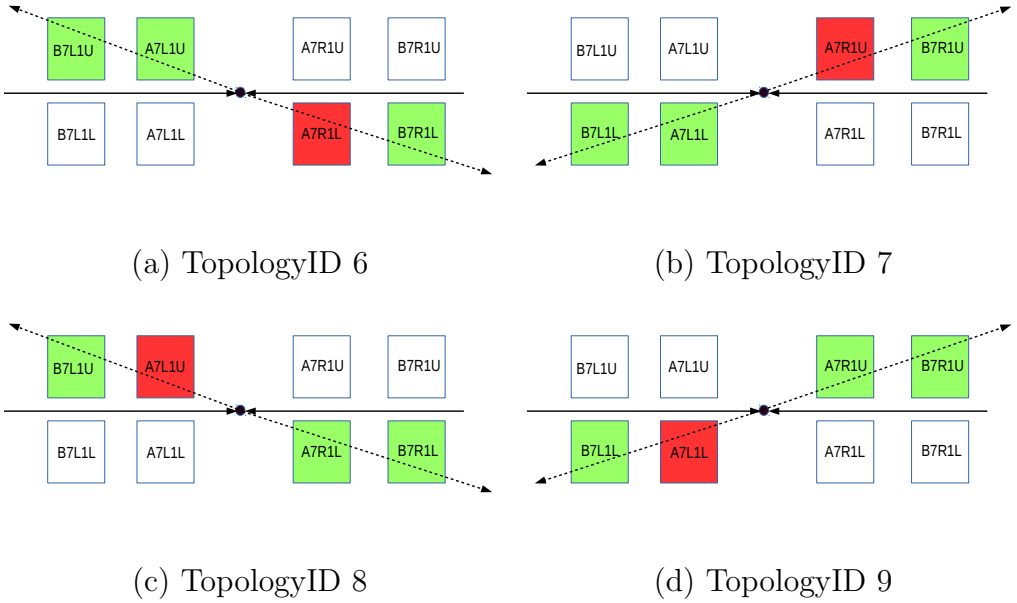

(a) TopologyID 6

(b) TopologyID 7

(c) TopologyID 8

(d) TopologyID 9

FIGURE 5.25: The sub-cases for the event topology class 3/4o. Elastic scattering is indicated by arrows. Detectors drawn in green indicate reconstructed tracks, while detectors drawn red indicate trigger signal in this armlet but no reconstructed tracks. Activity in the opposite spectrometer arm (white detectors) is ignored by default.

A rather peculiar class of events are the "3/4o"-class events, sketched in figure 5.25. Here, contrary to the "3/4i"-class, an inner detector has failed to provide reconstructed tracks. The probability for such an event is small compared to the other failed topologies. A possible cause for such an event is the development of a shower before the inner detector, overwhelming its track reconstruction. The density of the shower particles may decrease enough on the way to the outer detector to again allow track reconstruction.

As seen in figure 5.26, this sample consists of only a small amount of events.

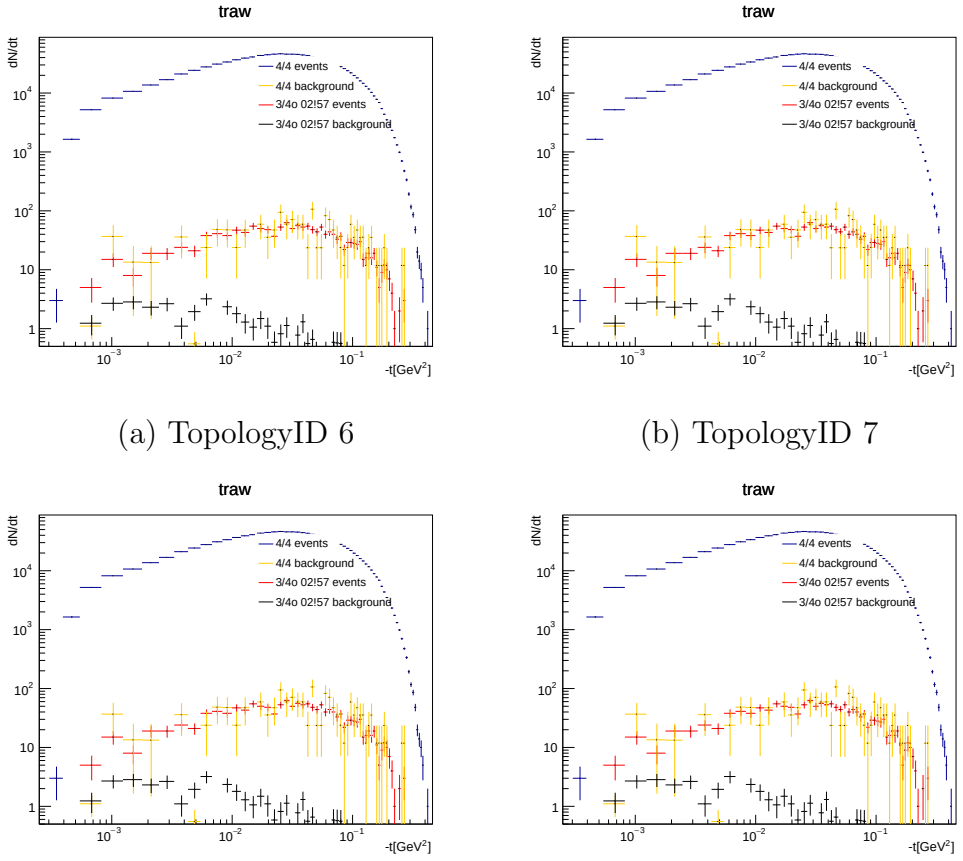

(a) TopologyID 6

(b) TopologyID 7

(c) TopologyID 8

(d) TopologyID 9

FIGURE 5.26: t-distributions reconstructed for the four sub-classes in the event topology class 3/4o in comparison with the according golden t-distribution. The blue line shows the reconstructed golden t-spectrum for comparison, while the red line shows the t-spectrum of the according failed topology. Yellow shows the residual background contribution estimated in the golden event sample, while black shows the residual background in the according failed t-spectrum both using the event mixing method.

The form of the t-distributions of those events are however in very good agreement with the golden elastic sample, given the ratio plots in figure 5.27. The large error-bars, especially in higher t-bins come from the fact, that the "3/4o"samples have small statistics.

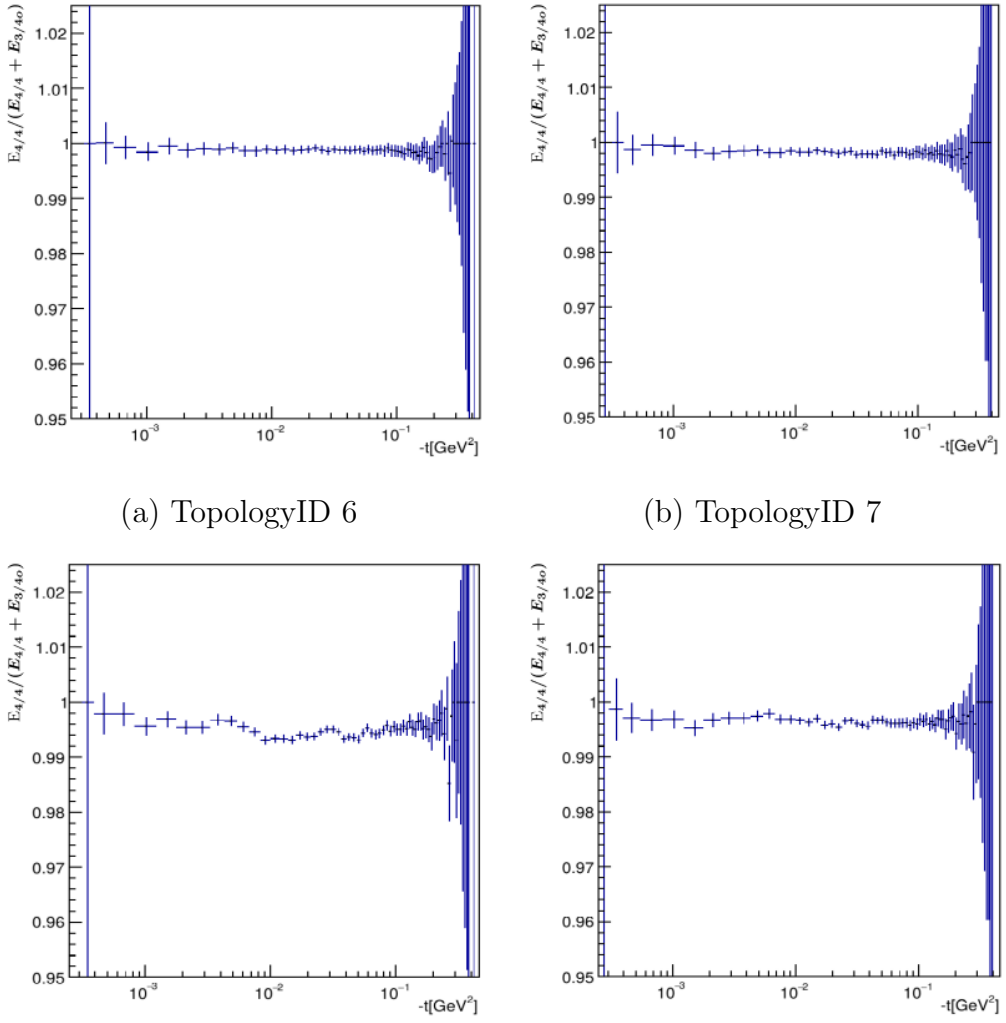

(a) TopologyID 6

(b) TopologyID 7

(c) TopologyID 8

(d) TopologyID 9

FIGURE 5.27: Ratios of the background and phase space corrected partial reconstruction efficiency for the "3/4o"-event class with given event counts E_i, where index i indicates the 4/4 and failed topology respectively.

5.3.4.3 Event topology 2/4

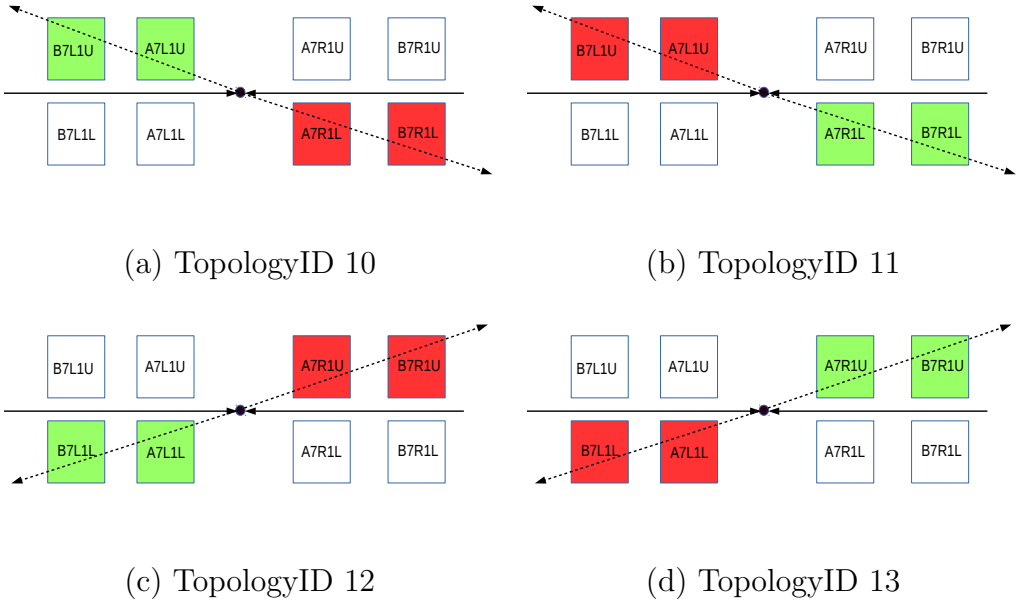

(a) TopologyID 10

(b) TopologyID 11

(c) TopologyID 12

(d) TopologyID 13

FIGURE 5.28: The sub-cases for the event topology class 2/4. Elastic scattering is indicated by arrows. Detectors drawn in green indicate reconstructed tracks, while detectors drawn red indicate trigger signal in this armlet but no reconstructed tracks. Activity in the opposite spectrometer arm (white detectors) is ignored by default.

The elastic event selection in the "2/4"-event class is the most difficult in this analysis. As seen in the topology sketches in figure 5.28, in these topologies, tracking information on an entire side of the interaction point is missing. There are no left-right correlation cuts possible and only one position local angle correlation for background suppression in each plane. Single diffractive protons as well as beam halo protons are primary sources of background here due to their similar event constellation. The elastic trigger requirements however cuts away most single sided background.

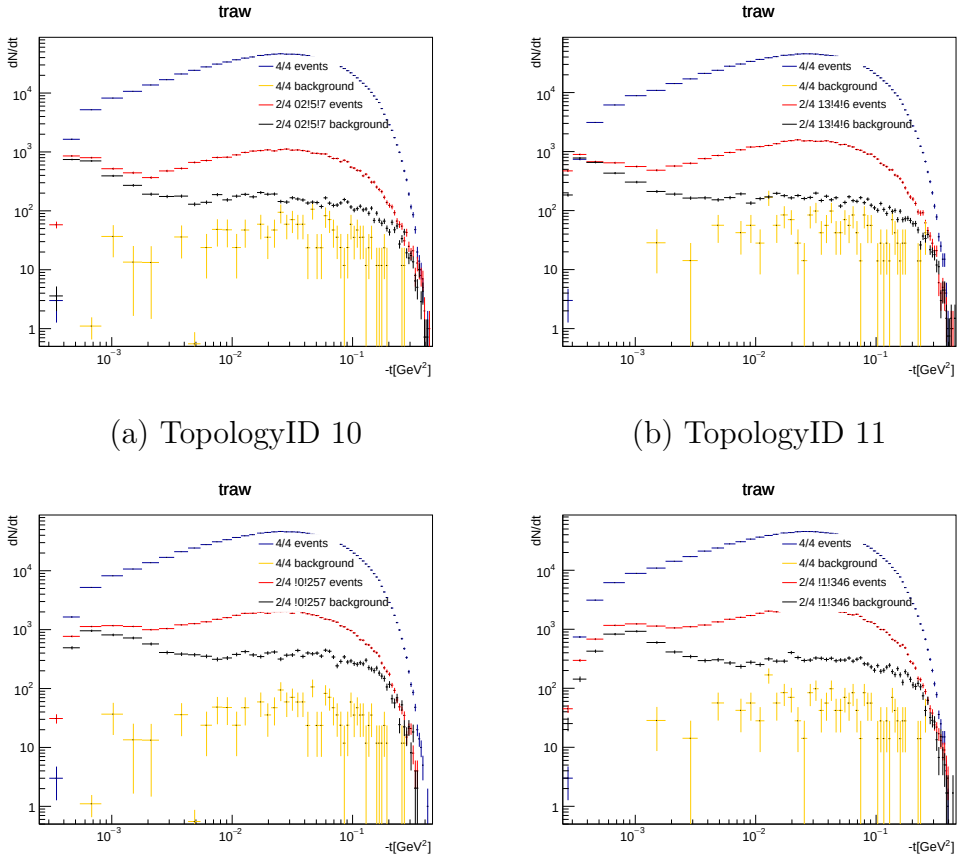

(a) TopologyID 10 (b) TopologyID 11

(c) TopologyID 12 (d) TopologyID 13

FIGURE 5.29: t-distributions reconstructed for the four sub-classes in the event topology class 2/4 in comparison with the according golden t-distribution. The blue line shows the reconstructed golden t-spectrum for comparison, while the red line shows the t-spectrum of the according failed topology. Yellow shows the residual background contribution estimated in the golden event sample, while black shows the residual background in the according failed t-spectrum both using the event mixing method.

The t-spectra for the "2/4"-event class as shown in figure 5.29 show in particular a large background contribution (black) for the samples (red). We see that the rate of "2/4" events becomes comparable to fully reconstructed elastic events for large t-values. For the few very first t-bins, the number of "2/4"-events after background subtraction and phase space correction is either overestimated or there is indeed a drop in reconstruction efficiency near the edge. Overall the fit line yields a negative slope in the order of one percent in t, indicating a slight overestimation of "2/4" events at large t. At the very first t-bins there are some fluctuations. Considering the large amount of background in these bins and the resulting uncertainties on the

elastic event numbers, these fluctuations are not enough to conclude any deviating reconstruction efficiency behavior at the lowest t-bins. Such a pattern would in any case be more apparent in the "3/4i" sample in figure 5.24, which gives also no hint to a t-dependent reconstruction efficiency.

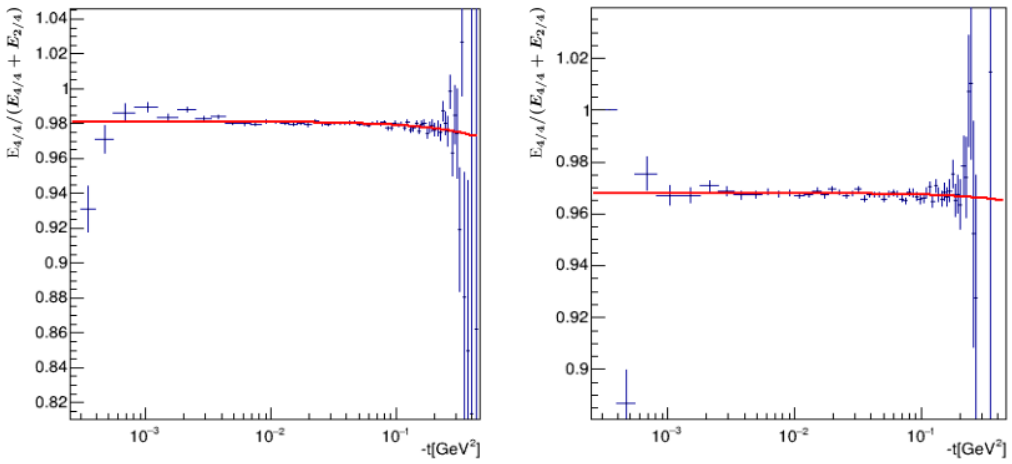

(a) TopologyID 10 (b) TopologyID 11

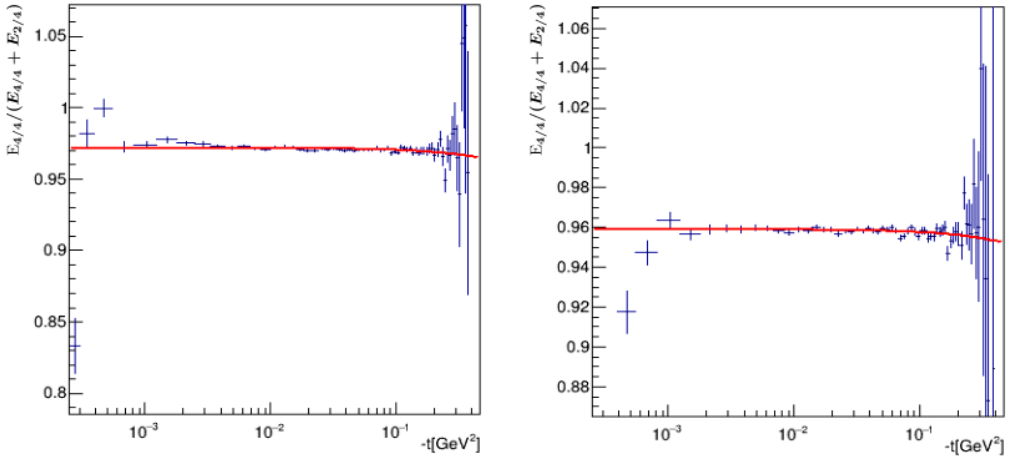

(c) TopologyID 12 (d) TopologyID 13

FIGURE 5.30: Ratios of the background and phase space corrected partial reconstruction efficiency for the "2/4"-event class with given event counts E_i, where index i indicates the 4/4 and failed topology respectively.

5.3.5 Characteristics of events in failed topologies

Table 5.6 shows the cutflow on the number of events for each data-driven topology exemplary for run 309039. The same tables for the remaining runs are given

in appendix A. The first column denotes the topology ID as introduced before with the addition of the two golden topologies which are denoted with ID 0 for arm 1 and ID 1 for arm 2. The second column shows the raw number of events with given elastic trigger signals. In successive steps those numbers are reduced, first by applying the fiducial cuts on the detector edge and beam screen edge (third column). The forth column shows how these numbers are further reduced after application of the geometric correlation cuts. For these numbers, irreducible background count is estimated using the event mixing method with the DPE model extension. The total number of background events estimated is given in the column labeled "total BG". This is the sum of the background estimated from the event mixing templates "EM-BG" and the background estimated by the DPE "DPE-BG". As explained before, the event mixing and DPE templates are scaled simultaneously in such a way that the sum of the two templates best describe the background in the off-momentum and off-orbit region simultaneously. For the golden "4/4" event samples, this results for instance in the observation, that only very few uncorrelated background events from the event mixing template are required to explain the background, while the majority of background is estimated to come from DPE. This is plausible by a visual comparison of figures 5.16, 5.17 and 5.20. The most prominent background features in 5.16 are located in the bands, labeled "A" and "E" which are the bands which are populated by the DPE 5.20. The band "A" is also present in the event mixing template 5.17, however is there weaker than the other ones, while it is more prominent in the data. The ratio of the total background number over the total number after geometric selection cuts (background fraction) is given in the column "BG frac". This quantity is also given as "partial fractions" from the DPE- and event mixing background. The estimated total background count is subtracted from the remaining events after geometric selection cuts, resulting in numbers given in the column "After BG sub". These numbers are corrected for acceptance effects by the EOFs, resulting in the final event numbers for any given topology which are printed in column "After EOF". For illustration, the EOFs are printed in the column "EOF". These phase space corrections are of course t-dependent. Here, an integrated global number is

given for illustration.

We notice immediately, that most raw events with an elastic trigger present have reconstructed tracks in all four detectors (Topology IDs 0 and 1) within the order of a million events each. Most events with elastic trigger in the failed topologies are in the "2/4" topologies, indicating a high prevalence of upstream shower events in this data taking, which will be examined in more detail further down. After estimating the actual number of elastic events in those sample ("After EOF"), we see the same order of magnitude of events in the "3/4i" and "2/4" samples. The number of estimated elastic events from the "3/4o" topologies are almost negligible. Interesting to note is the high background fraction in the "2/4" sample. A further observation that stands out is the higher prevalence of "3/4i" events on A-Side (IDs 2 and 3) compared to C-Side (IDs 4 and 5). This will be further investigated in section 5.4.

As a next step, we take a look at the time evolution of the reconstruction efficiency. It is sufficient at this point to only consider the partial reconstruction efficiency, meaning the efficiency calculated from the numbers above, neglecting any contributions from the "lower topologies" which are calculated statistically in a further step. The partial reconstruction efficiency is given by equation 5.11.

$$\epsilon_{\text{reco,partial}} = \frac{(N_{\text{golden}} - B_{\text{golden}})}{(N_{\text{golden}} - B_{\text{golden}}) + \frac{(N_{3/4\text{i}} - B_{3/4\text{i}})}{\text{EOF}(3/4\text{i})} + \frac{(N_{3/4\text{o}} - B_{3/4\text{o}})}{\text{EOF}(3/4\text{o})} + \frac{(N_{2/4} - B_{2/4})}{\text{EOF}(2/4)}} \tag{5.11}$$

We now plot the temporal evolution of $\epsilon_{\text{reco,partial}}$ with 10-LB time resolution in figure 5.31.

Topo	Triggers	After fid.	After geo	After BG sub	After EOF	EM-BG	DPE-BG	total BG	EM- BG frac	DPE- BG frac	total BG frac	EOF
0	1.29091e+06	1.2791e+06	1.22179e+06	1220168	1220168	10	1615	1625	8.24844e-06	0.00132242	0.00133067	1
1	1.27095e+06	1.25825e+06	1.20404e+06	1202084	1202084	5	1948	1953	4.26214e-06	0.00161837	0.00162263	1
2	91362	89853	80823	80449	80262	267	106	373	0.00330589	0.00131981	0.0046257	1.00233
3	102660	99850	90186	89632	89488	407	145	553	0.00452157	0.00161367	0.00613524	1.00161
4	94486	83011	51927	51649	51046	209	68	277	0.00402621	0.00131885	0.00534506	1.01182
5	84027	78091	54619	54284	53573	246	88	334	0.00451907	0.00161367	0.00613275	1.01326
6	9233	7808	1491	1454	1452	34	1	36	0.023222	0.00129343	0.0245154	1.001
7	8102	6954	2280	2204	2202	71	3	75	0.0313863	0.00157012	0.0329564	1.00123
8	20569	17993	6896	6719	6709	167	8	176	0.0242844	0.00129203	0.0255765	1.00158
9	13914	12279	4491	4359	4354	124	7	131	0.027811	0.00157592	0.0293869	1.00111
10	203558	181502	33354	25231	24878	8088	33	8122	0.242518	0.00100305	0.243521	1.01418
11	169051	160312	58666	41154	40946	17457	54	17511	0.297571	0.000930146	0.298501	1.00506
12	148124	131317	45932	36894	36153	8978	59	9037	0.195463	0.00130415	0.196767	1.02047
13	167592	154517	68527	52940	52756	15500	85	15586	0.226202	0.00125433	0.227456	1.00348

TABLE 5.6: Event cutflow for all data driven event topologies exemplary for run 309039. The table shows the two golden topologies with IDs 0 and 1, the 3/4i cases with IDs 2 to 5, the 3/4o cases with IDs 6 to 9 and the 2/4 cases with IDs 10 to 13. From left to right we have in the columns: The raw rate with just elastic triggers present, remaining events after fiducial cuts, remaining events after geometric correlation cuts, remaining events after background subtraction, remaining events after phase space correction (EOF), the subtracted background count determined by event mixing, the subtracted background count determined by DPE simulation, total background count, the background fraction and the phase space correction factors.

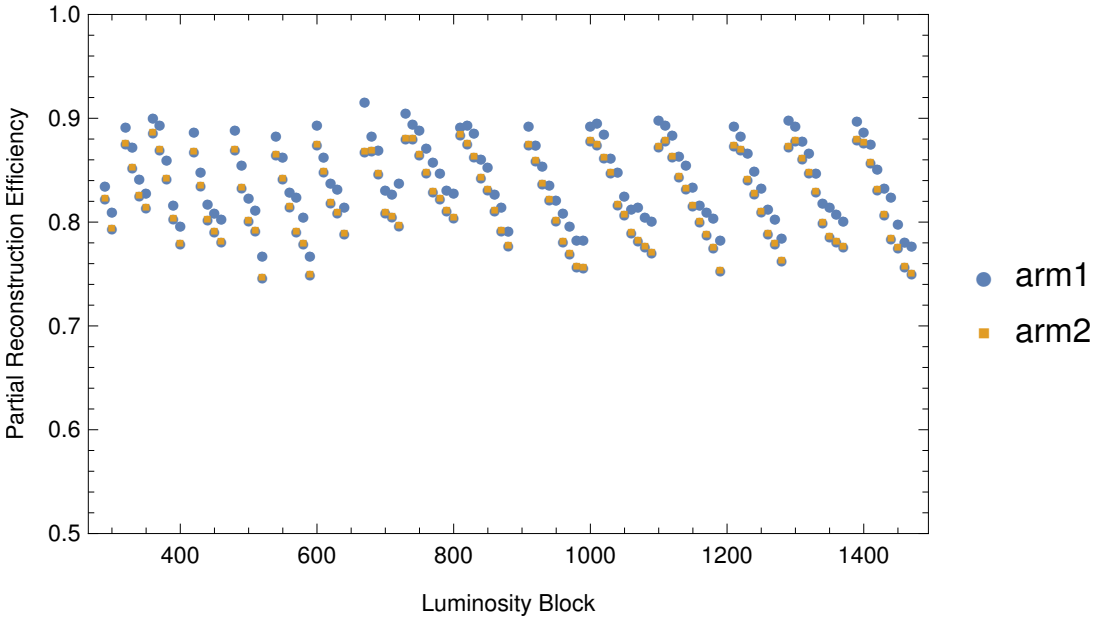

FIGURE 5.31: Time evolution of the partial reconstruction efficiency (data driven event topologies) for both spectrometer arms, exemplary for run 309039

The plot shows a periodic, almost linear decrease of the partial reconstruction efficiency over time, recovering to some initial value each time before the decrease. The observation is a result of the beam conditions of the $\beta^* = 2.5\,\mathrm{km}$ runs. Each data taking period (translating into a period of decreasing reconstruction efficiency) is interrupted by a beam scraping procedure which cleans out any beam halo buildup which accumulates over time. In figure 5.16 these are mostly the regions B, C and D. The lowering of the efficiency coinciding with increasing buildup is a strong indicator that the low reconstruction efficiency in the $\beta^* = 2.5\,\mathrm{km}$ campaign is causal to the presence of halo background.

We can examine the temporal behavior of the reconstruction efficiency in more detail by plotting a topology based partial efficiency by plotting equation 5.12, where N_i is the number of events in any single data driven failed topology.

$$\epsilon_{\mathrm{reco,partial}} = \frac{(N_{\mathrm{golden}} - B_{\mathrm{golden}})}{(N_{\mathrm{golden}} - B_{\mathrm{golden}}) + \frac{(N_\mathrm{i} - B_\mathrm{i})}{\mathrm{EOF(i)}}} \tag{5.12}$$

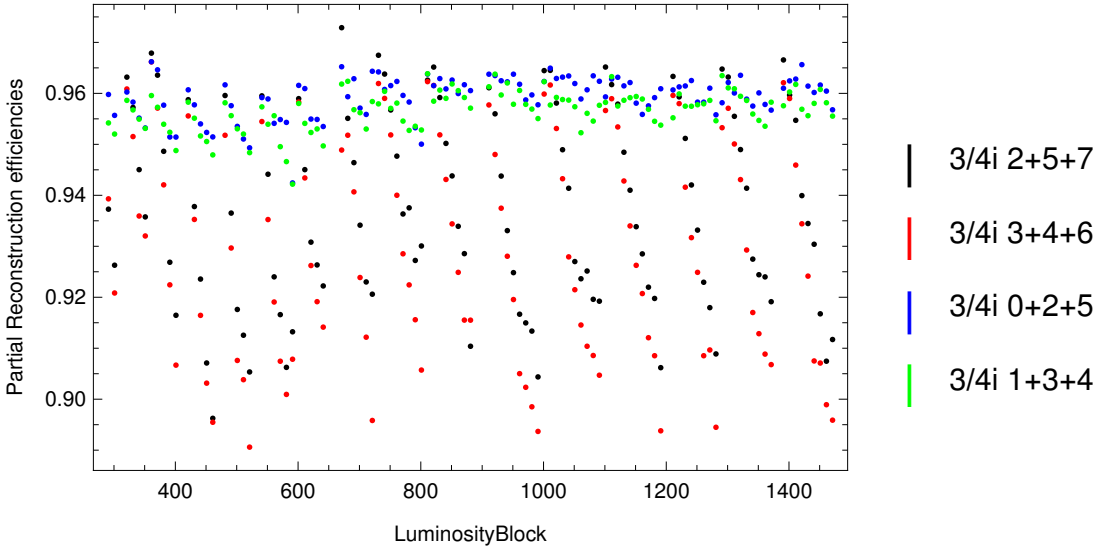

FIGURE 5.32: Time evolution of the individual topology contributions to the partial reconstruction efficiency (data driven event topologies), exemplary for run 309039

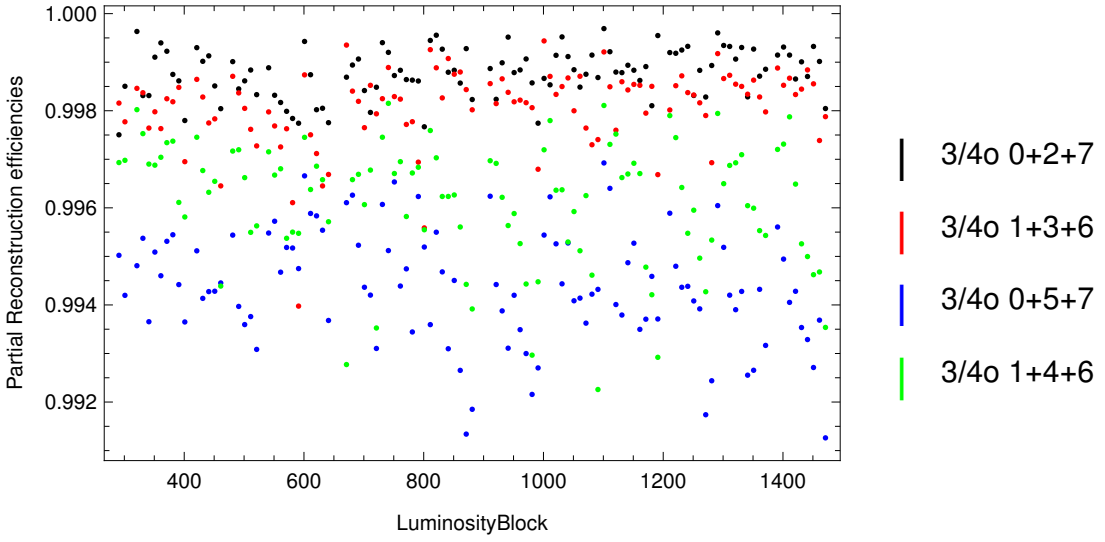

FIGURE 5.33: Time evolution of the individual topology contributions to the partial reconstruction efficiency (data driven event topologies), exemplary for run 309039

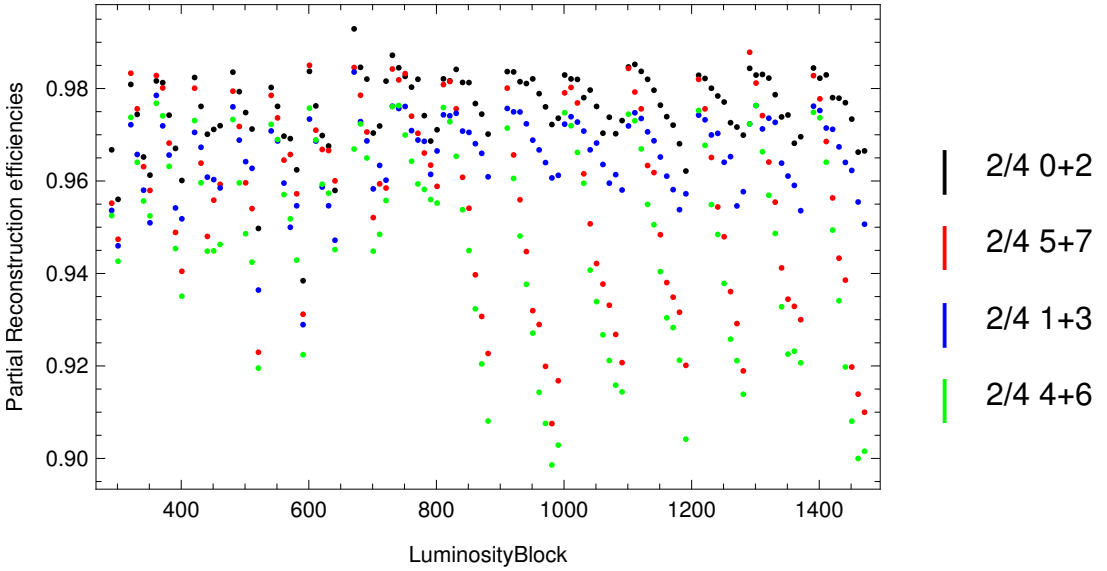

FIGURE 5.34: Time evolution of the individual topology contributions to the partial reconstruction efficiency (data driven event topologies), exemplary for run 309039

This representation lets us examine the time dependency of the contribution of each of the failed background topologies to the reconstruction (in)efficiency. The plots are shown without statistical error bars on each data point, since this makes the plot more readable. The error bars are small compared to the overall trends that are visible. The "3/4o" topologies, plotted in figure 5.33, have the least impact on the reconstruction efficiency (partial reconstruction value of close to 1) and the temporal evolution of the event count is fairly constant. In the beginning of each data taking period (directly after beam scraping), the "3/4i" events (figure 5.32) are the most dominant (indicated by the lowest partial efficiency value). Hereby the subtopologies where the failed detector is on A-Side (IDs 2 and 3) have a steeper decrease in time than for the C-Side "3/4i" topologies, indicating background buildup happens more quickly on A-Side. The same observation holds for the two "2/4" sub-topologies (figure 5.34), where the tracking failure is on A-Side, at least for most of the data taking periods. Single periods appear to exist, where the influence of the "2/4-partial efficiency" exceeds that of the "3/4i" one. Overall in the beginning of each data taking period, the level of partial "2/4" efficiency is higher than for the "3/4i" one, as in previous $\beta^* = 90\,\mathrm{m}$ analysis.

A further interesting observable is the estimated background pollution over time for the failed topologies. Those are shown in figures 5.35 for the 3/4i topologies and 5.36 for the 2/4 topologies. The plots use a time resolution of 10 LBs per data point. In plot 5.35 we can make out a general increasing trend of the background fraction within the scraping periods, however there is too much fluctuation on these low background fraction of the 3/4i topologies. In plot 5.36 for the 2/4 topologies however we can see a clear trend of rapidly increasing background fraction over time.

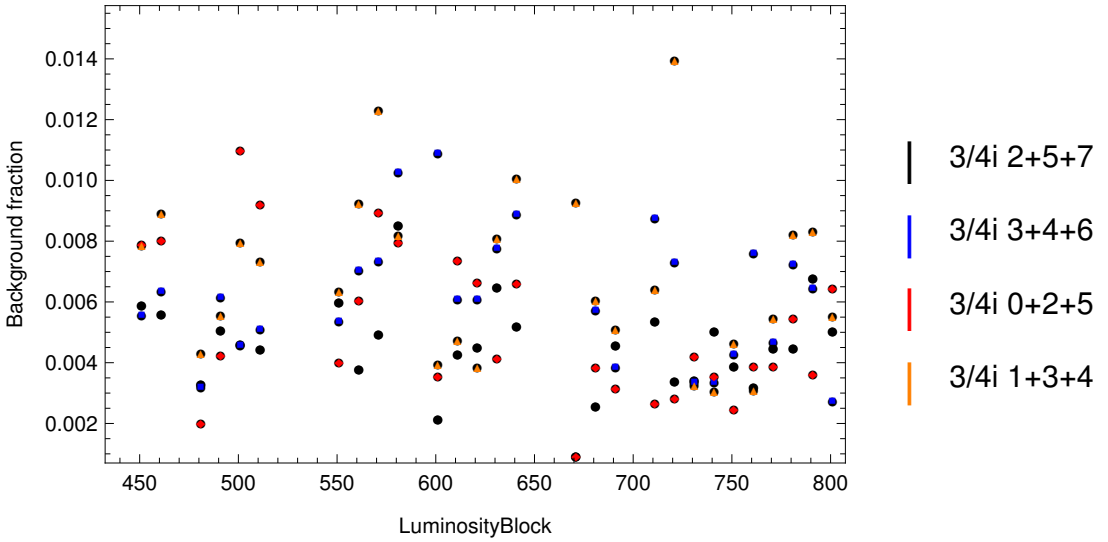

FIGURE 5.35: Time dependence of the background fraction for all 3/4i subtopologies, exemplary for run 309039

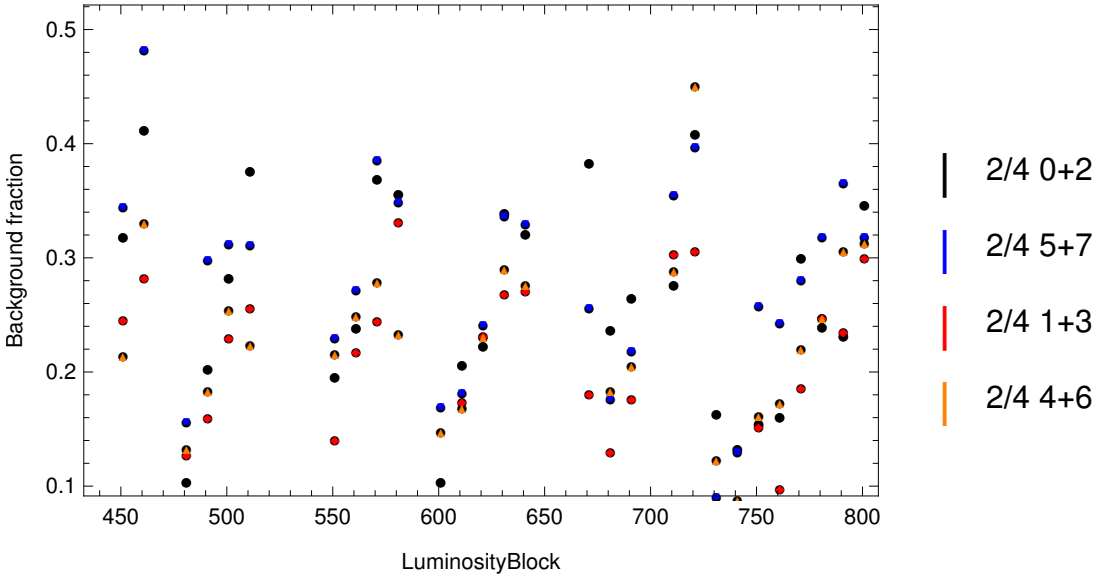

FIGURE 5.36: Time dependence of the background fraction for all 2/4 subtopologies, exemplary for run 309039

We found, that there is a clear correlation between the measured background fraction within a 10 LB block and the estimated partial reconstruction efficiency. This correlation is shown in figure 5.37 for the 2/4 subtopologies and in figure 5.38 for the 3/4 subtopologies:

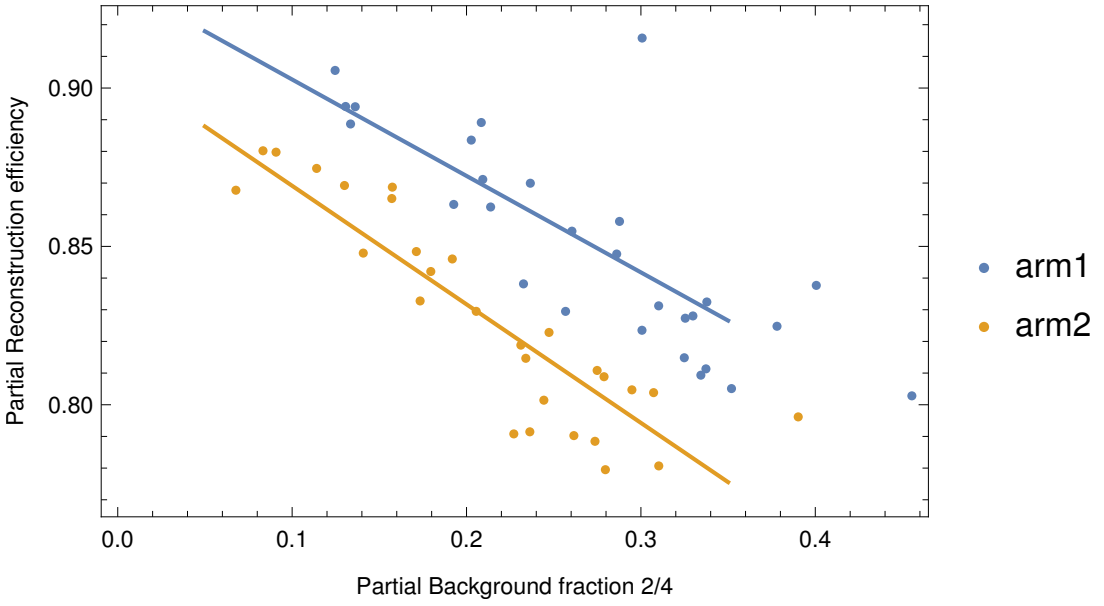

FIGURE 5.37: Correlation of estimated background fraction in 2/4 events per arm vs. the partial 2/4 reconstruction efficiency

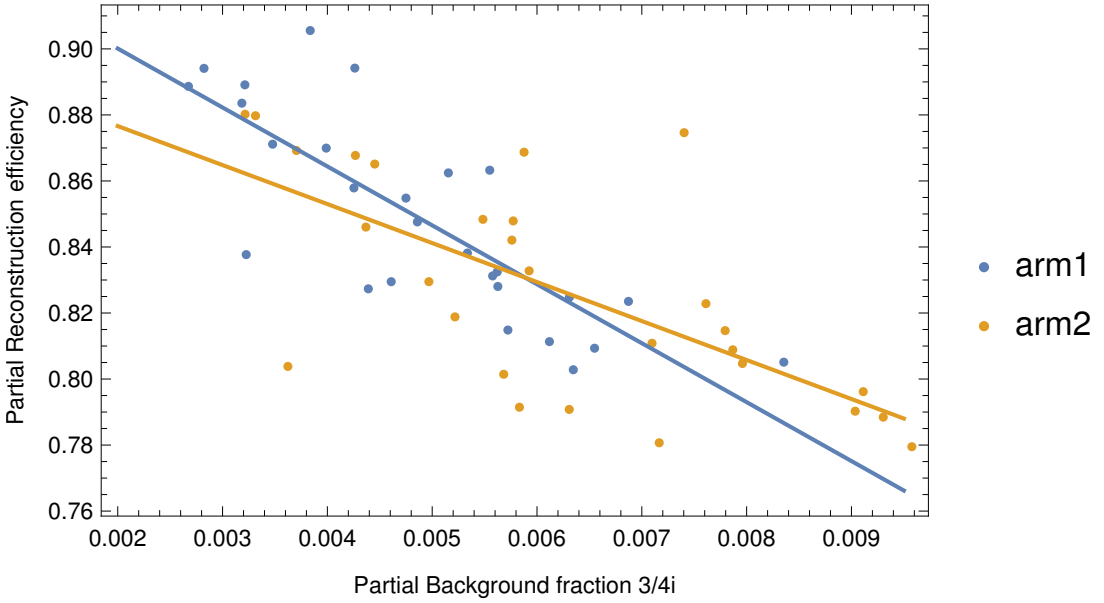

FIGURE 5.38: Correlation of estimated background fraction in 3/4i events per arm vs. the partial 3/4i reconstruction efficiency

The data points can be described by a linear fit per arm, which yields the line equations in 5.37 for 2/4:

$$f(x) = 0.933 - 0.305x \tag{5.13}$$

for arm 1 and

$$f(x) = 0.907 - 0.374x \tag{5.14}$$

for arm 2 respectively. Where x is the background fraction, $f(x)$ is the partial reconstruction efficiency. Also we yield correlations for the 3/4i sample in 5.38:

$$f(x) = 0.936 - 17.850x \tag{5.15}$$

for arm 1 and

$$f(x) = 0.900 - 11.810x \tag{5.16}$$

This shows, that there is a clear correlation about the reconstruction efficiency we obtain, and the amount of background from which the samples are polluted. It

doesn't however imply a causal link. The background in the failed topologies that we reconstruct can not be the cause of reconstruction failure. It just implies, that when there is a reconstruction failure in one or two adjacent detectors, more background is around and picked up by the remaining detectors with tracks. In section 5.4 the cause of the temporal decrease of reconstruction efficiency will be linked to the time dependent "shower probability", which is an observable independent of the reconstruction efficiency analysis and thus much more meaningful. This also means that it is in principle not possible to obtain a higher reconstruction efficiency by any means of background suppression technique in the analysis procedure.

5.3.6 Statistical extrapolation to lower topologies

The event number N_{lower} from equation 5.10 is calculated statistically based on the determined event numbers from the data driven topologies. The "lower failed topologies" consist of any type of topology, where no cut on position vs. local angle is possible. These include constellations, where only one detector on each side from the interaction point has reconstructed tracks, or there is only one detector out of four, or even none of the four detectors have reconstructed tracks. This includes even such peculiar constellations such that we have e.g. one inner detector on A-side with reconstructed tracks and not the outer one and on C-side we have the outer one with reconstructed tracks but not the inner one. In previous $\beta^* = 90\,\text{m}$ analysis, most of these lower topologies were data driven. In the first ALFA analysis at $\sqrt{s} = 7\,\text{TeV}$, everything except the "0/4" topologies were data driven [28]. This assumed the presence of a range in the vertical plane of the elastic event selection in those lower topologies, where background pollution and acceptance effects were negligible and the total number of elastic events in those lower topologies could be determined by a "4/4" template fit on this range (a kind of interpolation). For the $\sqrt{s} = 8\,\text{TeV}$ analysis [33], the author of this thesis kept this basic approach. Modifications were the introduction of the phase space corrections (EOFs), a different approach to calculate the "0/4" event numbers

and at last a statistical calculation of the expected number of "1/4o" event counts instead of data driven (events, where one outer detector has provided tracks and none else). Since large amounts of beam based background in the current data sets make it impossible to do a reliable event selection and background estimation on those lower topologies, the event numbers for those are now all determined purely statistical from higher topologies.
For the derivation of the formulas for each of the lower topologies, lets assume that E_{total} is the total number of elastic events within the acceptance region of the according spectrometer arm, so the sum over all final event numbers from all topologies, we get a set of equations, based on the probability p_{ij} of track reconstruction:

$$p_{ij} \cdot p_{kl} \cdot E_{\text{total}} = E_{ijkl} \tag{5.17}$$

The four indexes i through l denote the four detectors that make up a spectrometer arm. The pairs i, j and k, l are for the two detectors on A-side and C-side respectively. The indexes have either the value "true" or "false" whether the corresponding detector shall be assumed to have a reconstructed track(s) present or not. E_{ijlk} is then the event number for this given topology.
As an example, the event number in the "0/4" topology in arm 1 $E_{!0!2!5!7}$ is given by the probability of not having any tracks in both detectors reconstructed on A-Side $p_{!0!2}$ times the probability of the same on C-Side $p_{!5!7}$ times the total number of elastic events $E_{\text{total, arm1}}$. Neither the total number of elastic events in the acceptance region nor any of the probabilities are observables, so all numbers E_{ijlk} of interest are expressed in equations which depend only on measured background and acceptance corrected event numbers in higher failed topologies.

This gives in equation 5.18 for all lower failed topologies the estimated event number E_i, where i is the topologyID, as defined in figures 5.5, 5.6, 5.22, 5.25, 5.28 and 5.39:

$$
\begin{aligned}
E_{14} &= E_2 \cdot E_4/E_0 \\
E_{15} &= E_8 \cdot E_6/E_0 \\
E_{16} &= E_3 \cdot E_5/E_1 \\
E_{17} &= E_9 \cdot E_7/E_1 \\
E_{18} &= E_2 \cdot E_6/E_0 \\
E_{19} &= E_8 \cdot E_4/E_0 \\
E_{20} &= E_3 \cdot E_7/E_1 \\
E_{21} &= E_9 \cdot E_5/E_1 \\
E_{22} &= E_8 \cdot E_{10}/E_0 \\
E_{23} &= E_2 \cdot E_{10}/E_0 \\
E_{24} &= E_4 \cdot E_{11}/E_0 \\
E_{25} &= E_6 \cdot E_{11}/E_0 \\
E_{26} &= E_9 \cdot E_{12}/E_1 \\
E_{27} &= E_3 \cdot E_{12}/E_1 \\
E_{28} &= E_5 \cdot E_{13}/E_1 \\
E_{29} &= E_7 \cdot E_{13}/E_1 \\
E_{0a} &= E_{10} \cdot E_{11}/E_0 \\
E_{0b} &= E_{12} \cdot E_{13}/E_1
\end{aligned}
\tag{5.18}
$$

which only depend on determined numbers from higher topologies. The exclamation mark shall symbolize that those given detectors provide no tracks. Table 5.7 gives a prediction on how many elastic events reside in the lower topologies.

The definition of the topology IDs is given in figure 5.39:

TopoID	308979	308982	309010	309039	309074	309165	309166
14	537	163	884	3355	1221	1351	1025
15	3	1	4	8	3	3	3
16	595	169	996	3982	1433	1503	1148
17	3	1	4	8	2	3	2
18	22	7	34	95	29	28	24
19	62	19	103	280	108	158	116
20	46	11	61	164	42	41	38
21	35	10	59	194	74	103	73
22	45	14	60	137	47	54	51
23	385	120	515	1636	527	457	452
24	284	78	418	1707	727	678	463
25	12	3	16	49	17	14	11
26	34	9	42	130	44	56	43
27	581	152	712	2677	859	812	676
28	405	104	600	2344	958	964	712
29	31	7	37	97	28	26	24
0a	203	58	244	832	314	230	204
0b	395	94	429	1576	574	520	419

TABLE 5.7: Run-by-run summary of estimated elastic events in lower failed topologies. These calculated values are rounded to the closest integer.

FIGURE 5.39: Definition of the lower topologies. The elastic event count in these topologies is determined by statistical estimation and not by dedicated event selection

5.3.7 Statistical uncertainties in event selection and background subtraction

In previous $\beta^* = 90\,\mathrm{m}$ analysis, the statistical uncertainty of the reconstruction efficiency was determined by simple error propagation. This procedure was attempted also for this analysis framework, however proved to be unfeasible due to the advanced, time dependent background subtraction.

Instead, a simple bootstrap method was applied. For that, the analysis framework was executed more than 400 consecutive times, while simultaneously the bootstrap method was applied to the steps of the framework which are marked with stars in figure 5.21. The t-histograms for the events of the Monte-Carlo-Preprocessing (giving the EOFs), the histograms for the elastic event candidates (SignalLoop) as well as the background template histograms were for each event for each of those three steps filled with a random, Poisson distributed weighting factor using $\lambda = 1$. Figures 5.40 and 5.41 show resulting efficiency distributions. From all reconstruction efficiency distributions and for all runs, the standard deviation is taken as statistical uncertainty, resulting in values given in table 5.8.

Run	Stat.Err. eff. arm 1	Stat.Err. eff. arm 2
308979	0.0009	0.0010
308982	0.0015	0.0015
309010	0.0006	0.0006
309039	0.0004	0.0004
309074	0.0006	0.0007
309165	0.0007	0.0006
309166	0.0005	0.0005

TABLE 5.8: Run-by-run summary of the statistical error on the reconstruction efficiency obtained by the bootstrap method. The run number of each distribution is written at the peak of same.

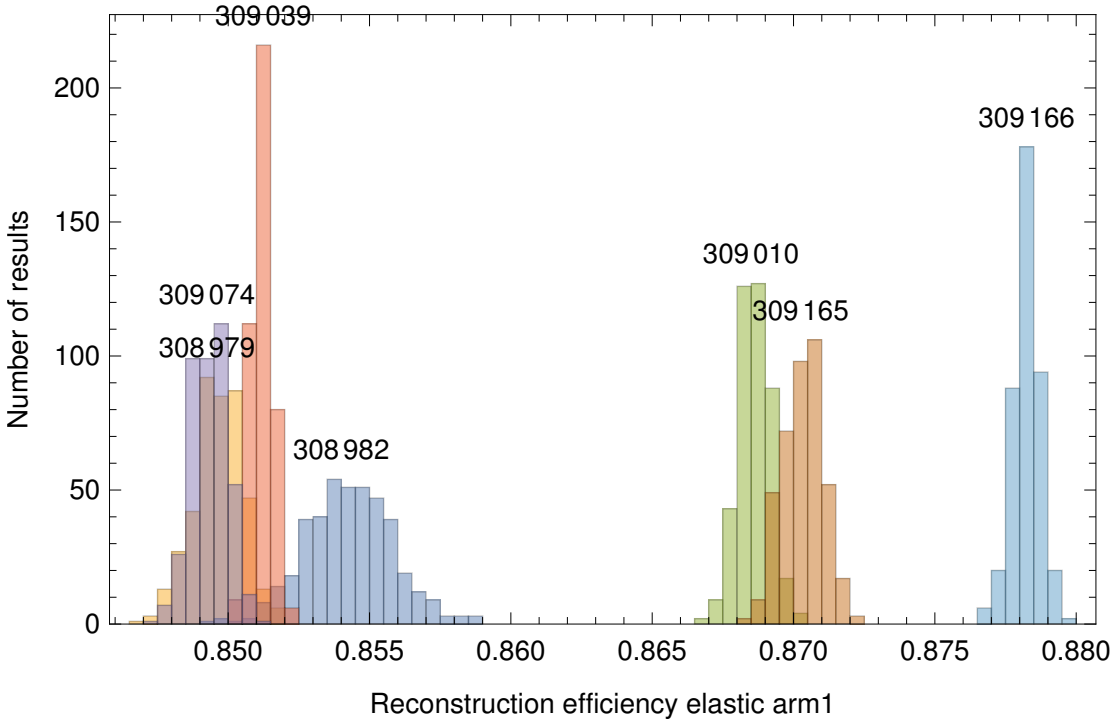

FIGURE 5.40: Spread of reconstruction efficiency value results for elastic arm 1 from all runs by the bootstrap method. The run number of each distribution is written at the peak of same.

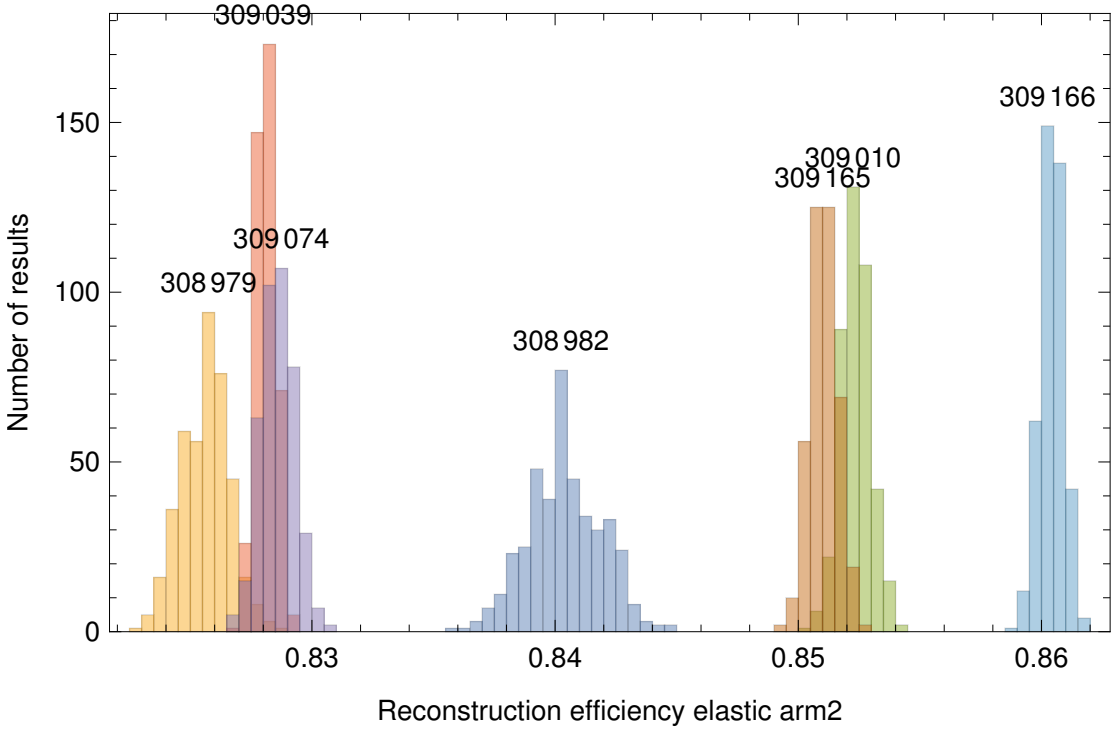

FIGURE 5.41: Spread of reconstruction efficiency value results for elastic arm 2 from all runs by the bootstrap method. The run number of each distribution is written at the peak of same.

5.3.8 Systematic uncertanties in event selection and background subtraction

The method for systematic uncertainty study used here is a combination of what was done in earlier $\beta^* = 90\,\mathrm{m}$ analysis with the addition of an extended treatment of the uncertainty on the background contribution.
For the procedure, a set of analysis parameters is varied within a reasonable range and the variations of the final reconstruction efficiency result are summed up in quadrature to give the systematic error uncertainty. Table 5.9 shows the set of systematic error variations that have been performed:

1. Variation of the position of the detector edge cut between 60 μm and 1 mm
2. Variation of the beam screen cut position between -1 and +1 mm from nominal value
3. Variation of the tightness of the elliptical cut in the x vs. θ_x correlation between 2.0 and 5.0 sigma
4. Variation of the tightness of the cut in the y vs. θ_y correlation between 10 and 40 μ rad displacement from the diagonal
5. Variation of the tightness of the elliptical cut in the x-A-Side vs. x-C-Side correlation between 2.0 and 5.0 sigma
6. Variation of the tightness of the linear cut in the y-A-Side vs. y-C-Side correlation between 0.5 and 2 mm
7. Variation on the minimum number of fibers to be active on a given detector without track reconstruction between 5 and 60 fibers.

Further, some variations were performed to access the stability of the background template. These variations effect the background templates only or their scalings and not the elastic selection:

1. Variation of the lower value of the x vs θ_x region for the background templates

2. Change of trigger requirement for template selection to veto additionally on trigger activity in the vertically opposite armlet

3. Change of trigger requirement to replace the L1_ALFA_Elast15 and L1_ALFA_Elast18 trigger signals with the more tight version (the Elast triggers require for any given armlet (two neighboring detectors on a side) to be a trigger signal present on either one. This variation requires a trigger signal on both)

4. No best-track matching

5. Require minimum bias activity in the central ATLAS detector in order to enhance SD events

6. Use only either only off-momentum region or off-orbit region for background scaling in the failed topologies (However still using both regions for the 4/4 samples, since both regions are required for DPE estimation)

The uncertainties from the background fraction estimates from the latter tests are propagated as uncertanties in the background values B in equation 5.10 and yield a further uncertainty on the global reconstruction efficiency given in the next to last row of table 5.9

Table 5.10 shows for each run and each event topology the uncertainty on the background fraction values.

Exemplary for run 309039, table 5.11 shows the central values of the background fraction for each topology depending on the template or scaling variation that was performed.

Another important test is the reconstruction efficiency determination when requiring stricter data quality levels. For this test, all tracks are discarded that have been reconstructed from less than five clean fiber layers, whereas a clean fiber layer is defined as such, that a layer shall have at most three lit up fibers. Table

Variation	308979	308982	309010	309039	309074	309165	309166
cut x vs. theta x sigma	0.0057	0.0044	0.0029	0.0007	0.0019	0.0040	0.0023
	0.0062	0.0069	0.0034	0.0004	0.0021	0.0025	0.0026
cut xL vs xR sigma	0.0019	0.0017	0.0012	0.0007	0.0043	0.0018	0.0018
	0.0017	0.0006	0.0004	0.0005	0.0053	0.0017	0.0018
cut yL vs yR mm	0.0008	0.0004	0.0004	0.0004	0.0007	0.0015	0.0004
	0.0015	0.0009	0.0006	0.0004	0.0006	0.0002	0.0005
beam screen cut variation [mm]	0.0011	0.0005	0.0003	0.0002	0.0003	0.0009	0.0001
	0.0009	0.0006	0.0003	0.0002	0.0003	0.0010	0.0001
detector edge cut variation [mm]	0.0045	0.0035	0.0025	0.0007	0.0004	0.0057	0.0017
	0.0028	0.0021	0.0060	0.0003	0.0005	0.0019	0.0015
y theta y murad	0.0042	0.0030	0.0039	0.0053	0.0036	0.0029	0.0039
	0.0059	0.0012	0.0033	0.0033	0.0029	0.0012	0.0025
min fibers act.	0.0032	0.0050	0.0040	0.0043	0.0064	0.0017	0.0035
	0.0016	0.0025	0.0006	0.0027	0.0037	0.0013	0.0022
BG fraction	0.0173	0.0045	0.0046	0.0048	0.0046	0.0158	0.0032
	0.0189	0.0030	0.0169	0.0043	0.0063	0.0046	0.0026
Total	0.0197	0.0094	0.0083	0.0085	0.0099	0.0178	0.0070
	0.0212	0.0084	0.0186	0.0061	0.0098	0.0061	0.0055

TABLE 5.9: Run-by-run summary of systematic uncertainties for the reconstruction efficiency. The first number in each cell is for spectrometer arm 1, while the second number in each cell is for arm 2.

TopoID	308979	308982	309010	309039	309074	309165	309166
0	0.0006	0.0007	0.0007	0.0007	0.0007	0.0006	0.0006
1	0.0008	0.0007	0.0008	0.0008	0.0008	0.0008	0.0008
2	0.0015	0.0039	0.0026	0.0024	0.0032	0.0017	0.0027
3	0.0024	0.0032	0.0034	0.0037	0.0044	0.0012	0.0026
4	0.0014	0.0040	0.0028	0.0036	0.0020	0.0017	0.0024
5	0.0022	0.0034	0.0024	0.0038	0.0035	0.0017	0.0029
6	0.0103	0.0101	0.0083	0.0127	0.0057	0.0071	0.0107
7	0.0123	0.0058	0.0184	0.0138	0.0187	0.0053	0.0069
8	0.0050	0.0082	0.0093	0.0080	0.0103	0.0044	0.0106
9	0.0104	0.0241	0.0129	0.0104	0.0135	0.0036	0.0090
10	0.1283	0.0492	0.0593	0.0704	0.0472	0.1943	0.0503
11	0.0996	0.0366	0.0606	0.0595	0.0727	0.0552	0.0834
12	0.1282	0.0400	0.1504	0.0502	0.0637	0.0857	0.0436
13	0.0575	0.0400	0.0524	0.0573	0.0841	0.0313	0.0602

TABLE 5.10: Systematic uncertanties on the central values of the background fractions for each run and each topology

TopologyID	nominal	Hard trigger	Require Minbias	Off-orbit	Off-momentum	Track 0
0	0.0013	0.0013	0.0013	0.0013*	0.0013*	0.0013
1	0.0016	0.0016	0.0016	0.0016*	0.0016*	0.0016
2	0.0046	0.0050	0.0064	0.0049	0.0016	0.0041
3	0.0061	0.0059	0.0091	0.0071	0.0018	0.0054
4	0.0053	0.0055	0.0078	0.0071	0.0006	0.0045
5	0.0061	0.0067	0.0087	0.0075	0.0012	0.0051
6	0.0245	0.0215	0.0382	0.0355	0.0127	0.0229
7	0.0330	0.0316	0.0456	0.0430	0.0180	0.0285
8	0.0256	0.0207	0.0365	0.0293	0.0206	0.0235
9	0.0294	0.0287	0.0419	0.0338	0.0212	0.0266
10	0.2435	0.2504	0.3225	0.3005	0.1818	0.2344
11	0.2985	0.3091	0.3916	0.3176	0.2727	0.3012
12	0.1968	0.2141	0.2516	0.2294	0.1511	0.1900
13	0.2275	0.2575	0.3105	0.2549	0.1958	0.2308

TABLE 5.11: Estimated Background fraction per topology using various methods of template construction/scaling for run 309039. Numbers marked with * means that this variation was not performed in the golden topologies, since those require both off-orbit and off-momentum normalization regions to include the simultaneous DPE and event mixing scaling.

Run	Efficiency arm 1	Efficiency arm 2
308979	0.793749	0.785789
308982	0.7971	0.801052
309010	0.811903	0.813706
309039	0.794374	0.787465
309074	0.790091	0.786716
309165	0.815162	0.813912
309166	0.825904	0.823956

TABLE 5.12: Run-by-run summary of Event Reconstruction efficiency requiring five instead of three good layers for track reconstruction.

5.12 shows the result of this test. The efficiencies are significantly decreased as one would naively expect, however a peculiar observation we have in this data taking campaign is the fact, that the elastic arm 1 efficiency comes close to the one of elastic arm 2. This is due to the fact, that in elastic arm 1 the two detectors on A-side had a timing problem at the time of the data taking, causing for some events complete fiber layers without tracking information. At stricter data quality requirement, this effect becomes visible.

The contributions from the individual systematic error contributions are displayed in table 5.9 for the reconstruction efficiency in both spectrometer arms. The quadratic sum from these contributions is given in the last row.

5.3.9 Results

Table 5.13 gives the final reconstruction efficiency and golden background fraction results with their respective errors.

Derived from that, we can extract a ratio of the efficiency of arm1 over arm2 in table 5.14, which is needed in turn in the vertical part of the alignment procedure.

The errors are calculated by error propagation, however taking the covariance between the efficiency values into account, according to equation 5.19.

Run	eff1	stat	syst	total	eff2	stat	syst	total
308979	0.8589	0.0009	0.0197	0.0197	0.8337	0.0010	0.0212	0.0212
308982	0.8536	0.0015	0.0094	0.0095	0.8391	0.0015	0.0084	0.0085
309010	0.8686	0.0006	0.0083	0.0083	0.8580	0.0006	0.0186	0.0186
309039	0.8490	0.0004	0.0085	0.0085	0.8255	0.0004	0.0061	0.0061
309074	0.8463	0.0006	0.0099	0.0099	0.8236	0.0007	0.0098	0.0098
309165	0.8792	0.0007	0.0178	0.0178	0.8554	0.0006	0.0061	0.0061
309166	0.8765	0.0005	0.0070	0.0070	0.8587	0.0005	0.0055	0.0055

TABLE 5.13: Run-by-run summary of Event Reconstruction efficiency per spectrometer arm with respective errors.

Run	Ratio efficiency arm 1/2	Total Error on Ratio
308979	1.0302	0.0333
308982	1.0173	0.0152
309010	1.0124	0.0264
309039	1.0285	0.0127
309074	1.0276	0.0141
309165	1.0278	0.0227
309166	1.0207	0.0099

TABLE 5.14: Ratios of the reconstruction efficiencies elastic arm 1 over elastic arm 2 with respective uncertainty.

$$\Delta R = \frac{\epsilon_{\text{arm1}}}{\epsilon_{\text{arm2}}} \sqrt{\left(\frac{\sigma_{\epsilon_{\text{arm1}}}}{\epsilon_{\text{arm1}}}\right)^2 + \left(\frac{\sigma_{\epsilon_{\text{arm2}}}}{\epsilon_{\text{arm2}}}\right)^2 - 2\frac{\text{COV}}{\epsilon_{\text{arm1}} * \epsilon_{\text{arm2}}}} \tag{5.19}$$

The plausibility of the shape of the time dependence of the reconstruction efficiency are cross-checked by normalization of the elastic yield. The elastic yield for a given luminosity block in a given run is divided after background subtraction by the luminosity and the reconstruction efficiency. This will theoretically yield a constant value over time, proportional to the elastic cross-section. In figure 5.42 we see this obtained values for each Luminosity Block and run. Within the statistical fluctuations, the values can be considered consistent, indicating a plausible temporal evolution of the reconstruction efficiency.

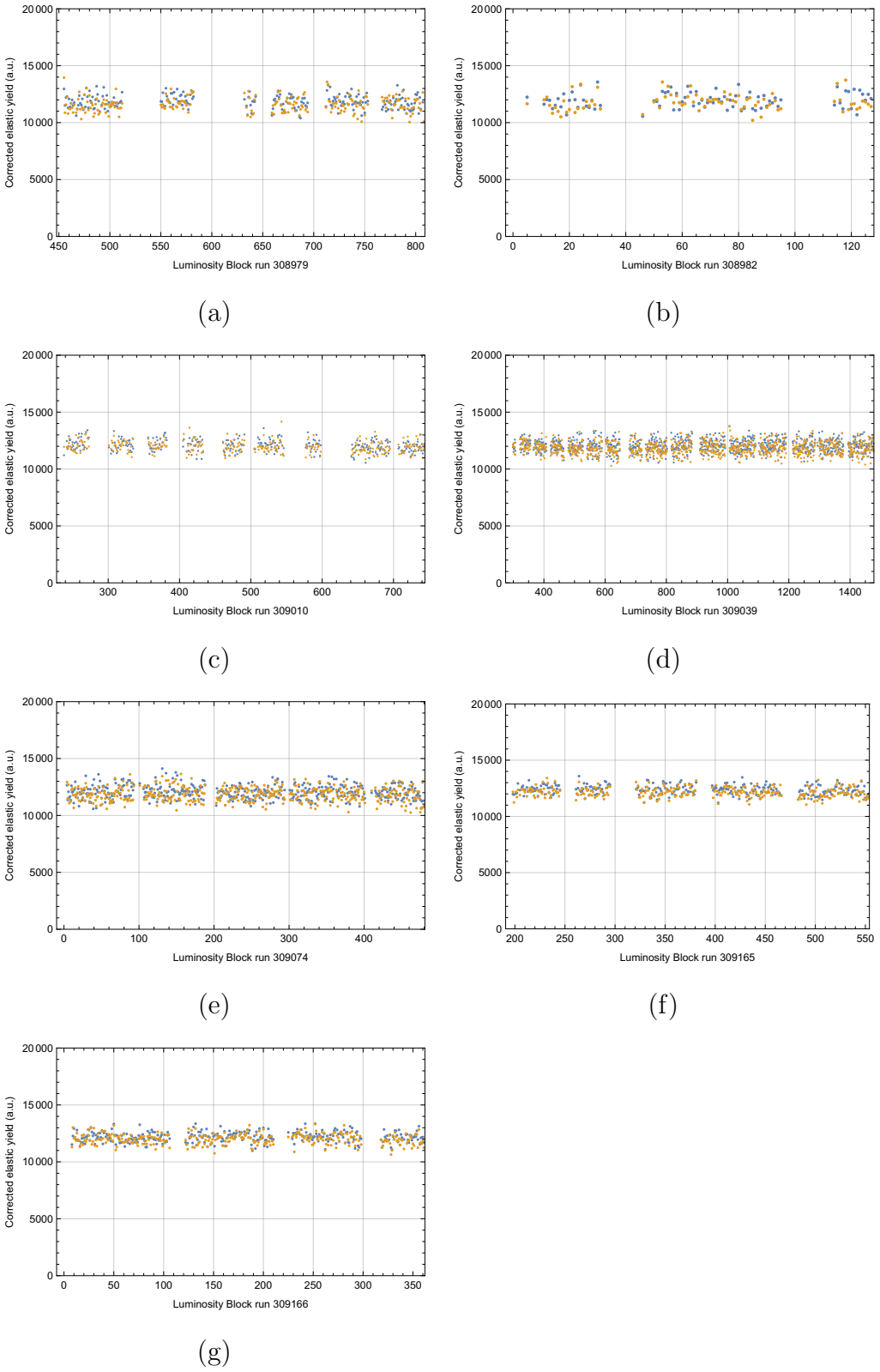

FIGURE 5.42: Elastic yield as a function of time, corrected for the time dependent reconstruction efficiency, background and luminosity.

5.4 Cause of low reconstruction efficency

As we have seen, the reconstruction efficiency values for the runs in the $\beta^* = 2.5\,\text{km}$ campaign are substantially lower than those that were determined for earlier $\beta^* = 90\,\text{m}$ runs [28] [33]. It is important to understand, which causes contribute to a low reconstruction efficiency and why the efficiencies deviate from run to run. The effects on the mentioned timing problem were studied in a dedicated analysis. This was performed by manipulating the $\sqrt{s} = 8\,\text{TeV}$, $\beta^* = 90\,\text{m}$ data in such a way, that on the raw fiber hits, layers were excluded according to the measured layer failure probability from the $\beta^* = 2.5\,\text{km}$ campaign. The $\beta^* = 90\,\text{m}$ tracks were then reconstructed using the manipulated fiber patterns. It was found, that on nominal data quality settings (requiring at least three good layers, which have at most three lit fibers for track reconstruction), the impact on the resulting reconstruction efficiency was marginal. It become however significantly lower, using stricter data quality settings, which is exactly what we observer here in table 5.12. Concluding, that the timing problem does not contribute to the low central values of the reconstruction efficiency in this campaign.
We examine the background hypothesis into more detail, which is confirmed to be the cause of the even lower reconstruction efficiency of the $\sqrt{s} = 8\,\text{TeV}$, $\beta^* = 1\,\text{km-run}$ [34].

We shall at this point further examine the beam background buildup over time as the leading cause of the low overall reconstruction efficiency. For that, the reconstruction efficiency analysis was supplemented to relate the measured reconstruction efficiency values within a 10-Luminosity-Block period to an unbiased measurement of the probability to have a shower-development in ALFA per proton bunch crossing. For the purpose of such unbiased measurements, a special prescaled "Bunch Group Trigger" exists, which gives a trigger signal every time a specific one of the colliding bunch pairs crosses at the ATLAS interaction point. The detector status (e.g. detector triggers, fiber hits, reconstructed tracks) is then saved regardless of whether an interaction with

resulting tracks or showers actually occurs. For each of the runs, the "shower probability" was measured by counting for how many bunch crossings the ALFA detectors on respectively A-Side or C-Side show a high total fiber multiplicity divided by the total number of bunch crossings. An event with "high total fiber multiplicity" is defined as having an event, where both upper and lower inner detectors on a given side from the interaction point show a total fiber multiplicity of over 200 active fibers. We further introduce a quantity "armlet shower probability" which does a similar measurement, but only requires to have shower conditions present in each of the four respective detector armlets (A-side upper, A-side lower, C-side upper, C-side lower, or in detector naming scheme: "B7L1U+A7L1U","B7L1L+A7L1L","B7R1U+A7R1U","B7R1L+A7R1L")

Figure 5.43 shows for each of the seven runs the measurement of the shower probability (to have shower encompassing an entire side from the interaction point) as a function of time (in terms of Luminosity Blocks). A-Side shower probability is indicated by blue data points, while orange data points indicate the shower probability for C-side. We can observe, that the basic tendency is the same for all runs. The shower probability increases with time, but drops to very low values each time a beam scraping was been performed. However there are some striking differences between the individual runs. For runs 308979 (a), 308982 (b), 309010 (c) and 309166 (g) we see, that that the shower probability on C-side rises more quickly than for A-side. Since LHC beam 2 passes trough the ALFA stations on C-side (see figure 3.9), this indicates that for these four runs, the quality of beam 2 deteriorates more quickly then of beam 1. Run 309165 (f) shows a rather equal deterioration of both beam during the first two data taking periods. However later on, beam 1 (A-side, blue data points) stays cleaner than beam 2, just like in the other four mentioned run. We have a reversed situation for runs 309039 (d) and 309074 (e) where A-side shower probability rises significantly more steep than at C-side. These two runs belong to the same LHC fill (see 3.1). We see this difference only later than Luminosity Block 600 in (d).

We can go into more detail by looking at the "armlet shower probability", as shown in figure 5.44. In contrast to the side-wise showers, we can now see a measure

of the up-down asymmetry of the beam quality, which translates into different shower probabilities in upper and lower armlets. The relative magnitudes of these shower pattern differ from the side-wise shower patterns in 5.43. For all runs, both armlets on A-side (red and black data points) show significantly more shower buildup over time than for the C-side armlets, contrary to the side-wise shower patterns, where one LHC fill shows more shower buildup on C-side. In general, except for run 308982 (b), armlet B7L1U+A7L1U (A-side, upper) experiences much more rapid shower buildup than the armlet on the lower vertical plane. Due to the selection requirements, the shower probability in 5.43 is more sensitive to upstream showers, meaning those showers which originate somewhere along the path between interaction point and detectors, e.g. by a halo proton hitting an LHC collimator. The armlet wise shower probability in 5.44 is more sensitive to showers, which originate at the ALFA detectors directly, where shower products do not reach the opposite detectors (upper/lower) of each station.

We can now do a correlation between the measured side-wise shower probabilities and the determined reconstruction efficiencies for the 3/4i event topologies in 5.45 and 5.46. Each data point represents a measurement for a 10 Luminosity Block time period. These plots show a clear correlation between the shower probability and the determined partial reconstruction efficiency. Also, contrary to the correlations shown in figures 5.37 and 5.38, there is no observation bias because the measurement of the shower probability and the measurement of the reconstruction efficiency each use a separate data selection. It is therefore safe to conclude, that the relatively low reconstruction efficiency values observed in this 2.5 km campaign result from higher prevalence of shower-inducing beam background conditions and the variations between the runs stem from observable differences of the LHC beam background characteristics.

It shall be emphasized that not all displayed correlations in these figures make physical sense. For instance, the topologyIDs 2 and 3 (plotted in black and red data points respectively) represent the constellations, where the outer detector on A-side failed to provide reconstructed tracks. For convenience they are also plotted against the shower probability on C-side in figure 5.46, even though a shower on

C-side would not cause detectors on A-side to be effected. The reason, one can see a trend in these correlations as well (even though much less linear) is the fact, that a rising shower probability on C-side coincides with rising shower probabilities on A-side. This means, there is in fact a correlation, however no causal link.
We show the same correlations for the 2/4 events in 5.47 and 5.48 and see basically the same trends. In figure 5.49 the 3/4i partial reconstruction efficiencies are now shown in relation to the armlet wise shower probabilities, exemplary for armlet B7L1U+A7L1U (upper A-side). We see also the basics trends here, concluding that both upstream showers (e.g. collimator hits) as well as halo based detector showers contribute to the efficiency drops.

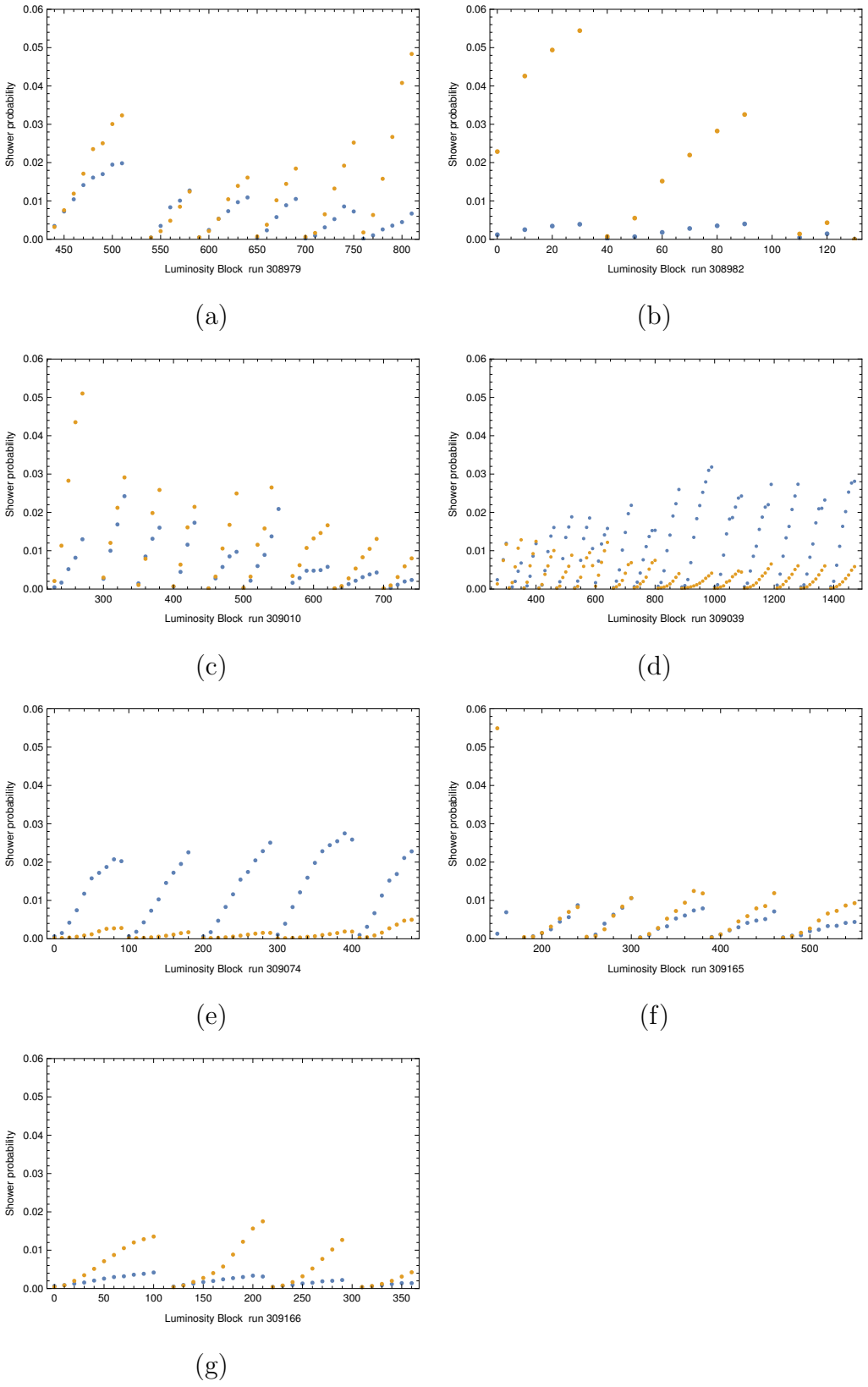

FIGURE 5.43: Shower probability for each run as a function of the Luminosity Block. Blue data points represent A-Side, while orange data points represent C-side.

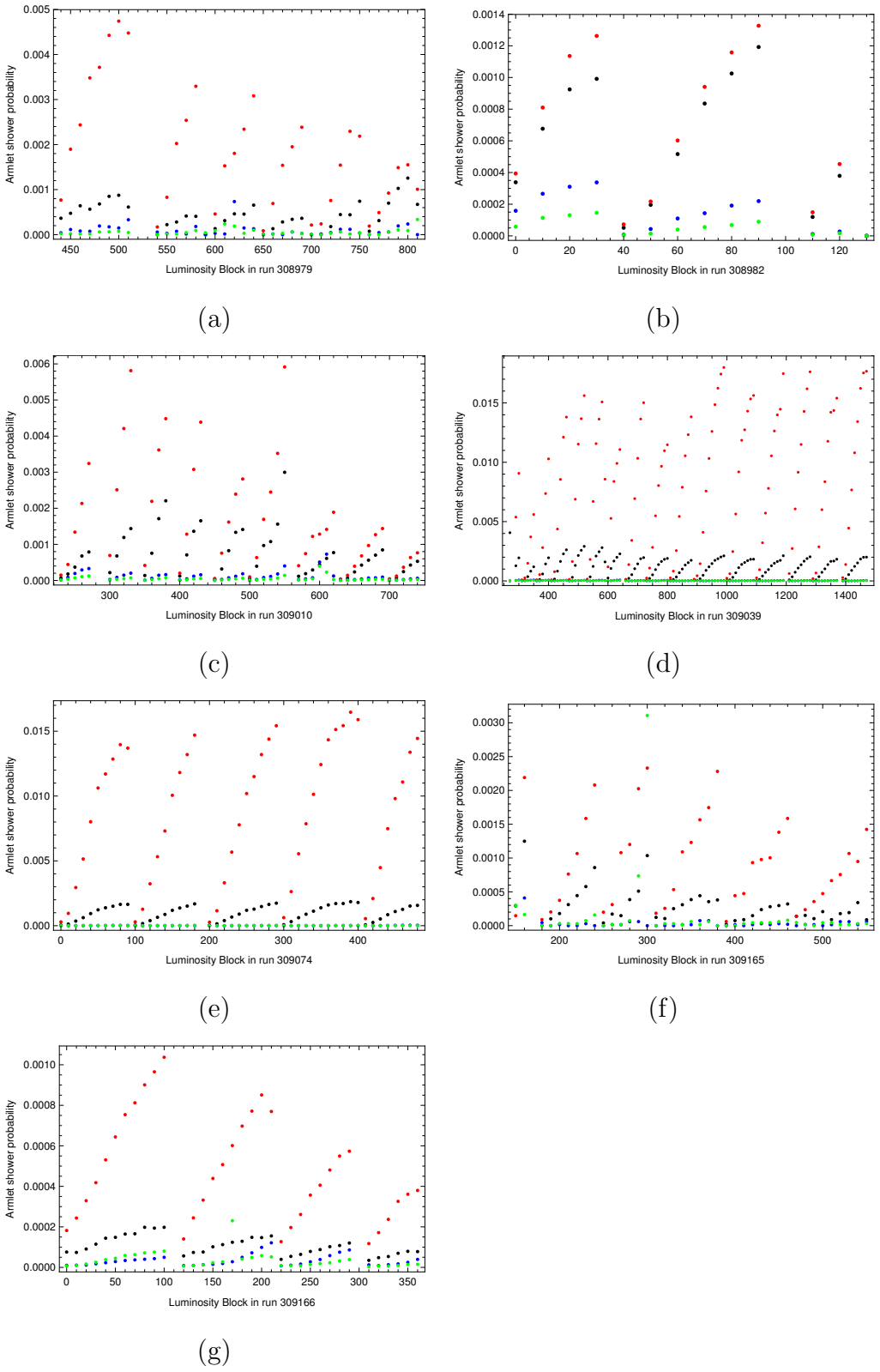

FIGURE 5.44: Shower probability in each of the four armlets as a function of the Luminosity Block. Black data points represent the armlet B7L1U+A7L1U (A-Side, upper vertical plane), red data points represent the armlet B7L1L+A7L1L (A-Side lower vertical plane), blue data points represent the armlet B7R1U+A7R1U (C-Side upper vertical plane), green data points represent the armlet B7R1L+A7R1L (C-Side lower vertical plane)

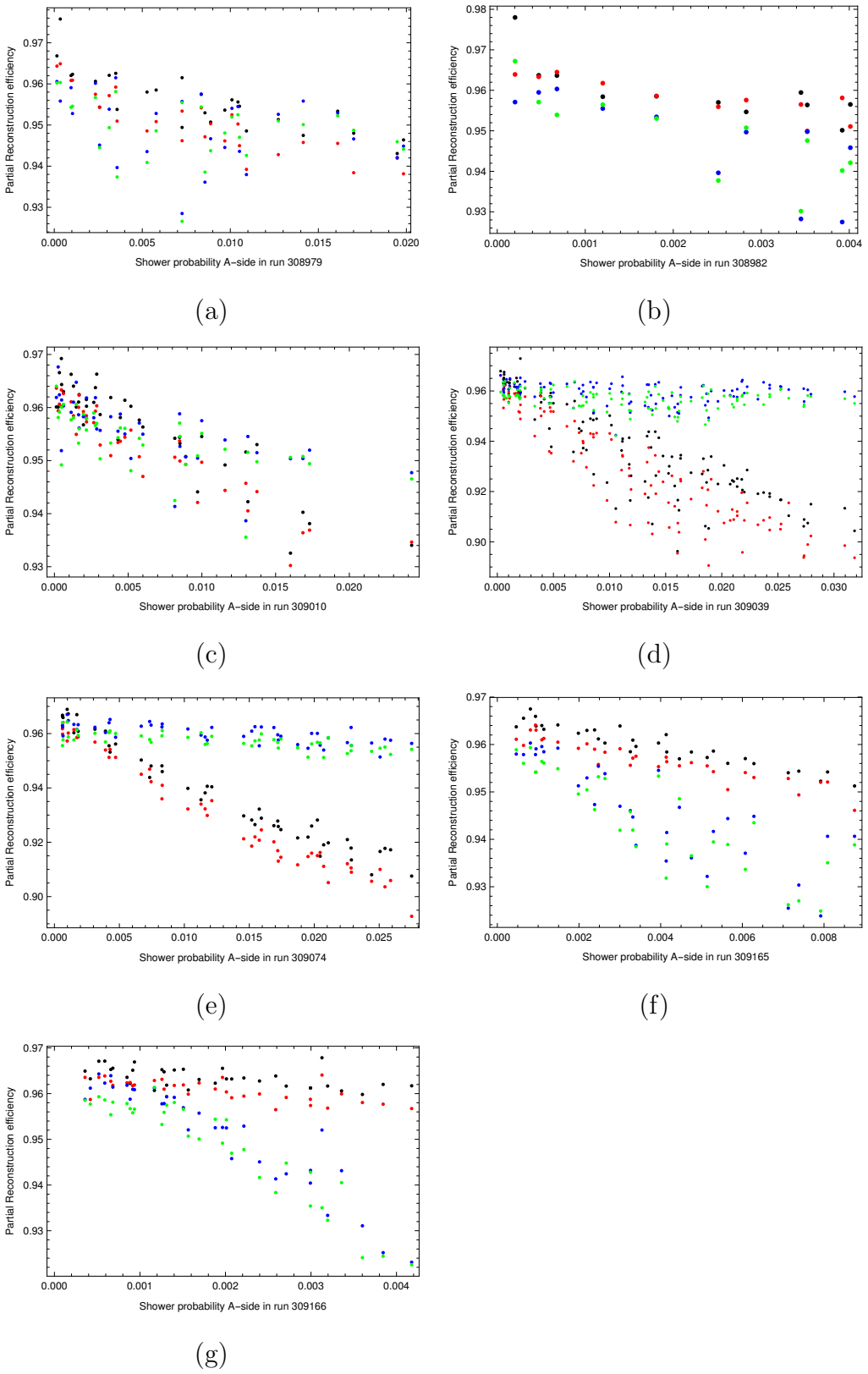

FIGURE 5.45: Correlation of the partial 3/4i reconstruction efficiencies as a function of the shower probability on A-Side. Black data points represent the correlation for topologyID 2, red data points for topologyID 3, blue data points for topologyID 4, green data points for topologyID 5.

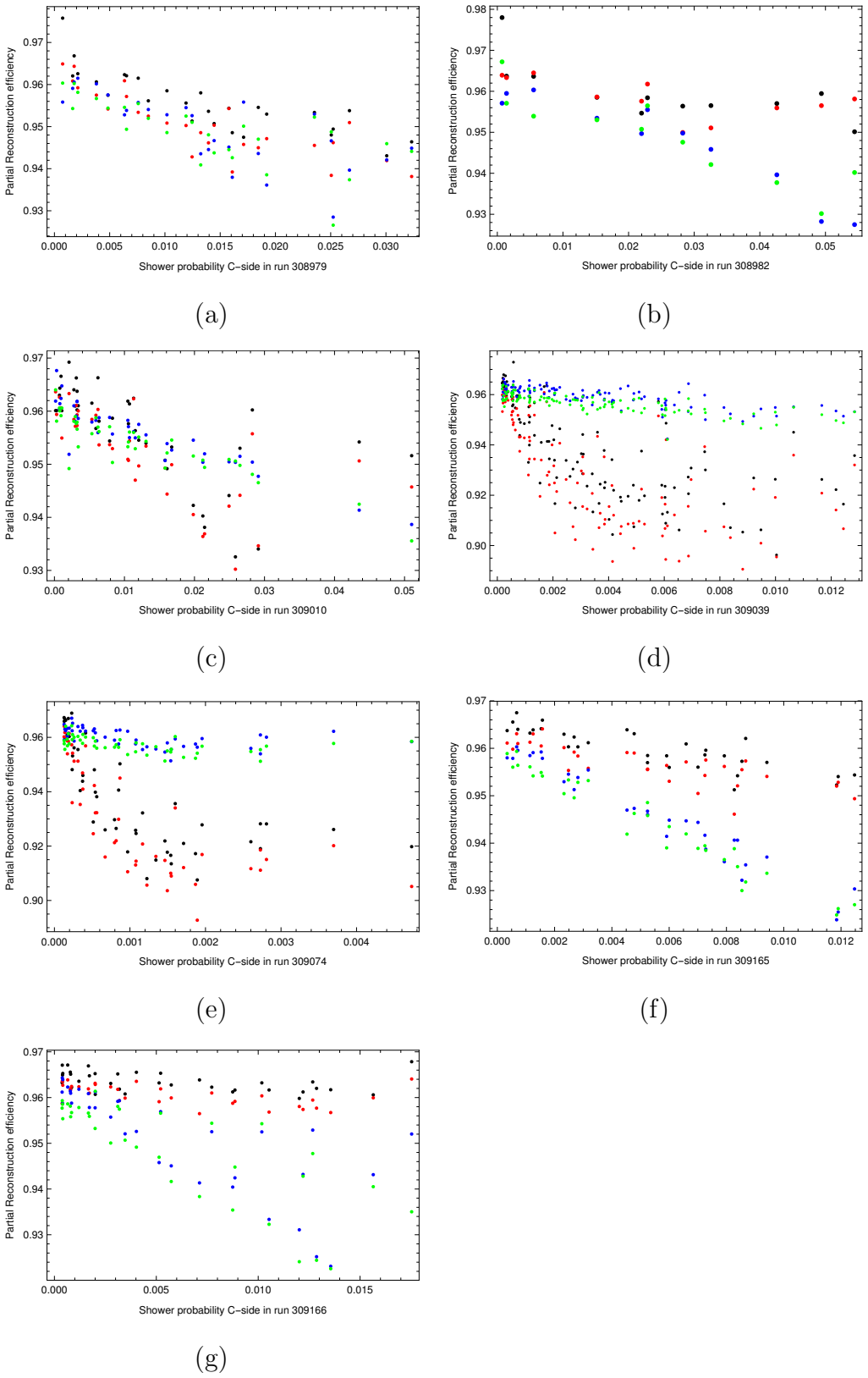

FIGURE 5.46: Correlation of the partial 3/4i reconstruction efficiencies as a function of the shower probability on A-Side. Black data points represent the correlation for topologyID 2, red data points for topologyID 3, blue data points for topologyID 4, green data points for topologyID 5.

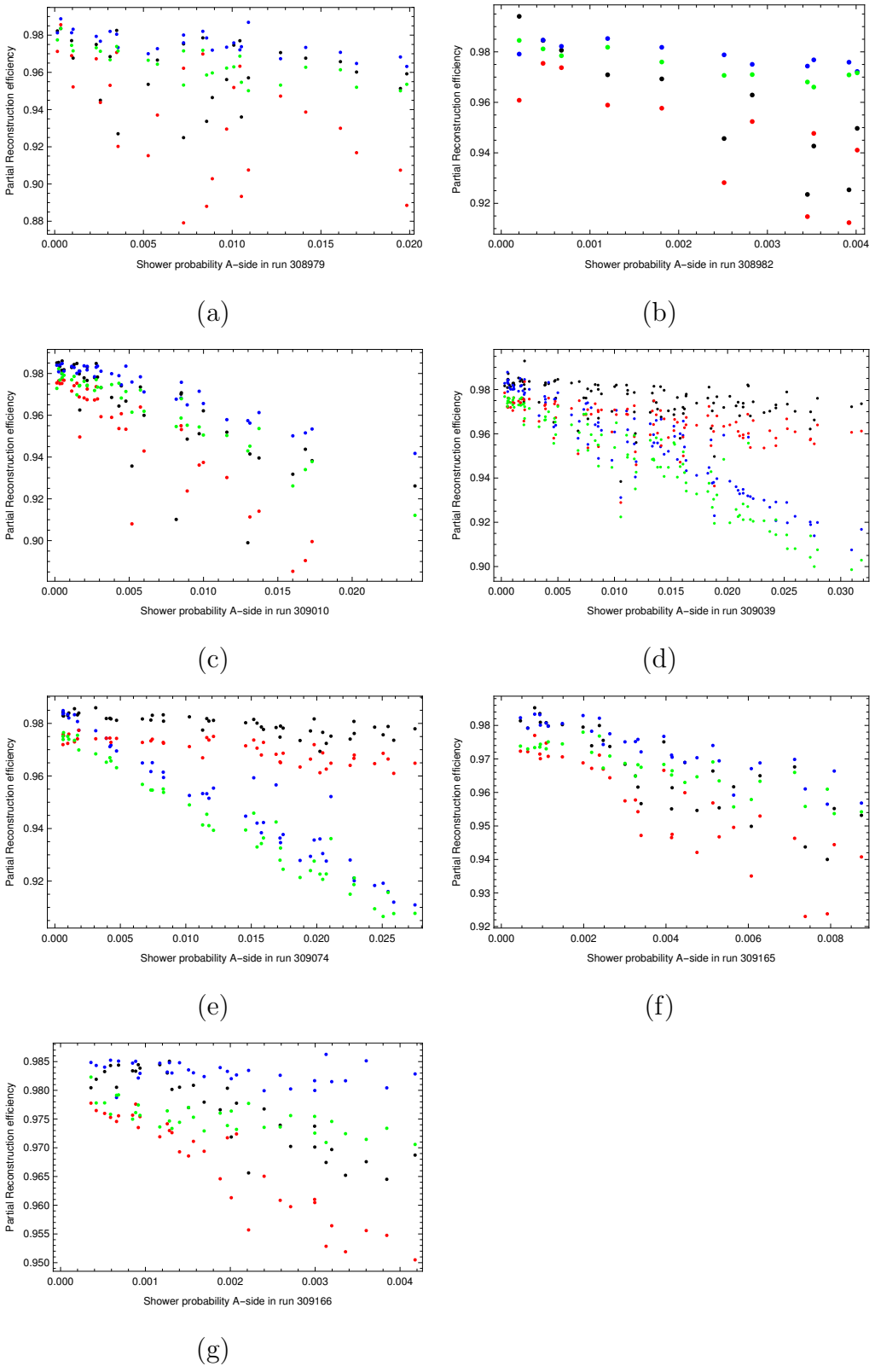

FIGURE 5.47: Correlation of the partial 2/4 reconstruction efficiencies as a function of the shower probability on A-Side. Black data points represent the correlation for topologyID 10, blue data points for topologyID 11, red data points for topologyID 12, green data points for topologyID 13.

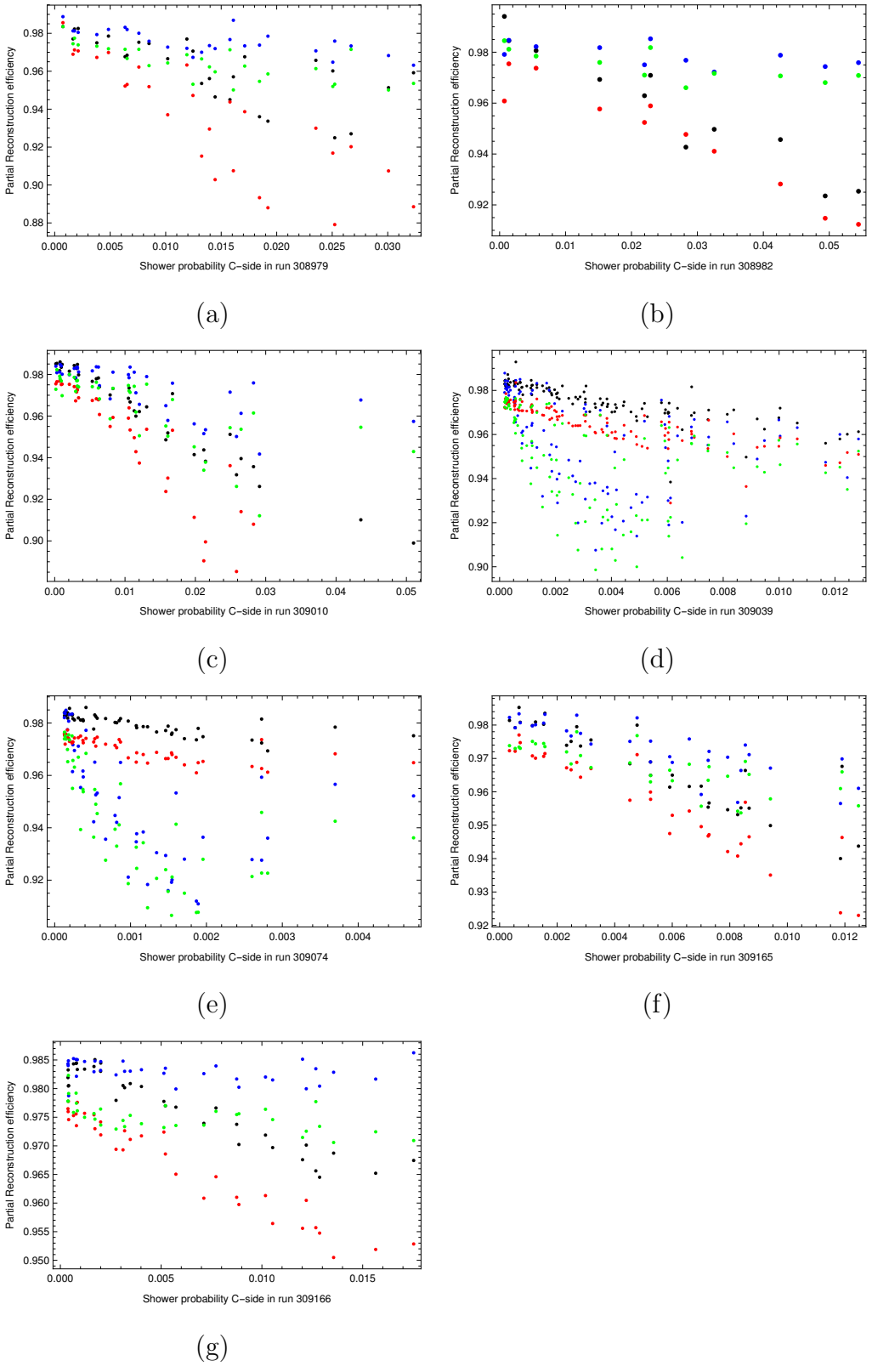

FIGURE 5.48: Correlation of the partial 2/4 reconstruction efficiencies as a function of the shower probability on C-Side. Black data points represent the correlation for topologyID 10, blue data points for topologyID 11, red data points for topologyID 12, green data points for topologyID 13.

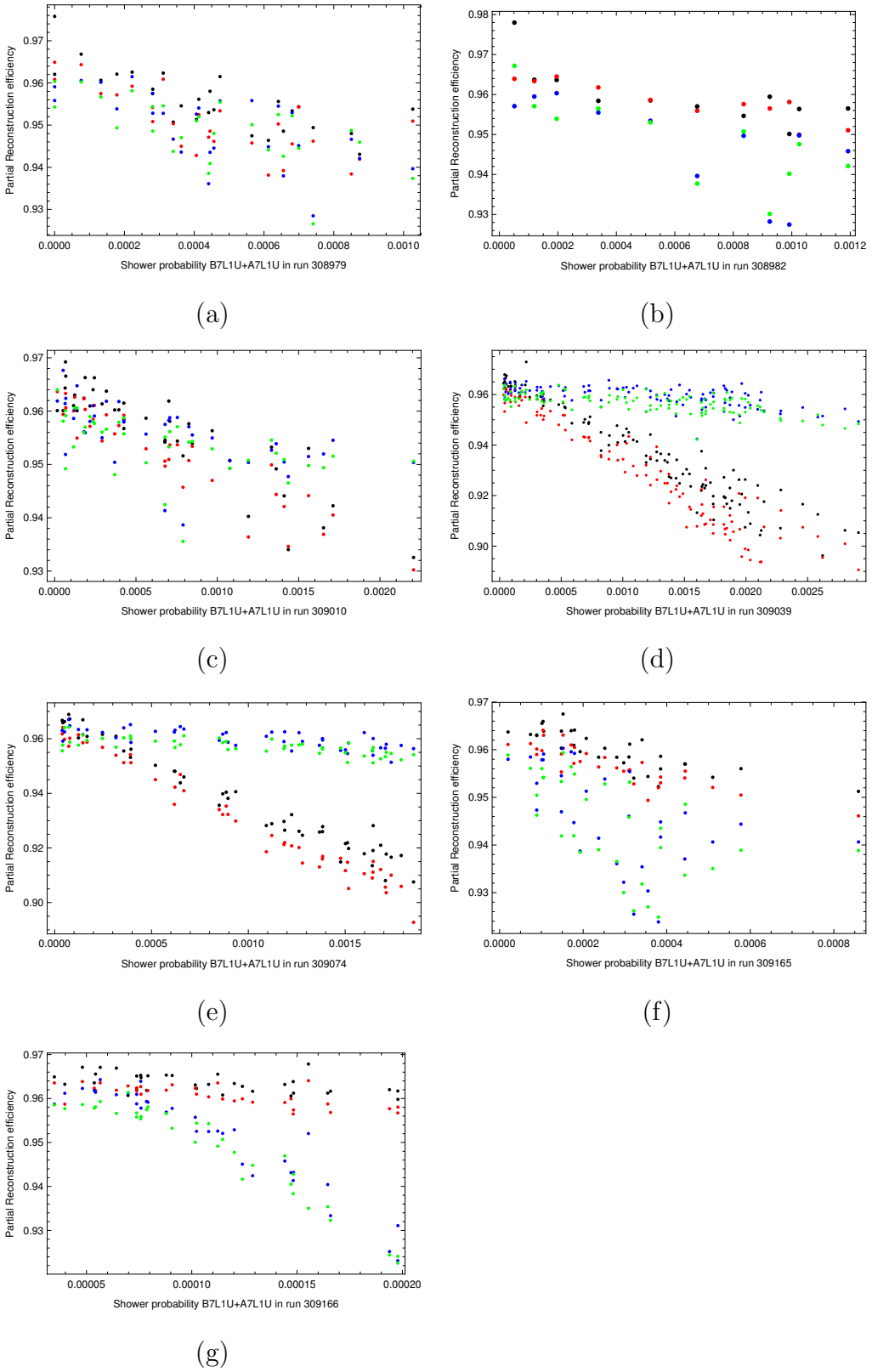

FIGURE 5.49: Correlation of the partial 3/4i reconstruction efficiencies as a function of the armlet shower probability on the upper A-Side. Black data points represent the correlation for topologyID 2, red data points for topologyID 3, blue data points for topologyID 4, green data points for topologyID 5.

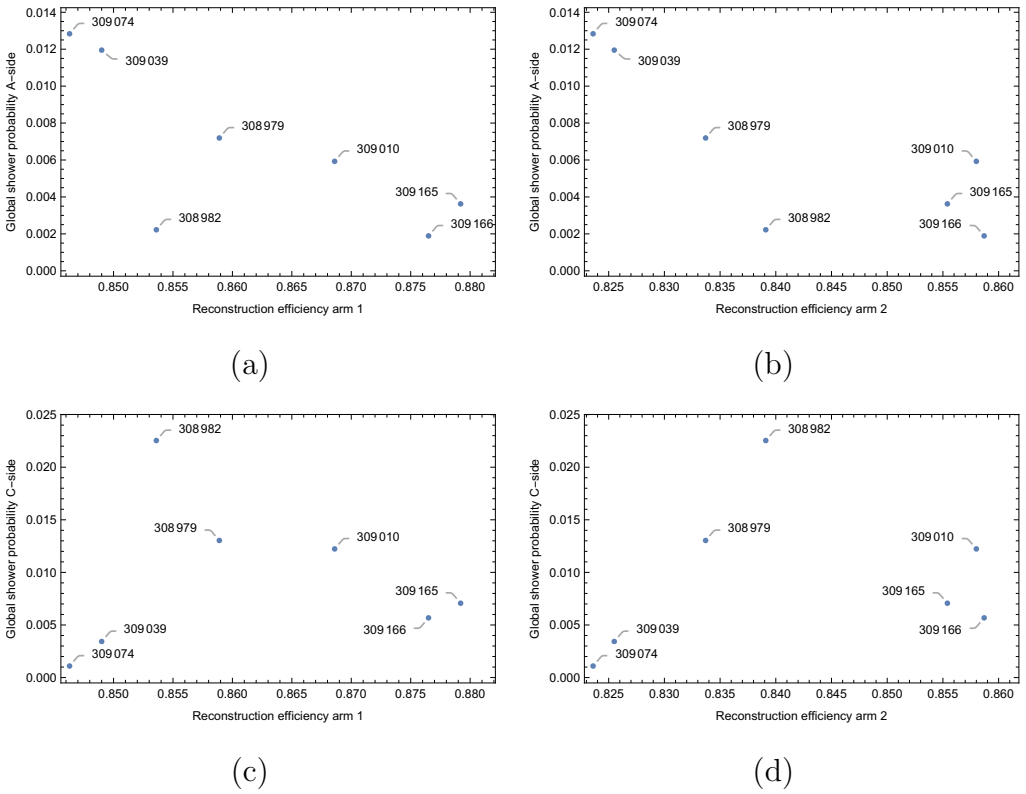

FIGURE 5.50: Time-integrated shower probability from bunch-group trigger analysis as a function of the reconstruction efficiency. Each data point represents the value pair for one run. The different plots show the efficiency values for spectrometer arm 1 and 2 and the shower probabilities at A-side and C-side respectively.

Figure 5.50 shows the correlation of the final reconstruction values per run with the observed shower probability. A clear trend is visible for the shower probabilities on A-side figures (a) and (b), where a smaller shower probability coincides with a higher final reconstruction efficiency. We see however for figures (c) and (d) that the shower probability on C-side does not show any clear correlation with the reconstruction efficiency values.

Figure 5.51 shows the correlation between the reconstruction efficiency and the armlet wise shower probabilities. We have basically the same observation here, that the shower probabilities on the A-side armlets (a), (b), (e) and (f) give a clear trend for the reconstruction efficiency, whereas the shower probabilities on the C-side armlets are uncorrelated with the reconstruction efficiency values. Here, a much higher prevalence of showers on A-side is present compared to C-side, contrary to the side-wise shower probabilities in figure 5.50 where C-side shower probability is a bit higher, however in the same order of magnitude.

Figures 5.52 show the reconstruction efficiency values as a function of the observed irreducible background fraction of the 4/4, 3/4i and 2/4 subtopologies. The according background fractions are combined from those subtopologies, which belong to the same spectrometer arm as the plotted reconstruction efficiency values. Interestingly, we see no correlations at all. It was already shown in figures 5.37 and 5.38 that there was indeed a strong correlation between the irreducible background fraction and the reconstruction efficiency within a run for different time slices. The observation however, that measured time-integrated background fractions cannot be used to make predictions on the time-integrated reconstruction efficiency (due to the missing correlation between different runs in figure 5.52) is a direct consequence of the argument, that these observed background fractions are not the cause of reduced reconstruction efficiency. The irreducible background is just a ensemble of events, that happen to have elastic signature in the back-to-back configuration (for 2/4 just the appropriate position/local angle correlation on one side from the interaction point). The fraction of these events changes when different background shapes are present.

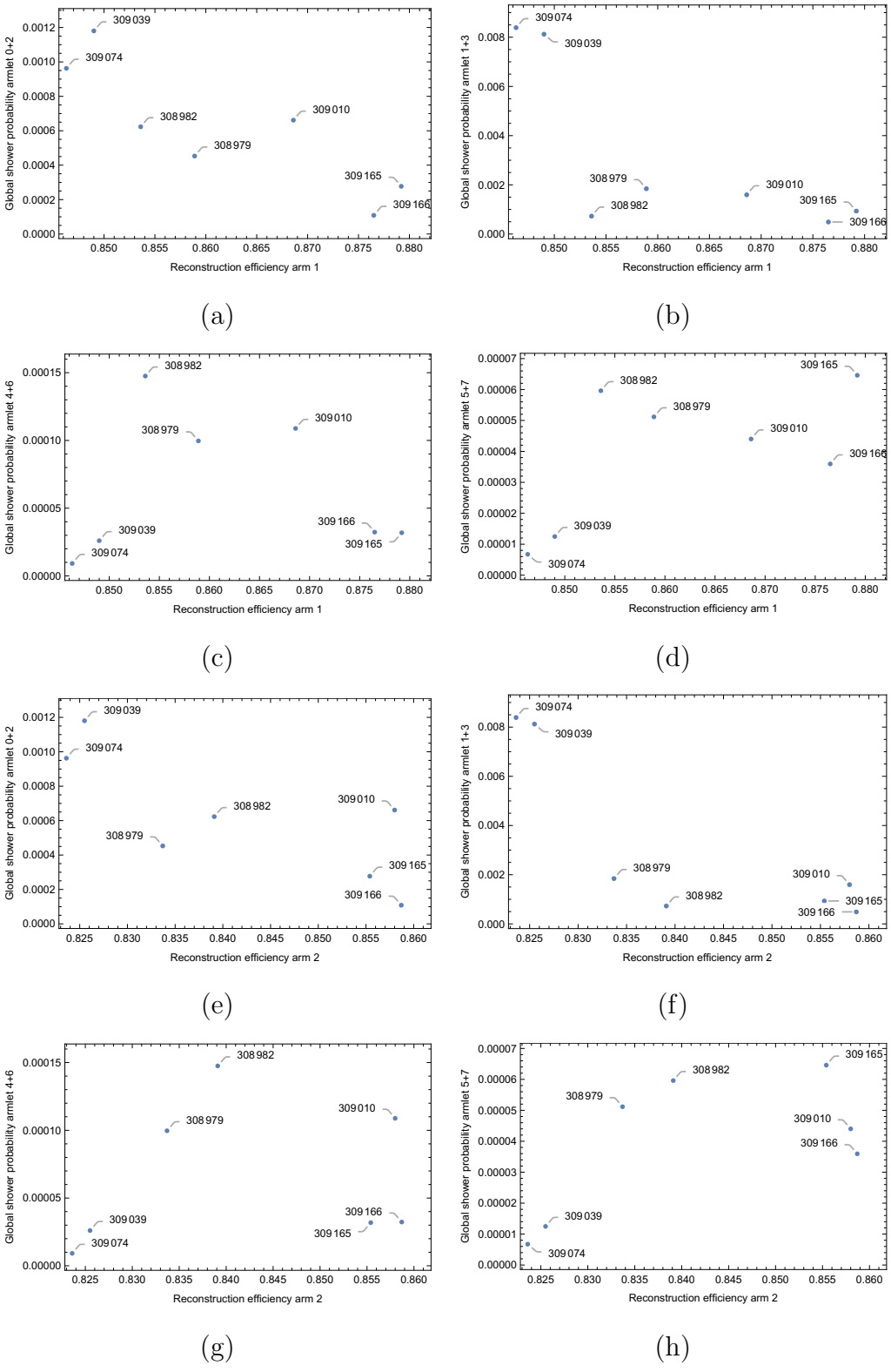

FIGURE 5.51: Time-integrated shower probability per armlet from bunch-group trigger analysis as a function of the reconstruction efficiency. Each data point represents the value pair for one run. The different plots show the efficiency values for spectrometer arm 1 and 2 and the shower probabilities respectively for the armlets "0+2" (B7L1U+A7L1U), "1+3" (B7L1L+A7L1L), "4+6" (B7R1U+A7R1U) and "5+7" (B7R1L+A7R1L).

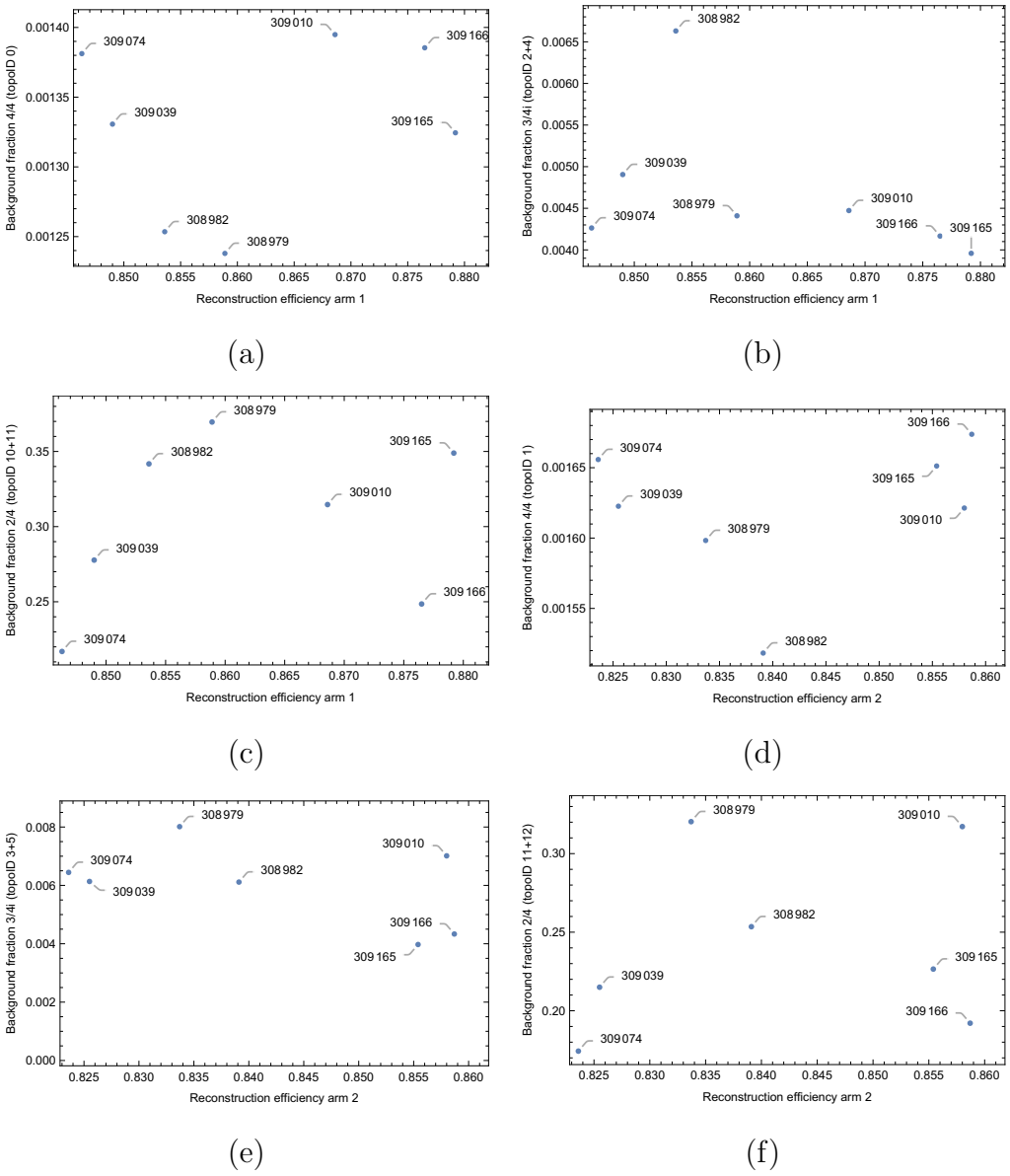

FIGURE 5.52: Time-integrated irreducible background fraction as a function of the reconstruction efficiency. Each data point represents the value pair for one run. The different plots show the efficiency values for spectrometer arm 1 and 2 and the background fraction observed in the according 4/4, 3/4i and 2/2 topologies (subtopologies combined).

5.5 Acceptance

For any given t-value, the acceptance is defined as the ratio of all events which are detectable inside the detector geometry to all number of events with that given t-value. The determination of the acceptance is Monte-Carlo based on a

PYTHIA8 simulation of an elastic sample and transport of the events from that sample to the ALFA detector stations. Knowledge of the beam optic parameters is required for the transport. The same sample is also used to calculate the acceptance corrections (EOFs) for all data driven failed topologies. For these calculations, the ratio of accepted events fulfilling the reduced set of available event selection cuts for a given topology over the accepted events using the complete golden cut set is used. The acceptance is a combination of geometrical detector acceptance and the reduction of acceptance from elastic event selection cuts, where for the latter one the EOF corrections come into play.

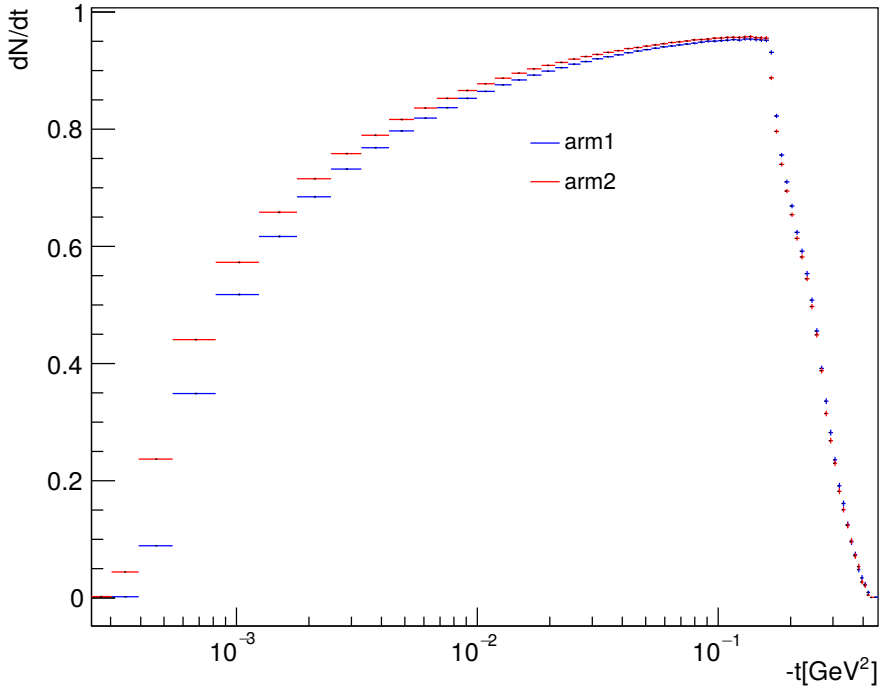

FIGURE 5.53: Acceptance curve for both spectrometer arms (arm 1 in blue, arm 2 in red), exemplary for run 309039.

Figure 5.53 shows the t-distribution of the golden acceptance.

The t-dependent phase space corrections are shown in figure 5.54. We see that all data driven failed topologies require, depending on the t-range rather sizable corrections. For the four "3/4i" event classes, those corrections are limited to the

few very first t-bins, while the remaining topologies require some corrections on the high end of the t-range. We can see, that without the EOFs, the event count in those bins would have been overestimated by about 10 percent. More critically we see that this aspect of the analysis is highly important in the 2.5km campaign to measure the reconstruction efficiency behavior near the CNI correctly.

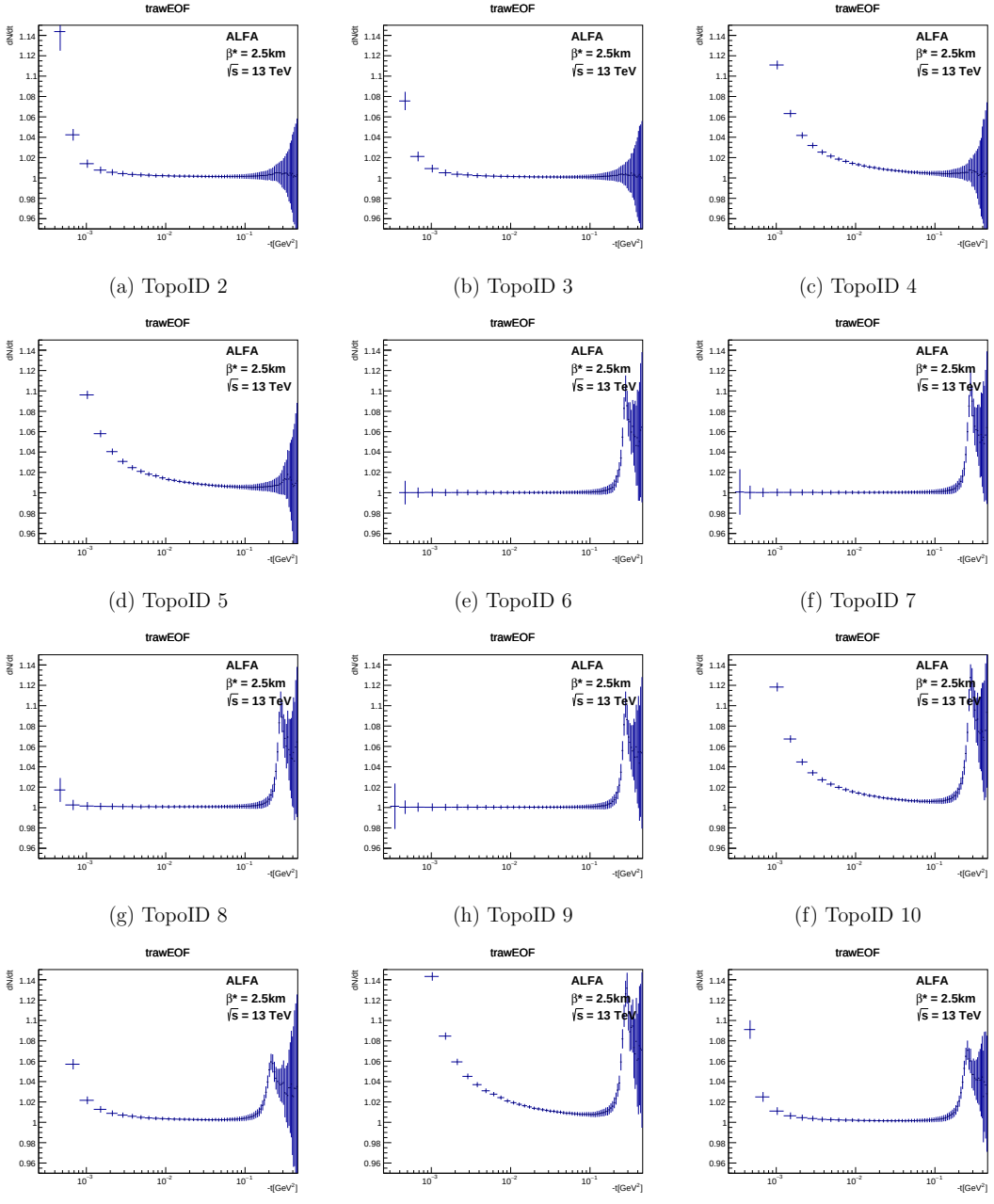

(a) TopoID 2 (b) TopoID 3 (c) TopoID 4

(d) TopoID 5 (e) TopoID 6 (f) TopoID 7

(g) TopoID 8 (h) TopoID 9 (f) TopoID 10

(g) TopoID 11 (h) TopoID 12 (f) TopoID 13

FIGURE 5.54: t-distribution of the phase space corrections (EOFs) for all data driven failed topologies.

5.6 Unfolding

Due to finite detector resolution, beam divergence and vertex spread at the interaction point, the t-value that is measured for any given elastic event is in most cases distorted compared to the true t-value. This "migration effect" needs to be taken into account in the analysis, and the measured elastic counting spectrum has to be corrected. The migration matrix for both elastic spectrometer arms is plotted in figures 5.55 and 5.56 respectively as derived from a Monte-Carlo sample. The vertical axis gives the true t-value of a generated event. The horizontal axis correlates this for the reconstructed t-value. The histogram entries show how ofter a certain transition occurs.

For the time being, a simple unfolding procedure is applied, where the bin content in the counting t-spectrum is redistributed into the same and neighboring bins with weights obtained by the according entry of the migration matrix. This procedure is done after background subtraction.

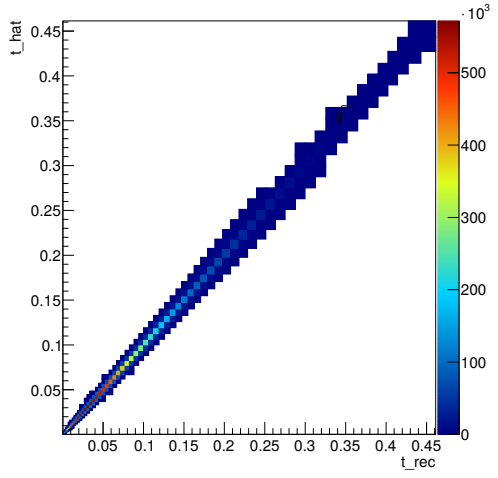

FIGURE 5.55: Migration matrix for elastic spectrometer arm 1

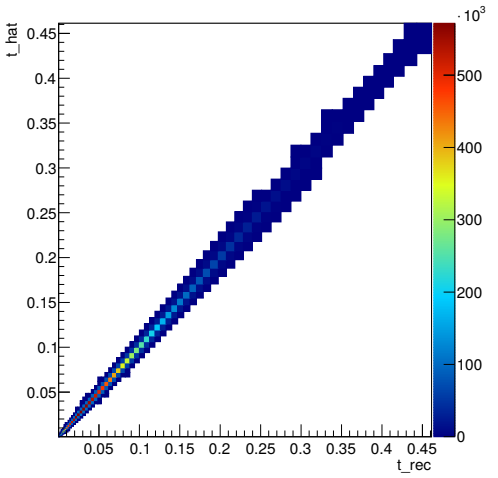

FIGURE 5.56: Migration matrix for elastic spectrometer arm 2

Chapter 6

Results

6.1 Differential elastic cross section with model fit

Figure 6.1 shows the result of the differential elastic cross section for all data sets combined as a function of t with fit values given in table 6.1. The fit was performed between $0.000543 \leq |t| \leq 0.1\text{GeV}^{-2}$. The lower end of the t-range is the lowest t-value, where an event acceptance above 10 % is archived. The high end of this range is given by an estimate, where non single-exponential contributions can be safely neglected below. The obtained ρ-values are most likely underestimated in the order of roughly 20 %, since the fit was performed without statistical correlations between the errors on the t-spectrum bins.

The first order nuclear slope model was fitted on all obtained differential elastic cross sections. Table 6.2 gives the result of those fits per run, together with

Parameter	Fit result	Fit error
σ_{tot}	104.4	0.03
B	20.7	0.01
ρ	0.0988	0.002

Table 6.1: Results from the model fit in figure 6.1

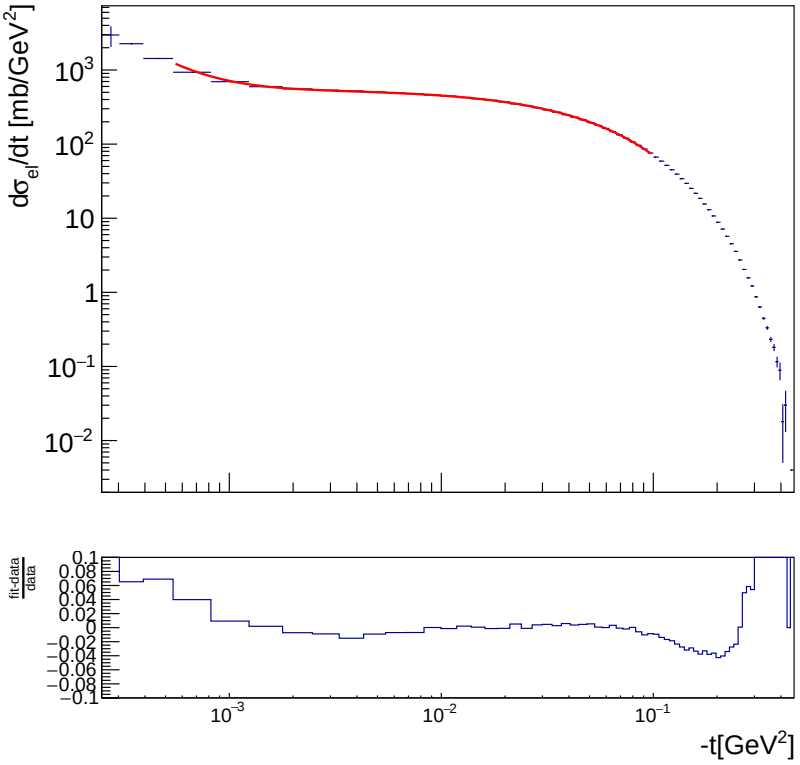

FIGURE 6.1: Combined differential elastic cross-section for all runs with model fit. The lower part shows the residual from the fit to the data. The bin-content as well as the fit of the differential elastic cross section was taken from [35], since there a more advanced unfolding procedure was used, necessary for a fit at the low t-end.

the partial systematic uncertainty due to the uncertainty in the reconstruction efficiency measurement. The results for the total cross-section are visualized in figure 6.2. For the central values, we see that there is a drift from earlier runs to later runs. Total cross section values obtained for later later runs tend to higher than for early runs. Clearly, in reality the total cross section is a physical constant at given $\sqrt{s}$ and the data points should be flat. Since the fits to the differential t-spectrum with results from 6.2 each converged nicely, the reason for the drift in total cross section measurement must stem from a drift in the t-independent normalization of the t-spectrum. The critical components in the normalization are the reconstruction efficiency and the luminosity measurement. We can see in figure 6.2 that due to the rather large systematic error contributions from the reconstruction efficiency, a constant value fit to the results is not unreasonable,

Run	$\sigma_{\text{tot}}[mb]$	syst	$B[\text{GeV}^{-2}]$	syst	ρ	syst
308979	103.47	1.4	20.78	0.01	0.1119	0.0052
308982	104.73	0.7	20.72	0.01	0.0783	0.0030
309010	103.87	0.9	20.76	0.01	0.1097	0.0037
309039	104.05	0.6	20.68	0.00	0.1014	0.0021
309074	104.55	0.8	20.77	0.01	0.0921	0.0030
309165	104.60	0.8	20.73	0.01	0.0994	0.0030
309166	105.43	0.5	20.69	0.00	0.0863	0.0019

TABLE 6.2: Run-by-run summary of the obtained total cross section values together with their partial systematic uncertainties due to the uncertainty of the reconstruction efficiency determination

resulting in a $\chi^2 = 5.00754$ per 6 degrees of freedom.

The energy evolution of all fitted parameters is given in figures 6.3,6.4 and 6.5. The inlays in each of the figures show a zoom into the LHC energy range, where TOTEM and ALFA measurements occurred. The measured total cross sections, shown in figure 6.3, from ALFA have always been slightly below those measured by the TOTEM collaboration. The reason for this is yet unknown, however it is some form of t-independent normalization discrepancy. Possible contributions are unknown systematics in the event reconstruction efficiency procedure and/or in the way of the luminosity determination (or compensation in case of TOTEMs luminosity independent measurement) in either one or both of the collaborations. The measurements of the nuclear B-slope in figure 6.4 have always been in good agreement between ALFA and TOTEM, however in [36] TOTEM found evidence of non-exponential contributions in the nuclear slope region up to $|t| < 0.2\,\text{GeV}^2$. In the according ALFA measurement, a larger value for the beam energy uncertainty was assumed, making it impossible to be sensitive to such measurement.

For the ρ-measurements in figure 6.5, ALFA continued to use the West and Yennie Coulomb phase, in tradition with previous measurement of ISR, SPS and Tevatron to make the measurements comparable, even though there is some criticism about the simplicity of this approach by [7].

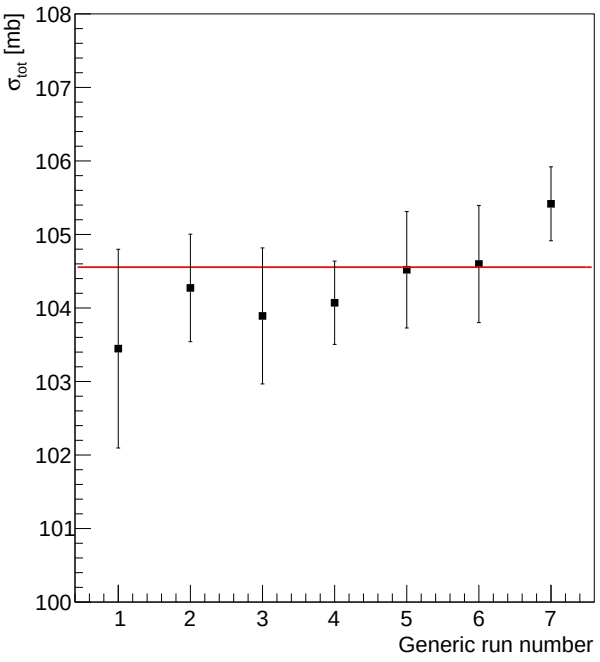

FIGURE 6.2: Fit results of the total cross-section per run with error bars from the uncertainties due to the reconstruction efficiency uncertainties. The runs were shortened as:
308979 ↦ 1 , 308982 ↦ 2 , 309010 ↦ 3 , 309039 ↦ 4 , 309074 ↦ 5 , 309165 ↦ 6 , 309166 ↦ 7

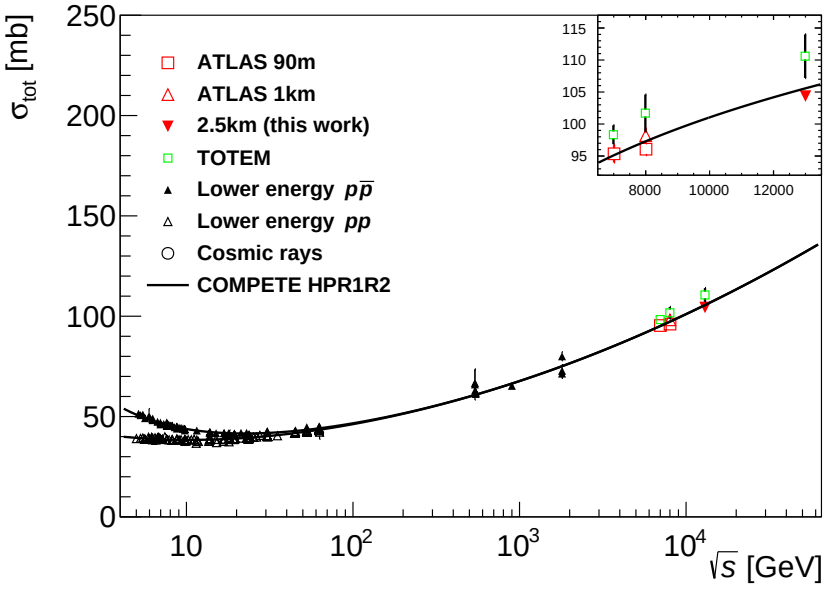

FIGURE 6.3: Comparison of the total cross section measurement from this work with other published measurements [37],[38],[39],[40],[41],[42], [43] and model predictions as a function of the center-of-mass energy [44]

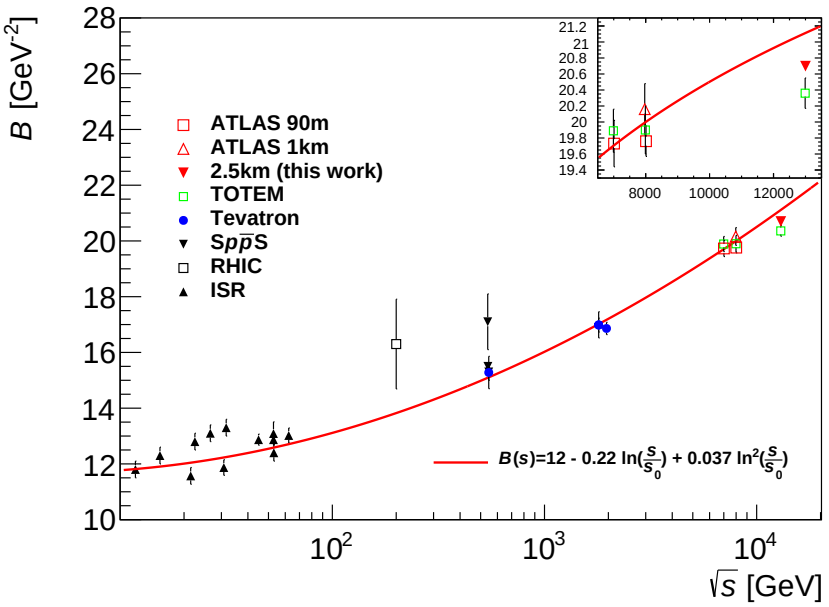

FIGURE 6.4: Comparison of the nuclear slope measurement from this work with other published results from the ISR [45][46][47] [48], at RHIC [49], at the Tevatron [50][51][52] and TOTEM [53] [54] [43]. Shown is also a calculation from [55] containing a quadratic and linear term in $log(s)$

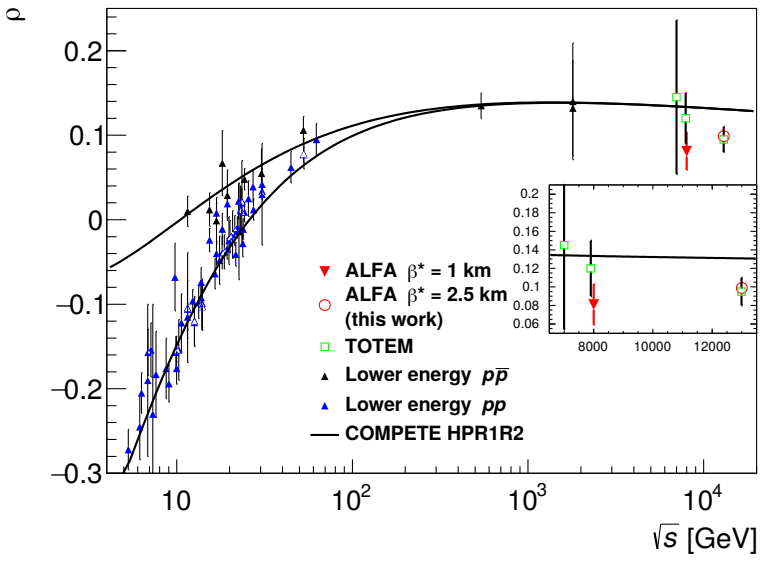

FIGURE 6.5: Comparison of the measurement of the ρ-parameter from this work with other published results [56], as well as a fit from COMPETE [44]. The two points from ALFA are not published yet, as they are work in progress. The value for the data point at $\sqrt{s} = 13\,\text{TeV}$ is from this work.

Chapter 7

Summary

In this thesis, data was analyzed that were taken at $\sqrt{s} = 13\,\text{TeV}$ in September 2016 with $\beta^* = 2.5\,\text{km}$ beam optics. The special beam optics made it possible to detect elastically scattered protons at very small momentum transfers down to $5 \cdot 10^{-4}\,\text{GeV}^2$. A measurement in the t-regime of the Coulomb-Nuclear-Interference region was thus possible and allowed for the determination of the ρ-parameter, the ratio of the real to imaginary part of the forward elastic scattering amplitude.

The central contribution of this thesis was the determination of the event reconstruction efficiency together with an estimate of the systematic and statistical error on those values for each one of the seven separate data sets. The confirmation, that the reconstruction efficiency is independent in t is also a very important result to ensure that the derived differential elastic cross-section has the correct shape near low $|t|$-values, which will be crucial for the correct determination of the ρ-parameter.

Preliminary results were present for this parameter, along with the total cross-section and the nuclear B-slope and the expected uncertainties from the reconstruction efficiency uncertainties.

The special LHC beam optic in this data taking unfortunately let to an environment with relatively large and time dependent background and upstream showers from beam halo buildup more strongly compared to earlier $\beta^* = 90\,\text{m}$ runs [28],[33]. For background estimation, a new event mixing method was

implemented, which was invented together with collaborators in light of the $\beta^* = 1\,\text{km}$, $\sqrt{s} = 8\,\text{TeV}$ analysis in order to estimate residual background fractions without the need to assume symmetric background conditions like in the previously employed "anti-golden" method. The phase space corrections (EOFs), which were invented by the author in light of earlier analysis [33] were modified and are now Monte-Carlo based, in order to be independent from uncertainties of the background pollution.

A framework for data conversion from ATLAS xAODs to ROOT NTuples, which was implemented by the author and used for all physics and commissioning data sets at $\sqrt{s} = 13\,\text{TeV}$, will continue to provide compatibility of any established analysis framework by the ALFA collaboration with future data takings by ALFA.

Appendix A

Cutflow tables for all seven runs

Topo	Triggers	After fid.	After geo	After BG sub	After EOF	EM-BG	DPE-BG	total BG	EM- BG frac	DPE- BG frac	total BG frac	EOF
0	230406	228034	217048	216779	216779	9	259	268	4.39876e-05	0.00119396	0.00123795	1
1	227552	224249	212827	212486	212486	10	329	340	4.92926e-05	0.00154898	0.00159828	1
2	12169	11860	10214	10170	10147	31	12	43	0.00304971	0.0011918	0.00424151	1.00233
3	14274	13450	11139	11071	11053	50	17	67	0.00455998	0.00154439	0.00610437	1.00161
4	29191	25547	11691	11637	11501	39	13	53	0.00336624	0.00119142	0.00455766	1.01182
5	41673	33260	11768	11652	11499	97	18	115	0.00830841	0.00153857	0.00984698	1.01326
6	5403	4558	487	470	469	16	0	16	0.0336744	0.00115519	0.0348296	1.001
7	9384	7155	938	888	886	48	1	49	0.0517594	0.00147116	0.0532306	1.00123
8	4361	3593	1209	1176	1174	31	1	32	0.0258599	0.00116453	0.0270245	1.00158
9	2929	2431	676	641	640	33	0	34	0.0493955	0.00147483	0.0508703	1.00111
10	133028	119723	14219	8800	8677	5408	10	5418	0.380366	0.000740738	0.381106	1.01418
11	29979	27128	8336	5409	5382	2919	6	2926	0.350272	0.000776714	0.351048	1.00506
12	227722	181638	22011	14556	14264	7431	22	7454	0.337628	0.00102765	0.338656	1.02047
13	30956	27148	10619	7584	7558	3022	11	3034	0.284661	0.00110982	0.285771	1.00348

TABLE A.1: Event cutflow for all data driven event topologies exemplary for run 308979. The table shows the two golden topologies with IDs 0 and 1, the 3/4i cases with IDs 2 to 5, the 3/4o cases with IDs 6 to 9 and the 2/4 cases with IDs 10 to 13. From left to right we have in the columns: The raw rate with just elastic triggers present, remaining events after fiducial cuts, remaining events after geometric correlation cuts, remaining events after background subtraction, remaining events after phase space correction (EOF), the subtracted background count determined by event mixing, the subtracted background count determined by DPE simulation, total background count, the background fraction and the phase space correction factors.

Topo	Triggers	After fid.	After geo	After BG sub	After EOF	EM-BG	DPE-BG	total BG	EM- BG frac	DPE- BG frac	total BG frac	EOF
0	75180	74410	70848	70759	70759	2	86	88	3.29793e-05	0.00122052	0.0012535	1
1	74003	73227	69934	69827	69827	1	104	106	2.49671e-05	0.0014933	0.00151827	1
2	3564	3492	3070	3050	3043	15	3	19	0.00508335	0.00121584	0.00629919	1.00233
3	3596	3475	3095	3079	3074	11	4	15	0.00357316	0.00149023	0.00506339	1.00161
4	10394	8980	3856	3829	3784	21	4	26	0.00568157	0.00121511	0.00689669	1.01182
5	6878	6201	3923	3895	3844	21	5	27	0.00546494	0.0014874	0.00695234	1.01326
6	2187	1822	164	156	156	7	0	7	0.0462917	0.00116549	0.0474572	1.001
7	918	795	257	250	250	5	0	6	0.0231573	0.00146094	0.0246182	1.00123
8	1328	1061	367	356	356	9	0	10	0.0264511	0.00118973	0.0276408	1.00158
9	569	508	187	179	179	7	0	7	0.0382284	0.0014384	0.0396668	1.00111
10	52633	47123	4813	2962	2921	1846	3	1850	0.383642	0.000753224	0.384396	1.01418
11	6935	6243	1979	1471	1463	506	1	507	0.255695	0.000909582	0.256605	1.00506
12	20073	17557	5080	3613	3540	1461	5	1466	0.287657	0.00106536	0.288722	1.02047
13	5186	4642	2350	1908	1901	438	2	441	0.186684	0.00121637	0.1879	1.00348

TABLE A.2: Event cutflow for all data driven event topologies exemplary for run 308982. The table shows the two golden topologies with IDs 0 and 1, the 3/4i cases with IDs 2 to 5, the 3/4o cases with IDs 6 to 9 and the 2/4 cases with IDs 10 to 13. From left to right we have in the columns: The raw rate with just elastic triggers present, remaining events after fiducial cuts, remaining events after geometric correlation cuts, remaining events after background subtraction, remaining events after phase space correction (EOF), the subtracted background count determined by event mixing, the subtracted background count determined by DPE simulation, total background count, the background fraction and the phase space correction factors.

Topo	Triggers	After fid.	After geo	After BG sub	After EOF	EM-BG	DPE-BG	total BG	EM- BG frac	DPE- BG frac	total BG frac	EOF
0	452157	448330	428657	428059	428059	5	592	597	1.28093e-05	0.00138206	0.00139487	1
1	451224	445961	425798	425107	425107	13	676	690	3.28073e-05	0.00158855	0.00162135	1
2	21900	21577	19501	19421	19376	52	26	79	0.00269498	0.00138026	0.00407524	1.00233
3	25921	24634	21238	21120	21086	83	33	117	0.00393266	0.00158487	0.00551753	1.00161
4	43044	38080	19884	19787	19556	69	27	96	0.00348738	0.00137916	0.00486654	1.01182
5	51691	43581	20590	20413	20146	144	32	176	0.00699708	0.00157999	0.00857707	1.01326
6	5690	4844	776	752	751	22	1	23	0.028928	0.00134395	0.0302719	1.001
7	9599	7413	1301	1232	1230	66	1	68	0.0514541	0.00150926	0.0529633	1.00123
8	4898	4336	2304	2259	2256	41	3	44	0.0178311	0.00135931	0.0191904	1.00158
9	3846	3280	1284	1240	1239	41	1	43	0.0321628	0.00153995	0.0337027	1.00111
10	130452	116953	18192	11794	11630	6380	16	6397	0.350741	0.000898568	0.35164	1.01418
11	26199	24944	12568	9203	9157	3351	12	3364	0.266677	0.00101491	0.267692	1.00506
12	213958	173000	28039	17686	17331	10324	28	10352	0.368215	0.00100525	0.369221	1.02047
13	36665	32640	16989	12800	12756	4167	20	4188	0.245335	0.00120077	0.246536	1.00348

TABLE A.3: Event cutflow for all data driven event topologies exemplary for run 309010. The table shows the two golden topologies with IDs 0 and 1, the 3/4i cases with IDs 2 to 5, the 3/4o cases with IDs 6 to 9 and the 2/4 cases with IDs 10 to 13. From left to right we have in the columns: The raw rate with just elastic triggers present, remaining events after fiducial cuts, remaining events after geometric correlation cuts, remaining events after background subtraction, remaining events after phase space correction (EOF), the subtracted background count determined by event mixing, the subtracted background count determined by DPE simulation, total background count, the background fraction and the phase space correction factors.

Topo	Triggers	After fid.	After geo	After BG sub	After EOF	EM-BG	DPE-BG	total BG	EM- BG frac	DPE- BG frac	total BG frac	EOF
0	477096	472989	451237	450613	450613	1	621	623	3.36832e-06	0.00137786	0.00138122	1
1	470027	465601	444516	443779	443779	0	736	736	0.0000	0.00165653	0.00165581	1
2	34268	33689	30086	29938	29869	105	41	147	0.0035118	0.00137492	0.00488672	1.00233
3	37625	36676	33074	32845	32792	173	54	228	0.00526093	0.00165055	0.00691148	1.00161
4	29781	26525	18721	18660	18442	35	25	60	0.00187649	0.00137717	0.00325366	1.01182
5	27846	26326	19794	19682	19424	79	32	111	0.00400452	0.00165263	0.00565715	1.01326
6	1616	1439	438	432	431	5	0	5	0.0115818	0.00136378	0.0129455	1.001
7	1975	1755	589	572	571	15	0	16	0.0262873	0.00161566	0.0279029	1.00123
8	7249	6453	2718	2654	2650	59	3	63	0.0219554	0.00134947	0.0233048	1.00158
9	4681	4230	1738	1688	1686	46	2	49	0.0267151	0.00161495	0.02833	1.00111
10	29677	26453	9406	8084	7971	1310	11	1321	0.139357	0.00118748	0.140544	1.01418
11	69455	65740	23981	17961	17871	5994	24	6019	0.249963	0.00103487	0.250998	1.00506
12	31477	28869	13744	11897	11658	1827	19	1846	0.132931	0.00143871	0.13437	1.02047
13	59600	56173	27358	22008	21932	5312	36	5349	0.194194	0.00133706	0.195531	1.00348

TABLE A.4: Event cutflow for all data driven event topologies exemplary for run 309074. The table shows the two golden topologies with IDs 0 and 1, the 3/4i cases with IDs 2 to 5, the 3/4o cases with IDs 6 to 9 and the 2/4 cases with IDs 10 to 13. From left to right we have in the columns: The raw rate with just elastic triggers present, remaining events after fiducial cuts, remaining events after geometric correlation cuts, remaining events after background subtraction, remaining events after phase space correction (EOF), the subtracted background count determined by event mixing, the subtracted background count determined by DPE simulation, total background count, the background fraction and the phase space correction factors.

Topo	Triggers	After fid.	After geo	After BG sub	After EOF	EM-BG	DPE-BG	total BG	EM- BG frac	DPE- BG frac	total BG frac	EOF
0	616524	611195	584698	583923	583923	32	742	774	5.515e-05	0.00126931	0.00132446	1
1	607263	601302	575475	574524	574524	1	949	950	2.14068e-06	0.00164908	0.00165122	1
2	27476	27054	24365	24287	24231	46	30	77	0.00189382	0.00126859	0.00316241	1.00233
3	30421	29335	25983	25891	25849	48	42	91	0.00187068	0.00164872	0.00351939	1.00161
4	53610	48341	33159	33008	32622	108	42	150	0.00328351	0.00126682	0.00455034	1.01182
5	45314	42947	34048	33900	33457	91	56	147	0.00267765	0.00164738	0.00432504	1.01326
6	3983	3415	709	682	682	25	0	26	0.0355731	0.00122578	0.0367989	1.001
7	5497	4452	923	907	906	13	1	15	0.0150606	0.00162693	0.0166875	1.00123
8	5668	5058	2886	2844	2840	37	3	41	0.013063	0.00125439	0.0143174	1.00158
9	3364	3134	1805	1778	1776	23	2	26	0.0130746	0.00163021	0.0147048	1.00111
10	92006	83769	20911	11459	11299	9437	14	9451	0.451304	0.000697391	0.452001	1.01418
11	32075	30151	16457	12283	12221	4158	15	4173	0.252677	0.000949844	0.253627	1.00506
12	104542	88535	27339	19815	19418	7490	32	7523	0.273987	0.00119923	0.275186	1.02047
13	28629	27429	20031	16635	16577	3367	27	3395	0.168135	0.00137408	0.169509	1.00348

TABLE A.5: Event cutflow for all data driven event topologies exemplary for run 309165. The table shows the two golden topologies with IDs 0 and 1, the 3/4i cases with IDs 2 to 5, the 3/4o cases with IDs 6 to 9 and the 2/4 cases with IDs 10 to 13. From left to right we have in the columns: The raw rate with just elastic triggers present, remaining events after fiducial cuts, remaining events after geometric correlation cuts, remaining events after background subtraction, remaining events after phase space correction (EOF), the subtracted background count determined by event mixing, the subtracted background count determined by DPE simulation, total background count, the background fraction and the phase space correction factors.

Topo	Triggers	After fid.	After geo	After BG sub	After EOF	EM-BG	DPE-BG	total BG	EM- BG frac	DPE- BG frac	total BG frac	EOF
0	558822	554167	529963	529228	529228	5	728	734	1.0784e-05	0.00137464	0.00138542	1
1	551456	546105	522463	521588	521588	0	873	874	1.20835e-06	0.00167256	0.00167377	1
2	22637	22294	20204	20123	20076	53	27	80	0.00263136	0.00137292	0.00400428	1.00233
3	24972	24120	21513	21423	21389	53	35	89	0.00247202	0.00167122	0.00414324	1.00161
4	42525	38483	27510	27392	27072	80	37	117	0.00291374	0.00137254	0.00428628	1.01182
5	39511	37314	28520	28392	28020	80	47	127	0.00280912	0.00167066	0.00447978	1.01326
6	2396	2148	656	636	636	18	0	19	0.0281005	0.00133787	0.0294383	1.001
7	4045	3371	948	930	929	15	1	17	0.0163537	0.00164797	0.0180017	1.00123
8	3914	3616	2320	2280	2276	36	3	39	0.0158324	0.00135475	0.0171872	1.00158
9	2544	2368	1387	1364	1362	20	2	22	0.014625	0.00165086	0.0162758	1.00111
10	46122	42600	16895	12143	11974	4734	16	4751	0.280219	0.000990812	0.28121	1.01418
11	18861	18097	11475	9118	9072	2344	12	2356	0.204279	0.00109535	0.205375	1.00506
12	74192	63839	22869	17437	17087	5402	29	5431	0.236227	0.0012796	0.237506	1.02047
13	20339	19671	15361	13309	13263	2029	22	2051	0.132096	0.00145405	0.13355	1.00348

TABLE A.6: Event cutflow for all data driven event topologies exemplary for run 309166. The table shows the two golden topologies with IDs 0 and 1, the 3/4i cases with IDs 2 to 5, the 3/4o cases with IDs 6 to 9 and the 2/4 cases with IDs 10 to 13. From left to right we have in the columns: The raw rate with just elastic triggers present, remaining events after fiducial cuts, remaining events after geometric correlation cuts, remaining events after background subtraction, remaining events after phase space correction (EOF), the subtracted background count determined by event mixing, the subtracted background count determined by DPE simulation, total background count, the background fraction and the phase space correction factors.

Bibliography

[1] Vincenzo Barone and Enrico Predazzi. *Kinematics*, pages 35–50. Springer Berlin Heidelberg, Berlin, Heidelberg, 2002. ISBN 978-3-662-04724-8. doi: 10.1007/978-3-662-04724-8_3. URL https://doi.org/10.1007/978-3-662-04724-8_3.

[2] R. Cahn. Coulombic-hadronic interference in an eikonal model. *Zeitschrift für Physik C Particles and Fields*, 15(3):253–260, 1982. ISSN 1431-5858. doi: 10.1007/BF01475009. URL http://dx.doi.org/10.1007/BF01475009.

[3] J. C. Bernauer, M. O. Distler, J. Friedrich, Th. Walcher, P. Achenbach, C. Ayerbe Gayoso, R. Böhm, D. Bosnar, L. Debenjak, L. Doria, A. Esser, H. Fonvieille, M. Gómez Rodríguez de la Paz, J. M. Friedrich, M. Makek, H. Merkel, D. G. Middleton, U. Müller, L. Nungesser, J. Pochodzalla, M. Potokar, S. Sánchez Majos, B. S. Schlimme, S. Širca, and M. Weinriefer. Electric and magnetic form factors of the proton. *Phys. Rev. C*, 90:015206, Jul 2014. doi: 10.1103/PhysRevC.90.015206. URL https://link.aps.org/doi/10.1103/PhysRevC.90.015206.

[4] Geoffrey B. West and D. R. Yennie. Coulomb interference in high-energy scattering. *Phys. Rev.*, 172:1413–1422, Aug 1968. doi: 10.1103/PhysRev.172.1413. URL https://link.aps.org/doi/10.1103/PhysRev.172.1413.

[5] Erasmo Ferreira, Takeshi Kodama, and A Kohara. Elastic amplitudes and observables in pp scattering. 1654, 11 2014.

[6] The TOTEM Collaboration. Proton-proton elastic scattering at the LHC energy of $\sqrt{s} = 7\,\text{TeV}$. *EPL (Europhysics Letters)*, 95(4):41001, 2011. URL http://stacks.iop.org/0295-5075/95/i=4/a=41001.

[7] The TOTEM Collaboration. Measurement of elastic pp scattering at $\sqrt{s} = 8\,\text{TeV}$ in the coulomb–nuclear interference region: determination of the ρ-parameter and the total cross-section. *The European Physical Journal C*, 76 (12):661, Nov 2016. ISSN 1434-6052. doi: 10.1140/epjc/s10052-016-4399-8. URL https://doi.org/10.1140/epjc/s10052-016-4399-8.

[8] O. V. Selyugin. High energy hadron spin flip amplitude. *Physics of Particles and Nuclei Letters*, 13(3):303–309, May 2016. ISSN 1531-8567. doi: 10.1134/S1547477116030195. URL https://doi.org/10.1134/S1547477116030195.

[9] Anderson Kendi, Erasmo Ferreira, and Takeshi Kodama. Amplitudes in the coulomb interference region of pp and ppbar scattering. 05 2009.

[10] R.J.N. Phillips and V. Barger. Model independent analysis of the structure in pp scattering. *Physics Letters B*, 46(3):412 – 414, 1973. ISSN 0370-2693. doi: https://doi.org/10.1016/0370-2693(73)90154-8. URL http://www.sciencedirect.com/science/article/pii/0370269373901548.

[11] Claude Bourrely, Jacques Soffer, and Tai Tsun Wu. Determination of the forward slope in pp and ppbar elastic scattering up to LHC energy. *The European Physical Journal C*, 71(3):1601, Mar 2011. ISSN 1434-6052. doi: 10.1140/epjc/s10052-011-1601-x. URL https://doi.org/10.1140/epjc/s10052-011-1601-x.

[12] The CERN accelerator complex. *CERN Document Server*. URL https://cds.cern.ch/record/1621894. Accessed on February 9th 2018.

[13] Founding member states of CERN as of 1954 (map of 1989). URL https://commons.wikimedia.org/wiki/File:BlankEurope1989.png. Accessed on February 22th 2018.

[14] TE-EPC-LPC in LHC. URL http://te-epc-lpc.web.cern.ch/te-epc-lpc/machines/lhc/pagesources/LHC-Underground-Layout.png. Accessed on February 22th 2018.

[15] The TOTEM Collaboration. Luminosity-Independent Measurement of the Proton-Proton Total Cross Section at $\sqrt{s} = 8\,\text{TeV}$. *Phys. Rev. Lett.*, 111: 012001, Jul 2013. doi: 10.1103/PhysRevLett.111.012001. URL https://link.aps.org/doi/10.1103/PhysRevLett.111.012001.

[16] ATLAS Online Luminosity. URL https://atlas.web.cern.ch/Atlas/GROUPS/DATAPREPARATION/PublicPlots/2017/DataSummary/figs/peakLumiByFill.png. Accessed on February 22th 2018.

[17] Computer generated image of the whole ATLAS detector. URL https://cds.cern.ch/record/1095924? Accessed on February 22th 2018.

[18] ATLAS Detector and Technology. URL http://atlas.cern/discover/detector. Accessed on February 22th 2018.

[19] An computer generated image representing how ATLAS detects particles. URL https://cds.cern.ch/record/1505342. Accessed on February 22th 2018.

[20] ATLAS pixel detector electronics and sensors. *Journal of Instrumentation*, 3(07):P07007, 2008. URL http://stacks.iop.org/1748-0221/3/i=07/a=P07007.

[21] Computer generated image of the ATLAS inner detector. URL https://cds.cern.ch/images/CERN-GE-0803014-01. Accessed on February 22th 2018.

[22] Vasiliki A. Mitsou. The ATLAS transition radiation tracker. pages 497–501, 2003. doi: 10.1142/9789812702708_0073. URL http://weblib.cern.ch/abstract?ATL-CONF-2003-012.

[23] P Puzo. ATLAS calorimetry. 494:340–345, 11 2002.

[24] E. Diehl. ATLAS Muon Detector Commissioning. In *Particles and fields. Proceedings, Meeting of the Division of the American Physical Society, DPF 2009, Detroit, USA, July 26-31, 2009*, 2009. URL http://inspirehep.net/record/834063/files/arXiv:0910.2767.pdf.

[25] *ATLAS muon spectrometer: Technical Design Report.* Technical Design Report ATLAS. CERN, Geneva, 1997. URL https://cds.cern.ch/record/331068.

[26] A. Sidoti. Minimum Bias Trigger Scintillators in ATLAS Run II. *Journal of Instrumentation*, 9(10):C10020, 2014. URL http://stacks.iop.org/1748-0221/9/i=10/a=C10020.

[27] Sketch of ATLAS-ALFA Detector Positions. URL https://twiki.cern.ch/twiki/pub/Atlas/AlfaMechanics/Roman_Pot_and_detector_positions_31-03-2016.pdf. Accessed on March 2nd 2018.

[28] Measurement of the total cross section from elastic scattering in pp collisions at $\sqrt{s} = 7\,\text{TeV}$ with the ATLAS detector. *Nuclear Physics B*, 889:486 – 548, 2014. ISSN 0550-3213. doi: https://doi.org/10.1016/j.nuclphysb.2014.10.019. URL http://www.sciencedirect.com/science/article/pii/S0550321314003253.

[29] P. Hansen J.B. Hansen S. Jakobsen, P. Fassnacht. Commissioning of the Absolute Luminosity For ATLAS detector at the LHC. PHD Thesis.

[30] K. Janas. Analysis of the Track Reconstruction Algorithm in the ALFA detector of the ATLAS experiment, 2014. Technical report.

[31] *Transversale Bahndynamik in Kreisbeschleunigern*, pages 239–288. Springer Berlin Heidelberg, Berlin, Heidelberg, 2008. ISBN 978-3-540-75282-0. doi: 10.1007/978-3-540-75282-0_6. URL https://doi.org/10.1007/978-3-540-75282-0_6.

[32] B. Allongue et al. Test Beam: First measurements with an ALFA Roman Pot Prototype, 2008. Internal ATLAS note:. ATL-LUM-INT-2010-001.

[33] The ATLAS Collaboration. Measurement of the total cross section from elastic scattering in pp collisions at $\sqrt{s} = 8$ TeV with the ATLAS detector. *Phys. Lett.*, B761:158–178, 2016. doi: 10.1016/j.physletb.2016.08.020.

[34] Simon Holm Stark. *Study of forward elastic pp scattering at = 8 TeV with the ALFA detector*. PhD thesis, 2017.

[35] Hasko Stenzel. Private Communication, 2018.

[36] The TOTEM Collaboration. Evidence for non-exponential elastic proton-proton differential cross-section at low $|t|$ and $\sqrt{s}$=8 TeV by TOTEM. *Nucl. Phys.*, B899:527–546, 2015. doi: 10.1016/j.nuclphysb.2015.08.010.

[37] J. Beringer et al. Review of Particle Physics (RPP). *Phys. Rev.*, D86:010001, 2012. doi: 10.1103/PhysRevD.86.010001.

[38] The TOTEM Collaboration. Measurement of proton-proton elastic scattering and total cross-section at $\sqrt{s} = 7\,\text{TeV}$. 101:21002, 01 2013.

[39] Pedro Abreu et al. Measurement of the proton-air cross-section at $\sqrt{s} = 57$ TeV with the Pierre Auger Observatory. *Phys. Rev. Lett.*, 109:062002, 2012. doi: 10.1103/PhysRevLett.109.062002.

[40] G. Aielli et al. Proton-air cross section measurement with the ARGO-YBJ cosmic ray experiment. *Phys. Rev.*, D80:092004, 2009. doi: 10.1103/PhysRevD.80.092004.

[41] M. Honda, M. Nagano, S. Tonwar, K. Kasahara, T. Hara, N. Hayashida, Y. Matsubara, M. Teshima, and S. Yoshida. Inelastic cross section for p-air collisions from air shower experiments and total cross section for p-p collisions up to $\sqrt{s} = 24\,\text{TeV}$. *Phys. Rev. Lett.*, 70:525–528, Feb 1993. doi: 10.1103/PhysRevLett.70.525. URL `https://link.aps.org/doi/10.1103/PhysRevLett.70.525`.

[42] R. M. Baltrusaitis, G. L. Cassiday, J. W. Elbert, P. R. Gerhardy, S. Ko, E. C. Loh, Y. Mizumoto, P. Sokolsky, and D. Steck. Total Proton Proton

Cross-Section at s**(1/2) = 30-TeV. *Phys. Rev. Lett.*, 52:1380–1383, 1984. doi: 10.1103/PhysRevLett.52.1380.

[43] The TOTEM Collaboration. First measurement of elastic, inelastic and total cross-section at $\sqrt{s} = 13$ TeV by TOTEM and overview of cross-section data at LHC energies. 2017.

[44] K.A. Olive and Particle Data Group. Review of Particle Physics. *Chinese Physics C*, 38(9):090001, 2014. URL `http://stacks.iop.org/1674-1137/38/i=9/a=090001`.

[45] U. Amaldi et al. New Measurements of Proton Proton Total Cross-Section at the CERN Intersecting Storage Rings. *Phys. Lett.*, B 62:460, 1976.

[46] G. Barbiellini et al. Small angle proton proton elastic scattering at very high-energies (460 GeV$^2 \leq s \leq$ 2900 GeV^2). *Phys. Lett.*, B 39:663, 1972.

[47] N. Amos et al. Measurement of Small Angle $\bar{p}p$ and Proton Proton Elastic Scattering at the CERN Intersecting Storage Rings. *Nucl. Phys.*, B 262:689, 1985.

[48] M. Ambrosio et al. Measurement of Elastic Scattering in Anti-proton - Proton Collisions at 52.8 GeV Center-of-mass Energy. *Phys. Lett.*, B 115:495, 1982.

[49] Stephen L. Bueltmann et al. First measurement of proton proton elastic scattering at RHIC. *Phys. Lett.*, B 579:245, 2004.

[50] F. Abe et al. Measurement of small angle proton-antiproton elastic scattering at $\sqrt{s} = 546$ and 1800 GeV. *Phys. Rev.*, D 50:5518, 1994.

[51] N. Amos et al. Measurement of ρ, the ratio of the real to imaginary part of the $\bar{p}p$ forward elastic scattering amplitude, at $\sqrt{s} = 1.8$-TeV. *Phys. Rev. Lett.*, 68:2433, 1992.

[52] V. M. Abazov et al. Measurement of the differential cross section $d\sigma/dt$ in elastic $p\bar{p}$ scattering at $\sqrt{s}$=1.96 TeV. *Phys. Rev.*, D 86:012009, 2012.

[53] G. Antchev et al. Luminosity-independent measurement of the proton-proton total cross section at $\sqrt{s} = 8$ TeV. *Phys. Rev. Lett.*, 111:012001, 2013.

[54] G. Antchev et al. Measurement of proton-proton elastic scattering and total cross-section at $\sqrt{s} = 7$ TeV. *Europhys. Lett.*, 101:21002, 2013.

[55] V. A. Schegelsky and M. G. Ryskin. Diffraction cone shrinkage speed up with the collision energy. *Phys. Rev.*, D 85:094024, 2012.

[56] The TOTEM Collaboration. First determination of the ρ-parameter at $\sqrt{s} = 13\,\text{TeV}$, probing the existence of a colourless three-gluon bound state. *Submitted to: Phys. Rev.*, 2017.

List of Figures

List of Tables

Selbstständigkeitserklärung

Ich erkläre: Ich habe die vorgelegte Dissertation selbstständig und ohne unerlaubte fremde Hilfe und nur mit den Hilfen angefertigt, die ich in der Dissertation angegeben habe. Alle Textstellen, die wörtlich oder sinngemäß aus veröffentlichten Schriften entnommen sind, und alle Angaben, die auf mündlichen Auskünften beruhen, sind als solche kenntlich gemacht. Ich stimme einer evtl. Überprüfung meiner Dissertation durch eine Antiplagiat-Software zu. Bei den von mir durchgeführten und in der Dissertation erwähnten Untersuchungen habe ich die Grundsätze guter wissenschaftlicher Praxis, wie sie in der "Satzung der Justus-Liebig-Universität Gießen zur Sicherung guter wissenschaftlicher Praxis" niedergelegt sind, eingehalten.

Ort, Datum	Unterschrift